Molecular simulation of crystal growth in alkane and polyethylene melts

by

Numan Waheed

B.S. Chemical Engineering, Cornell University (1997)

Submitted to the Department of Chemical Engineering in partial fulfillment of the requirements for the degree of

DOCTOR OF PHILOSOPHY
at the
MASSACHUSETTS INSTITUTE OF TECHNOLOGY

April 2005
[June 2005]

Author.....
Department of Chemical Engineering
April 27, 2005

Certified by.....
Gregory C. Rutledge
Professor of Chemical Engineering
Thesis Supervisor

Accepted by.....
Daniel Blankschtein
Professor of Chemical Engineering
Chairman, Committee for Graduate Students

Molecular simulation of crystal growth in alkane and polyethylene melts

by

Numan Waheed

Submitted to the Department of Chemical Engineering on April 27, 2005
in partial fulfillment of the requirements for the degree of
Doctor of Philosophy in Chemical Engineering

Abstract

Molecular simulation has become a very powerful tool for understanding the process of polymer crystallization. By using carefully constructed simulations, one can independently observe the two phenomena responsible for melt crystallization: nucleation and growth. This research focuses on modeling the growth process using potentials that are well-parameterized for alkanes and polyethylene.

In experiment and modeling of the kinetics of alkane crystallization, focus has been concentrated on growth rates very near the melting temperature, where the growth of these systems is optically observable. In this temperature range near T_m, diffusion is not a limiting factor, which has led to theory that models the thermodynamic driving force and its effect on kinetics. Phenomenologically, one observes a maximum growth rate at a temperature intermediate between the glass transition temperature T_g and the melt temperature T_m. This arises as a competition between a thermodynamic driving force towards crystal growth, associated with locking chains into crystallographic registry and the ability of chains to diffuse to the new layer and rearrange themselves conformationally to satisfy the restrictions of crystal symmetry. The thermodynamic driving force is rate limiting at high temperatures, while melt mobility is rate limiting at low temperatures.

Growth rates are of interest to the polymer processing community, who require accurate crystallization kinetic data over the entire temperature range, in order to predict solidification under process conditions and thus final fiber properties. A model which retains its connection to molecular structure would certainly be of benefit for purposes of product design; such connection is possible using molecular simulations. Non-equilibrium molecular dynamics enables us to observe growth for a range of temperatures around the temperature at which the maximum growth rate occurs.

We present a molecular dynamics (MD) framework for measuring crystal growth rates for n-eicosane ($C_{20}H_{42}$, denoted C20), by simulating growth on a pre-existing crystal surface. We show that growth rates for short alkanes such as C20 are directly observable over a range of quench temperatures, for the case where the crystallization front is preceded by a supercooled amorphous region, and heat transfer occurs faster than the characteristic time for crystallization. We present data that we have acquired from these simulations through analysis of the propagation of orientational order, using the bond order parameter, and density changes, using Voronoi volumes.

To determine molecular weight effects, we use the same technique to look at systems of $C_{50}H_{102}$ and $C_{100}H_{202}$ (denoted C50 and C100). With these higher molecular

weight n-alkanes, we can also measure the occurrence of folds during crystal growth. From these MD simulations, we obtain data for the growth rate of n-alkane crystals over a range of temperatures and molecular weights. Qualitatively, we see frequent adsorption and desorption of chain segments on the surface in both C50 and C100 systems. We find evidence for a surface nucleus involving 4-5 chain segments, from multiple chains, that are approximately 20 beads long, shorter than the ultimate thickness of the chain stem in the crystal.

We construct a general crystal growth model that can be parameterized entirely in terms of universal properties of polymer chains, described by polymer physics and chemically specific quantities that can be estimated polymer by polymer using molecular dynamics simulations. The model is an extension to polymer crystallization models to incorporate molecular weight effects, using a small number of chemically specific quantities that can be estimated from molecular dynamics simulations. It accounts for the thermodynamic driving force, using classical nucleation theory, and melt relaxation time, using WLF theory. Our model can predict rates as a function of temperature and molecular weight, up to the entanglement molecular weight.

Past the entanglement molecular weight, the analysis reveals that the growth rate of alkanes and polyethylene can both be described by the same relationship. The appropriate relaxation time is used to describe the kinetic barrier to crystallization. For chains shorter than the entanglement length, this is the Rouse time. For chains longer than the entanglement molecular weight, kinetic limitations are modeled by the local relaxation of an entangled segment at the interface. Use of the model is illustrated for polyethylene crystallizing in a fiber spin line under conditions of slow cooling and fast cooling.

Finally, we present a simplified framework for the study of polymer crystallization using Kinetic Monte Carlo (KMC). We have developed a general KMC algorithm for measuring growth of a polymer crystal phase during melt crystallization, based on the algorithm of Bortz *et al.* We have incorporated new moves into a general framework to allow multi-chain, three-dimensional growth and the escape of chains from the crystal to the melt, through the fold surface. We performed parametric studies on the melt-crystallization of C20 to study the effects of each energy barrier. In addition, the KMC algorithm allows us to consider the importance of individual moves in contributing to growth. We have shown, as a proof-of-concept, that this algorithm is capable of generating morphologies characteristic of several theories of secondary nucleation in polymer melts.

Thesis Supervisor: Gregory C. Rutledge
Title: Professor of Chemical Engineering

Acknowledgements

I would like to thank Professor Greg Rutledge, who has been an extraordinary advisor and mentor. His determination to understand the details of my work stimulated my own deeper understanding. His patience allowed me to explore avenues that didn't always benefit, but helped me to make a map that I will use for years. And Greg knows the importance of a good map.

I would like to thank the wonderful researchers that provided great advice and support, especially my thesis committee. And my coworkers, Dr. Marc S. Lavine and Dr. Min Jae Ko, who have been my deskmates, teachers, and friends. My thanks and respect to the Rutledge research group. They have been great company, magnetic personalities, and probing researchers. I must also thank the members of the MIT CAEFF team, who have been wonderful collaborators and travel companions. My thanks to the support staff at MIT, in all capacities, who keep this place running. I also thank the professors and friends from the University of Leeds who welcomed me during my time there.

I must thank CAEFF, the Center for Advanced Engineering Fibers and Films, for financial support. I thank Dr. Jonathan Harris and Dr. Sandeep Patel, for making their source code available in the initial stages. Also, thanks to Professor Mark Gerstein for making his Voronoi tessellation algorithm available.

I would like to thank my family. My parents have been both supportive and encouraging, during these years, and offered invaluable advice. My sister is the best sister ever, and has always encouraged me to think outside the box. I love them dearly. Thanks to my friends I met through the MSAs of Boston, who are some of the best people I know. They make the best friends, roommates, and company. Also, my friends at the Interfaith Abrahamic Discussion, who have opened my horizons. And there are several other uncategorizable friends to whom I owe a great deal, including Suleman, Sid, Jontie, Caline, Ahsun, and Waqas, among others.

I thank God for the opportunity to learn and for making it a priority for me. I now know that any topic of study requires a spiritual journey, as well as a scientific one. For even in polymer physics, I have seen signs.

> "O Assemblies of Mankind and Jinn! If you can penetrate the realms of the Heavens and the Earth, then penetrate them. You will not be able to penetrate them except by My authority. Then which of the favors of your Lord, will you both deny?"
>
> The Qur'an 55:33-34

This work was supported by the Center for Advanced Engineering Fibers and Films (CAEFF) of the Engineering Research Centers Program of the National Science Foundation, under NSF Award Number EEC-9731680.

TABLE OF CONTENTS

LIST OF FIGURES

LIST OF TABLES

Chapter 1

Introduction

1.1 Motivation

Polymer melt crystallization during processing has been a phenomenon of long-standing interest, from the melt-spinning work of Ziabicki to the injection-molding studies of van Krevelen [Ziabicki 1976; van Krevelen 1978], and is of considerable engineering importance. However, even for the relatively simple case of quiescent crystallization of polyethylene (PE), the physical steps involved during melt crystallization are still unclear. Experiments on polyethylene reveal a complex morphology. Pioneering work by Keith and by Keller revealed that within the spherulitic structure that develops lie layers of twisting stacked lamellae, separated by layers of amorphous polymer [Keller 1955; Keith 1964]. Since polymer crystallization, unlike atomic crystallization, is a kinetically-limited process, growth rate studies have been of primary relevance. As early as the 1950's, Mandelkern showed that the temperature dependence of the spherulitic growth rate is consistent with crystal growth controlled by secondary nucleation [Mandelkern 1958].

Prevailing theories of polymer crystallization are based on classical nucleation theory, from the early work by Turnbull and Fisher [Turnbull and Fisher 1949]. Since growth is controlled by secondary nucleation, a number of theories have emerged specifically for polymer melts, although most invoke other assumptions that are obtained by analogy to single crystal formation in dilute solution. Hoffman-Lauritzen theory uses a surface energy argument to justify the assumption that chain stems deposit on the surface fast enough to be considered a single process [Hoffman and Miller 1997]. Sadler's entropic barrier model incorporates the idea of molecular pinning and accounts for surface roughening [Sadler and Gilmer 1986]. Point's model allows for each unit to attach or detach, creating the possibility of having folds anywhere [Point 1979]. All three theories exhibit elements of agreement with the existing experimental evidence, and remained in contention largely due to the lack of detailed, mechanistic data that might distinguish one over the others. More recently, Strobl has conjectured a multi-step model with intermediate "granular crystal layers" that merge to form the lamellar crystal [Strobl 2000]. This model agrees with more recent experimental results for PE, including the TEM studies of Kanig, and the FTIR work of Tashiro *et al.*, which reveal a hexagonal phase precursor to the orthorhombic form of PE [Kanig 1991; Tashiro et al. 1998].

Empirically-based process models for crystallization kinetics have also been developed. These tend to derive from the general statistical arguments of Avrami, regarding the time dependence of the degree of crystallinity [Avrami 1940]. Nakamura *et al.* extended Avrami's original analysis by proposing the "isokinetic assumption," whereby the time dependence of the linear growth rates is equal to the time dependence of nucleation rates [Nakamura et al. 1973]. Subsequently, Ziabicki's extension to this

equation, modified to account for orientation, has proved to be the most common form employed in processing and in constitutive models. It links crystallization rates to empirical parameters that are material dependent. Ziabicki's empirical model for crystallization is

$$G(T) = G_{\max} \exp\left[-4 \log 2 \frac{(T - T_{\max})^2}{D^2} + C_a f_a^2 \right] \tag{1.1}$$

where $G(T)$ is the growth rate, G_{max} is the maximum growth rate, T_{max} is the temperature at which G_{max} occurs, and the parameter D is the half-width of the empirically-observed curve for the temperature dependence of the rate. This dependence of rates on temperature implies that there is a maximum rate for polymer crystallization, at a temperature intermediate between T_g and T_m. As one approaches T_g, the mobility of the system becomes restrictive and slows diffusive transport to the growing crystal surface; conversely, as one approaches T_m, crystallization is hindered by the low thermodynamic driving force. For flow conditions, f_a is the measure of "amorphous orientation" prior to crystallization, and C_a is an empirical parameter for the enhancement of crystallization due to the amorphous orientation. The recent work of Eder *et al.* provides a more general representation, where primary nucleation is described in terms of an activation time spectrum [Eder et al. 1990]. This formulation still requires an empirical model to characterize growth rates, but obtaining these parameters from experiments is difficult, since crystallization rates often depend of the experimental setup and the processing history of the sample.

Molecular simulation has become an important tool for understanding the process of alkane crystallization. Simulation techniques such as lattice dynamics, Monte Carlo, and molecular dynamics provide detailed information that experiments have not yet been able to capture, due to the complex morphologies of crystallizing polymer systems. Through carefully constructed simulations, one can independently observe nucleation and growth during melt crystallization, the latter often described as either layer or normal growth.

Simulation-based modeling has become a fundamental technique in understanding the behavior of polymers in situations where the equilibrium assumption holds valid. However, progress has been slower in the modeling of dynamic processes, because of the long time and length scales involved. Our interest is in polymer crystallization, which is a dynamic phase change process from an amorphous initial state to a metastable semi-crystalline final state. This phenomenon has proven to be difficult to model realistically, although a great deal has been learned from simplified modeling. It would be more beneficial if simulations could be used to generate the kinetic rate data that can be used in processing models or a finite element processing simulation, as shown in Fig. 1.1. Molecular and Langevin dynamics in particular are techniques that are capable of generating dynamic data for molecular-level systems.

None of the crystallization models currently available in the literature are fully applicable for describing alkane crystallization rates over a wide range of temperatures and molecular weights solely using parameters that depend only on chemical architecture. Nevertheless, a model which retains its connection to molecular structure would certainly

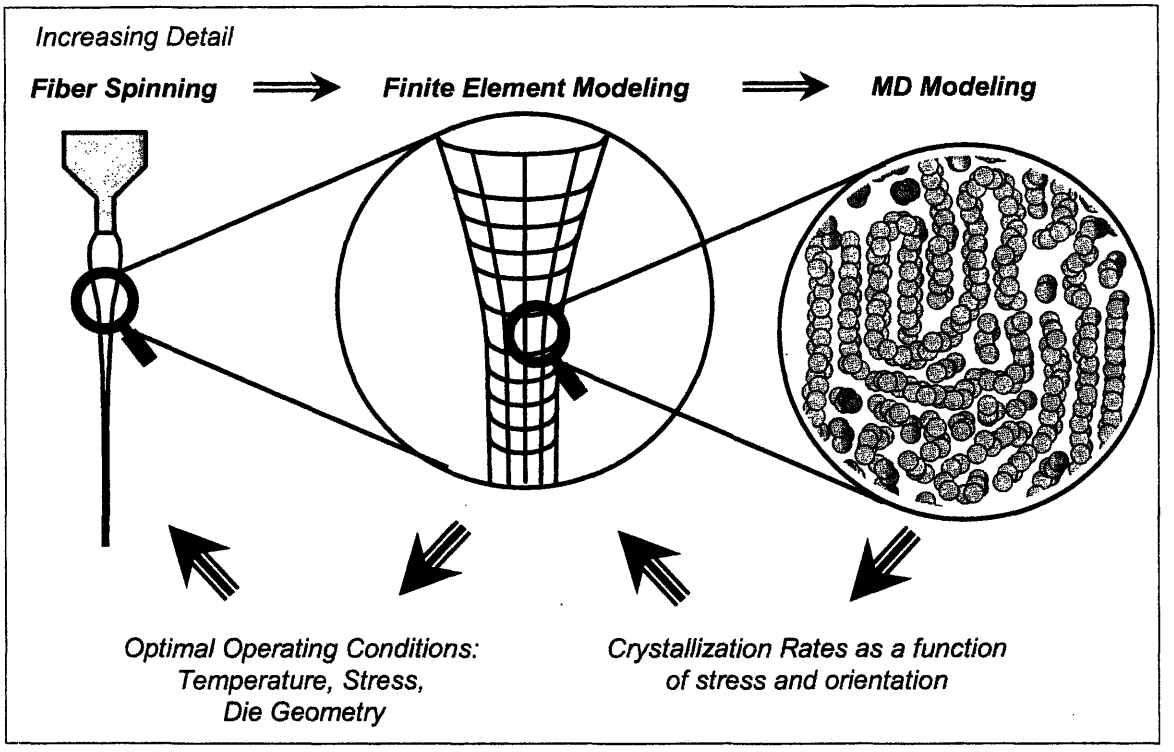

Figure 1.1 Hierarchy of molecular modeling motivation.

be of benefit for purposes of product design; such connection is possible using molecular modeling. Atomistic simulation, through its resolution on the atomic length scale, provides information that cannot be obtained through any other source.

1.2 Objectives

The objectives of this work have been to improve the understanding of the kinetics of crystallization of polyethylene, in order to parameterize process models and constitutive equations used in accounting for crystallization in fiber and film processing. Polytheylene is chosen as a prototypical polymer, and the methods used are extensible to other crystallizable polymers as well. This approach entails all of the following objectives:

(1) Identification of an appropriate atomistic model for alkanes and polyethylene. This model must be complex enough to appropriately model polyethylene chains in both a melt and crystal state, yet simplistic enough to make the problem tractable by molecular simulation techniques. The criterion for model selection should be that it is based on fundamental knowledge, with no adjustable parameters. This goal must also include identification of the best model for the crystal surface. In addition, this step bears impact on the selection of the technique to use for dynamic modeling, molecular dynamics or Langevin dynamics, since the inherent assumptions of these techniques are valid only when the atomistic model meets certain conditions.

(2) Implementation of the molecular simulation, to predict crystal growth rates and study the physical mechanisms underlying secondary nucleation. Analysis techniques to be explored include: torsional bond distributions, rates of torsional flips, radial distribution functions, overall changes in chain orientational order, overall changes in density, and spatial fluctuations in local order and density. In addition, some insight should be gained regarding the mechanisms involved in chain crystallization, and the elementary processes taking place.

(3) Model parameterization for a crystallization growth rate model, such as Ziabicki's Gaussian model. The model must retain its connection to molecular structure by extracting meaningful rate parameters based on the simulation results, with the goal being to provide rate data that could be used in a continuum level model of crystallization during fiber or film processing. In addition, the insight gained from simulation data at different temperatures and molecular weights will allow for the refinement of the crystallization growth rate model. The atomic scale information provided by simulation should be used to parameterize a phenomenological model of polymer crystal growth. This model should account for both temperature and molecular weight dependence but should not rely on experimental sources to parameterize chemical constants. To our knowledge, this is the first such attempt to parameterize a crystallization rate equation from a molecular model.

(4) Validation of simulation results by comparison to existing crystallization data. This must primarily mean comparison to experimental data for phase transition points.

Comparison with kinetic data must also be attempted, despite the fact that observed crystallization rates in isolated systems are often too slow to compare to nano-scale simulation times. In fiber processing, when fast crystallization is observed, the complexity of the fiber morphology and rheology during the fiber drawing prevents us from extracting crystallization rates. Validation should also include comparison of the growth rate model to current existing growth rate models.

(5) Extension of results to a simplified model for polymer crystallization. The key features of polymer crystallization will be extracted to create a simplified model for crystallization, to be implemented in a kinetic Monte Carlo algorithm that can capture the essentials of the crystallization process. Validity of the model should be proven by comparison to the detailed simulation results.

For these purposes, the remainder of this thesis is organized as follows. Chapter 2 will outline the background, both experimental and theoretical, recent developments in alkane forcefields, and recent advances using simulation. Chapter 3 will present our approach to the development of the atomic model and simulation techniques. The initial set of simulations on n-eicosane will be discussed in Chapter 4. This is followed in Chapter 5 by presentation of the relevant results in simulations of other molecular weight alkanes. Chapter 6 will highlight the retooling of the crystallization model based on simulation results. Then, Chapter 7 will suggest an extension of the alkane model to polymers, based on the fundamental understanding developed from the simulations. In addition, Chapter 8 will present a simplified algorithm for modeling polymer

crystallization using kinetic Monte Carlo. Finally, a summary of this work will be presented in Chapter 9, and some recommendations for future research in this field and improvements based on what we have learned.

Chapter 2

State of the Art

2.1 Experimental Observation of Crystallization

Knowledge of the morphology of semi-crystalline polymeric material has proven important in understanding the mechanical properties of a material [Lin and Argon 1994; Al-Hussein et al. 2000]. For several processes including fiber spinning and injection molding, high-speed crystallization is taking place in the presence of orienting stresses and rapid cooling, making the study of these systems complex. There are several studies that have attempted to account for crystallization for specific engineering problems, including the melt-spinning work of Ziabicki to the injection-molding studies of van Krevelen [Ziabicki 1976; van Krevelen 1978].

Several techniques have also been used to gather information on crystallization in drawn fibers. Atomic force microscopy studies have revealed the interlocking of lamellae in shish-kebab crystalline domains [Hobbs et al. 2001], the crystallographic planes of orthorhombic polyethylene [Snetivy et al. 1992], and even a granular substructure that may indicate that a lamella forms initially through planar crystal blocks [Heck et al. 2000]. Transmission electron microscopy has revealed the differences from

quiescent growth in the lamellar microstructure due to increasing shear rates [Hosier et al. 1995].

In addition, a great number of x-ray diffraction studies also have been conducted on crystallizing polymer melts. Wide angle X-ray studies (WAXS) recently revealed that the onset of crystallization does not occur until the removal of stress from the system [Blundell et al. 2000; Mahendrasingam et al. 2000]. Small angle X-ray studies (SAXS) have revealed information about the lamellar crystallite and amorphous interphase thicknesses [Stribeck et al. 1995]. Several simultaneous small- and wide-angle X-ray studies have been conducted in the last several years to determine what happens in the initial stages of crystallization. Some studies have suggested that there is an induction time between the emergence of SAXS peaks and WAXS peaks, indicating that large scale density fluctuations, consist with spinodal decomposition, are a precursor to the crystalline phase [Imai et al. 1994; Ryan et al. 1999; Sasaki et al. 1999; Heeley et al. 2003]. Other work has suggest that the nucleation and growth mechanisms are best to describe polymer crystallization, either explaining the induction time as an issue of apparatus sensitivity or presenting evidence of no induction time at all [Kolb et al. 2000; Schultz et al. 2000; Somani et al. 2000; Wang et al. 2000].

With so much complexity in in-situ processing measurement, another approach has been to observe rates and mechanisms in the absence of these complicating factors. However, even for the relatively simple case of quiescent isothermal crystallization of polyethylene (PE), there still remain several unanswered questions about the mechanisms of melt crystallization.

Early work by Keith and by Keller, among others, revealed the complex morphology of polymer systems [Keller 1955; Keith 1964]. In quiescent systems, it was shown that a spherulitic structure develops, in which lie layers of twisting, stacked lamellae separated by layers of amorphous polymer. The formation of folded lamella ewas a clear indication that this process was kinetically-limited, as thermodynamics would prefer fully-extended chains. Thus the kinetics of growth has been a subject of study for many years. Mandelkern showed that the temperature dependence of the spherulitic growth rate is consistent with crystal growth controlled by secondary nucleation, which led to study of the lamellar growth rate and the mechanisms that cause the formation of lamellae [Mandelkern 1958].

One approach to studying growth is to examine single crystal lamella, either grown from solution, or isolated from the melt, as illustrated in Figure 2.1. This has allowed for detailed examination of lamellar thickening growth as a function of the undercooling of the system below the melt temperature, ΔT [Hikosaka et al. 2000; Hocquet et al. 2002]. In addition, some studies in high pressure regimes have revealed a high pressure hexagonal phase for polyethylene which exhibits higher mobility in the chain direction than the orthorhombic phase [Rastogi et al. 1991; Hikosaka et al. 1997].

The structure of single crystal lamellae have been shown to reveal regular folded structures, for solution-crystallized lamellae [Bassett et al. 1959], and more recently, for melt-crystallized lamellae, when the crystallization temperature is near the melting temperature [Bassett et al. 1988]. Direct measurement of lamellar growth in the lateral direction for isolated lamellae has only been possible near the melt-temperature [Bassett et al. 1988; Toda 1992; Okada et al. 1998; Tian et al. 2004]. However, the temperature

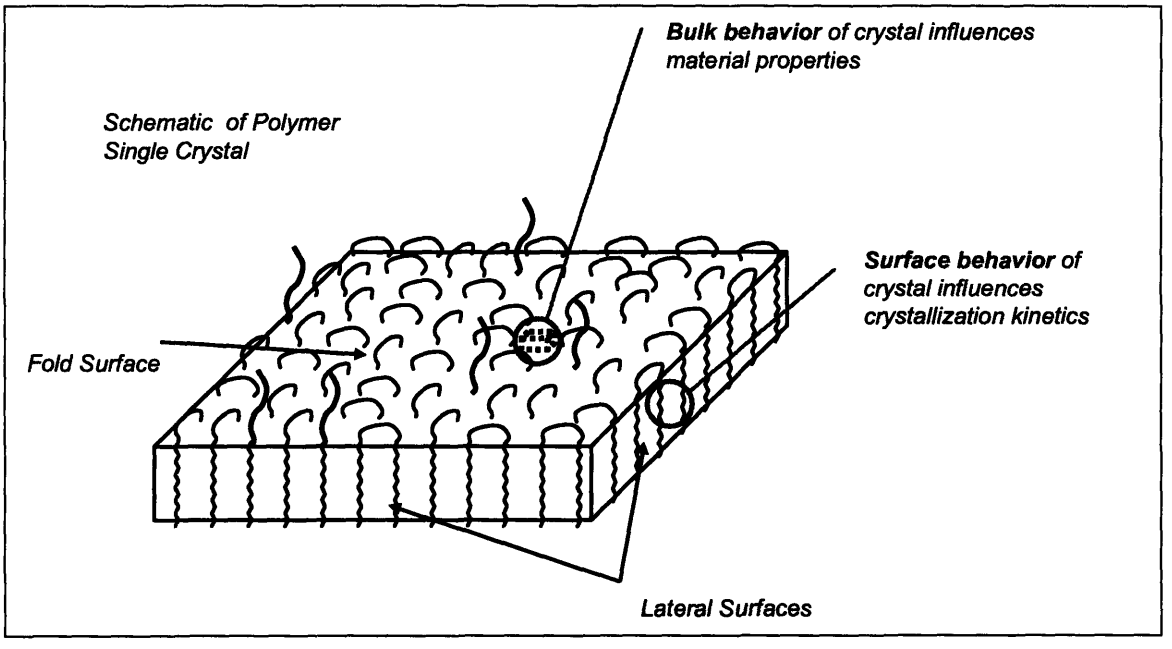

Figure 2.1 Schematic of Polymer Single Crystal.

range of these measurements is far higher than the quenching seen during processing, rendering the growth rate data of little use for this application. Furthermore, it is not at all clear whether the mechanisms that cause regular chain folding in the melt are viable at high undercoolings.

The alternative method for measuring growth rates is to measure the spherulitic growth rate directly, as was done for polyethylene by Hoffman *et al.* [Hoffman et al. 1975], and for a variety of other polymers by Mandelkern *et al.* [Mandelkern et al. 1968]. Both studies were unable to capture a range of undercoolings wide enough to reach the maximum crystallization rates. However, more recent studies of polyethylene have been able to approach the maximum rate [Ratajski and Janeschitz-Kriegl 1996; Wagner and Phillips 2001]. Perhaps the widest range of data that has been examined with kinetic theory is for poly (p-phenylene sulfide) [Lovinger et al. 1985], but a large amount of data for different polymers has been collected by Gandica and Magill, which verifies the form of Ziabicki's empirical curve [Gandica and Magill 1972].

Substantial studies have also been done of short and long alkane systems, as a surrogate for polyethylene. However, much of the work revolves around the onset of chain folding and its impact on the final morphology. Hosier and Bassett observed that pseudo-spherulitic structures formed from once-folded C246 [Hosier and Bassett 2000]. For smaller undercoolings, the kinetics of extended chain growth were shown to increase linearly with undercooling. Several studies have shown that non-integral folded (NIF) crystals form as a precursor to integral folded (IF) crystals at small undercoolings, indicating that the NIF structures, though not thermodynamically favorable, grow faster than IF structures [Ungar and Keller 1987; Cheng et al. 1992; Alamo et al. 1994].

Again, these results were attained for small undercoolings and may not translate to processing conditions.

A great deal is also known about crystallization of short alkanes. They have been shown to exhibit a mobile rotator phase at high pressure [Sirota et al. 1994]. Recent studies of homogenous nucleation have shown that chains as short as C25 begin to exhibit polymer-like behavior in their undercoolings and surface energies, perhaps indicating the crossover from extended chain nucleation to a chain-bundle nucleation [Kraack et al. 2000; Kraack et al. 2000]. The melting behavior for several n-alkanes is well-known [Small 1986]. Techniques have been developed for the growth of large (centimeter-scale) single-crystals of n-alkanes, allowing for growth measurements at temperatures near the melting point [Narang and Sherwood 1980; Yoon et al. 1989]. However, even less growth data exists for a wide range of undercoolings than exists for polyethylene, because the crystallization of crystals occurs faster and is more difficult to observe optically.

2.2 Theoretical Modeling of Crystal Growth Rates

A few well-known trends in polymer crystallization have led to the development of complex polymerization theories. Phenomenologically, one observes a maximum growth rate at a temperature intermediate between the glass transition temperature T_g and the melt temperature T_m [Gandica and Magill 1972; Ziabicki 1976]. This arises as a competition between a thermodynamic driving force towards crystal growth, associated with locking chains into crystallographic registry and which is rate limiting at high temperatures, and the ability of chains to diffuse to the new layer and rearrange

themselves conformationally to satisfy the restrictions of crystal symmetry, which is rate limiting at low temperatures.

In addition, growth rate behavior near the melting point has been studied particularly. While growth rates exhibit a linear dependence on the undercooling, there are discrete changes in the slope of the growth rate, which are believed to be due to a change in the mechanism of surface nucleation [Hoffman and Weeks 1962; Armistead et al. 1992]. Studies of molecular weight effects on growth rates have revealed that with increasing molecular weight, growth rates decrease for the same undercooling [Hoffman et al. 1975; Hoffman and Miller 1997; Okada et al. 1998; Umemoto et al. 2002]. These trends are illustrated in Fig. 2.2.

In experiment and modeling of the kinetics of alkane crystallization, focus has been concentrated on growth rates very near the melting temperature, where the growth of these systems is optically observable. In this temperature range near T_m, diffusion is not a limiting factor, which has led to theory that accurately models the thermodynamic driving force, and its effect on kinetics [Hoffman and Weeks 1962; Mandelkern 1964]. This also allows for studying the effects of chain length, by considering its effects on the melting temperature. However, since our interest is in processing conditions over a large range of temperatures, previous models for alkane crystallization kinetics do not suffice since they generally do not account for the reduced mobility at low temperature [Nozaki and Hikosaka 2001]. Models for the kinetics of polymer crystallization are more capable of capturing this temperature dependence, because it is a combination of thermodynamics and the constraints of diffusion and chain connectivity that lead to the unique chain-folded lamellar structure of melt-crystallized polymers. However, molecular weight

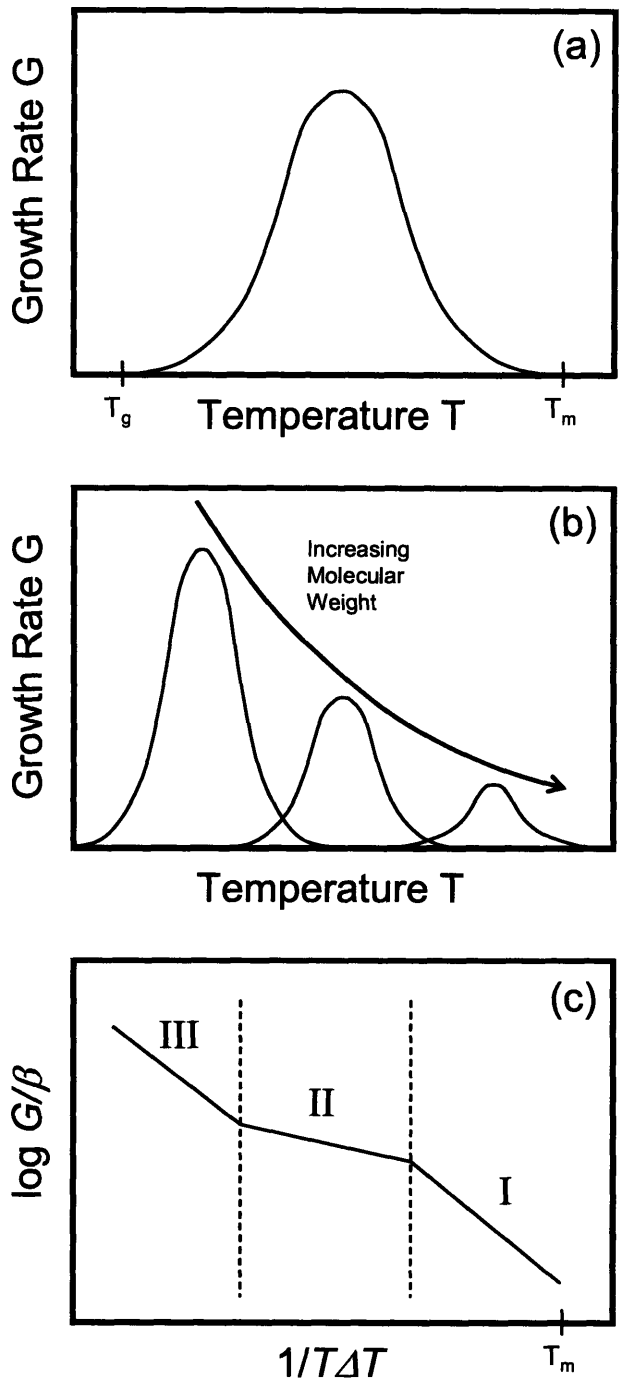

Figure 2.2 Observed trends in polymer crystal growth. (a) Dependence of growth rates on temperature found in polymer processing. (b) The effect of molecular weight on the growth rate curve. (c) The three observed regimes of growth that are seen close to T_m in laboratory growth experiments, graphed according Hoffman's rate equation, Eq. (2.4); different slopes reveal different nucleation barriers. (c) adapted from Armistead and Goldbeck-Wood 1992.

dependence is not as relevant for the growth rates of long, entangled chains, and therefore polymer growth rate models do not often have explicit molecular weight dependence.

Several previous models have been suggested to account for the temperature dependence of polymer linear growth rates, based on different approaches. Based purely on empirical evidence, Ziabicki modeled the dependence by using a simple Gaussian function, as shown below

$$G = G_{\max} \exp\left[-4 \log 2 \frac{(T - T_{\max})^2}{D^2} \right] \tag{2.1}$$

where G_{max} is the maximum growth rate, T_{max} is the temperature at which it occurs, and D is the half-width of the Gaussian curve; this has become the standard model in polymer fiber processing [Ziabicki 1976]. There are several other approaches that have invoked a combination of theory and empirical fitting. Gandica and Magill noted that a corresponding states equation existed for crystallization kinetics, whereby almost all data could be reduced to a dimensionless "master curve," described by the maximum growth rate, the melt temperature, and the glass transition temperature [Gandica and Magill 1972]. Recent work by Umemoto and Okui, has extended this approach by using theory to yield a general analytical form for the master curve and solving for the maximum growth rate as a function of molecular weight [Umemoto and Okui 2002]. Van Krevelen followed a similar approach, using both theory and empirical data to develop the following equation for the rate:

$$G = G_0 \exp\left[-C_D \frac{T_m^{\,2}}{T(T_m - T_g)} \right] \exp\left[-\frac{C}{T}\left(\frac{T_m}{T_m - T} \right) \right] \tag{2.2}$$

where G_0 is 10^{12} nm/s, C_D is a dimensionless constant with a value of approximately 5 for most polymers, and C is a characteristic constant for every polymer, containing the ratio of the surface energy of a nucleus to the lattice energy gained by crystallization. In this equation, the competing forces of secondary nucleation and thermal diffusion are described in terms of T_m, the thermodynamic melting point of a perfect crystal, and T_g, the glass transition temperature where diffusive motion is arrested, respectively. However, he was unable to find a value for C_D that would model satisfactorily the diffusion term over the entire range of undercoolings [van Krevelen 1978].

Purely theoretical approaches have invoked classical nucleation theory, based on the work of Turnbull and Fisher [Turnbull and Fisher 1949], whereby the energy barrier can be broken down into a thermodynamic part for the formation of a critical nucleus and a diffusive part for activated diffusion to the phase boundary. This allows for the parameterization of the growth rate in terms of energy barriers to nucleation and diffusive hopping:

$$G = G_0 \exp\left[-\frac{E_D}{RT}\right]\exp\left[-\frac{\Delta G_2^*}{RT}\right] \tag{2.3}$$

where G_0 is a pre-factor, E_D is the barrier to diffusive hopping, and ΔG_2^* is the free energy required to form a critical two-dimensional surface nucleus. The most sophisticated model of secondary nucleation is that due to Hoffman and coworkers, in which the crystallization process is limited by the attachment of the first fully extended

stem to a smooth surface of the crystal [Hoffman and Weeks 1962; Lauritzen and Hoffman 1973]. Near T_m, the rate exhibits the following proportionality,

$$G = \beta \exp\left[-K_g / T\Delta T\right] \tag{2.4}$$

where β is a temperature-dependent diffusion term, K_g is the surface nucleation constant reflecting the ratio of surface energy to bulk energy difference of a critical volume, and ΔT is (T_m-T), the undercooling below the equilibrium melting temperature. This constant K_g is a consequence of general nucleation theory and is relatively independent of molecular weight, since the surface energies and free energy difference between the subcooled amorphous and crystal phase are a function of the chemical properties of the monomer unit only. Hoffman shown that close to T_m, the value of K_g changes, indicating a change in nucleation mechanism at shown in Fig. 2.2(c); three different regimes of growth have been predicted and modeled for polyethylene [Armistead and Hoffman 2002]. Shorter chain lengths favor what Hoffman termed Regime I and II growth, where deposition is occurring within a single layer. Regime I growth occurs when a single surface nucleus forms and subsequent growth occurs in the terraces of the nucleus. In Regime II growth, surface nucleation rates are sufficiently fast that multiple events of surface nucleation may occur in the same layer of growth. However, for the undercoolings relevant to processing, the phenomena observed are comparable to what Hoffman termed regime III growth, or rough growth, where surface nucleation is occurring in more than one layer, and new chains nucleate on steps, terraces, or kinks. Mandelkern developed a model based on the idea that the formation of a critical monomolecular nucleus is the limiting step in the crystallization process [Mandelkern

1964]. Binsbergen provided early criticism of both approaches [Binsbergen 1970]. Particularly, he stated that Hoffman's assumption that the critical nucleus is a fully extended chain ignores the fact that there are lower energy paths to create a new layer. Also, he questioned whether Mandelkern's assumption of an easily defined surface nucleus makes sense, in light of the random attachment and removal of segments that he believed would occur. These criticisms were consistent with theories of growth suggested by Point [Point 1979] and by Sadler and Gilmer [Sadler and Gilmer 1986], in which the crystallizing surface might sample several conformations before finding one that is stable and contributes to growth. Keller *et al.* suggested that the presence of a stable, highly mobile hexagonal phase for polyethylene at high pressure might be indicative of an intermediate mobile phase at the growth front that is capable of lamellar thickening, in addition to lateral growth [Keller et al. 1994]. More recently, Strobl has introduced a new model for crystal growth, where a layer of "granular crystals," which develop from a "mesomorphic" layer of highly ordered melt, precedes the formation of the final lamella [Strobl 2000]. None of these models are fully applicable for describing alkane crystallization rates over a wide range of temperatures and molecular weights solely using parameters that depend only on chemical architecture.

Even though these prevailing theories of polymer crystallization are based on secondary nucleation, most invoke other assumptions that are obtained by analogy to single crystal formation in dilute solution. Hoffman-Lauritzen theory uses a surface energy argument to justify the assumption that chain stems deposit on the surface fast enough to be considered a single process. Sadler's entropic barrier model incorporates the idea of molecular pinning and accounts for surface roughening. Point's model allows

for each unit to attach or detach, creating the possibility of having folds anywhere. All three theories exhibit elements of agreement with the existing experimental evidence, and remained in contention largely due to the lack of detailed, mechanistic data that might distinguish one over the others. Strobl's multi-step model, with intermediate "granular crystal layers" that merge to from the lamellar crystal, agrees with more recent experimental results for PE, including the TEM studies of Kanig, *et al.* and the FTIR work of Tashiro *et al.*, which reveal a hexagonal phase precursor to the orthorhombic form of PE [Kanig 1991; Tashiro et al. 1998]. However, Lotz commented that the crystal structure of isotactic polypropylene reveals that polymer crystallization takes place by a sequential method of deposition, where stems probe the crystal topology to determine the best conformation for registry, similar to the ideas of Sadler and Point [Lotz 2000].

Once the assumptions based on single crystal formation are noted, it is less clear what the structure of a lamella in a melt-crystallized system should look like. There are a few possible outcomes that have been mentioned in the literature; one of the main differences between them is in the approach to chain folding. One phenomenon that is observed in the case of a single chain crystallizing from dilute solution is that of tight folding, or adjacent re-entry. In this case, a chain crystallizes in a lamella of a certain thickness by folding into an adjacent lattice position. Because x-ray scattering results reveal the signatures of the lamellar part of the semi-crystalline morphology, it has been conjectured that melt-crystallized lamellae crystallize by the same method. The Hoffman-Lauritzen model of secondary nucleation in polymer assumes that the connectivity of the system will lead to this type of adjacent re-entry. However, because of the high energy associated with tight folds, it has been suggested that polymer could

crystallize in the same structure, with non-adjacent re-entry into the crystal. This idea is present in Flory's "switchboard model" for lamellar crystals [Flory 1962], and the more recent proposal of Strobl, that crystallization occurs by formation of a mesomorphic layer near the crystal surface, could also lead to this type of structure. This idea suggests the possibility of no folds at all, which is an extension to the "fringed micelle" model of crystallization, where chains don't fold, but lead into the melt phase that cannot crystallize more material, due to entanglements, although this idea has never been suggested by experiments. There could also be a "mixed" model with combination of adjacent and non-adjacent re-entry. Past and recent simulation results have shown that a distribution of tight folding, loose folding, and chain ends in the melt might be the most energetically favorable way to dissipate order and density in the interphase region between the melt and the crystal [Mansfield 1983; Balijepalli and Rutledge 1998; Gautam et al. 2000]. Figure 2.3 shows schematic representations of the three models.

2.3 Molecular Simulation of Alkanes

A useful simulation in general, and specifically for polymer crystallization, requires both a good representation of the species to be modeled and a good modeling technique. We will address recent work in both the development of interatomic potentials for alkanes and polyethylene and recent results using available modeling techniques.

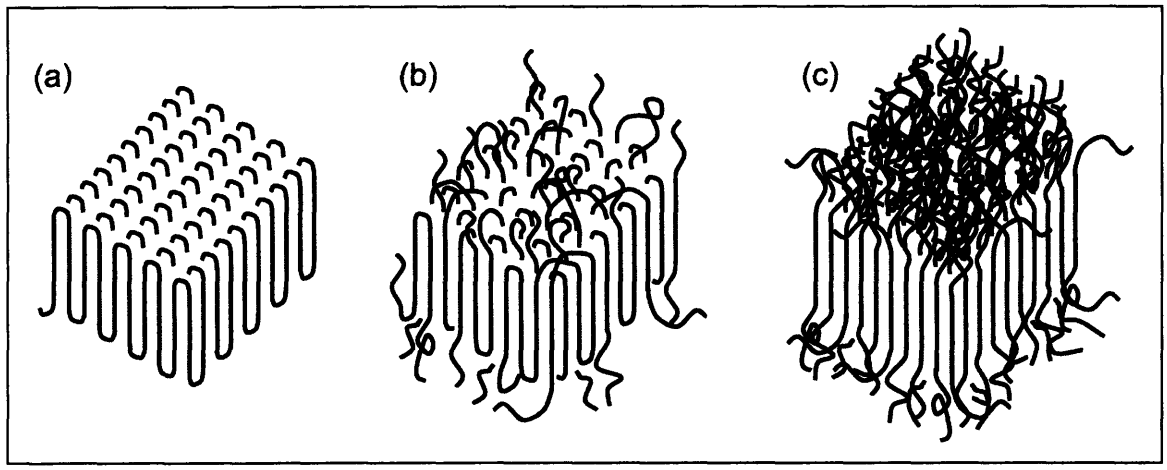

Figure 2.3 Possible models for polymer lamellar structure after melt crystallization. (a) Tight folds model; (b) A model with a distribution of different folds; (c) No folds or "switchboard" model.

2.3.1 Developments in interatomic force fields

There are several representations of atoms which fall under the category of molecular models. For polyethylene and alkanes, the most detailed representation employed is the explicit atom (EA) representation, where each carbon and hydrogen atom on the chain is individually represented. Subsequently, sources of validation are needed to verify the bond length (1-2 interactions), bond angles (1-3 interactions), torsional angles (1-4 interactions), and nonbonded interactions. A few force fields are regularly used, with differences resulting from the different experimental phenomena they attempted to match [Vacatello and Flory 1986; Sorensen et al. 1988; Karasawa et al. 1991].

Since explicit atoms simulations can be computationally costly, one simplification that is commonly made is the use of a united atom (UA) representation, where CH_2 and CH_3 groups are condensed into a single bead representation. This allows representation of alkanes and polyethylene as a chain of beads, regulated by a similar set of bond lengths, bong angles, torsional angles, and nonbonded angles, but for interactions between the CH_2 and CH_3 beads, not the carbon and hydrogen atoms. A variety of these focefields are available in the literature, as well [Ryckaert and Bellmans 1975; Rigby and Roe 1987; Mayo et al. 1990; Paul et al. 1995; Bolton et al. 1999]. It should be noted that two comparison studies between UA and EA forcefields found the chains modeled with the two methods had only slight conformational differences, but that UA forcefields overpredict diffusion, due to the lack of interatomic packing that explicit hydrogens allow [Yoon et al. 1993; Bolton et al. 1999]. There has been an attempt to correct this for long alkane melts, which yields diffusion enhanced by only 20% with UA forcefields [Paul et

al. 1995]. Therefore a cost-benefit analysis is necessary in determining the best interatomic potential for the system of interest.

There has been focus specifically on the form and strength of the torsional potential, and how they affect chain stiffness and properties [Gee and Boyd 1998; Lavine et al. 2003]. The DREIDING forcefield [Mayo et al. 1990] has become a commonly used forcefield in the simulation of alkanes and polymer chains [Kavassalis and Sundararajan 1993; Fujiwara and Sato 1998; Iwata and Sato 1999]. The DREIDING forcefield relies on orbital hybridization arguments to create three equal wells for the *trans*, *gauche plus*, and *gauche minus* states, with equal barrier heights of 3 kcal/mol for alkanes. However, it also allows 1-4 non-bonded interactions, which have little effect on the *trans* state, but significant effects of the *gauche* states and the barrier between them. The Ryckaert and Bellmans torsional potential, based on experimental data, explicitly accounted for all 1-4 interactions in the torsional potential [Ryckaert and Bellmans 1975], and has produced more realistic results [Rigby and Roe 1987; Esselink et al. 1994]. In addition, recent experimental data and ab initio calculations have led to an optimized forcefield for alkanes that can duplicate accurately P-V-T behavior for short alkane melts [Paul et al. 1995].

Finally, it is worth noting that as a compromise between EA and UA, Toxvaerd suggested an anisotropic united atom (AUA) model, noting that the points at which the CH_2 and CH_3 beads are covalently bonded are slightly shifted from the center of the non-bonded potential [Toxvaerd 1990]. Accounting for this, improvements were made to the equation of state, and the forcefield has found subsequent uses in parameterizing the

equation of state and measuring the heat of vaporization [Pant et al. 1993; Toxvaerd 1997].

Unfortunately, we are not aware of any forcefields for alkanes or polyethylene that have been parameterized for properties of both the melt phase and the crystalline phase. The UA and AUA forefields mentioned have been calibrated for melt properties, while the EA forcefields were calibrated for crystalline properties. EA forcefield parameters have been modified from the crystalline parameters to study the melt phase [Smith and Yoon 1994], but we are not aware of a forcefield that has been tested to reproduce properties of both phases.

2.3.2 Recent work with different simulation techniques

A simulation study of crystal growth rates must rely on methods that yield system dynamics, despite the fact that a great deal about semi-crystalline polymer can be learned from methods that generate equilibrium such as lattice dynamics [Lacks and Rutledge 1994; Wilhelmi and Rutledge 1996; Bruno et al. 1998] and Monte Carlo [Martonak et al. 1997; Balijepalli and Rutledge 2000; Mavrantzas and Theodorou 2000; Yamamoto et al. 2000].

The most traditional method is molecular dynamics (MD), in which the equations of motion are integrated over time, using the gradient of the configurational energy of the system. Homogenous nucleation is difficult to simulate using MD due to the induction time associated with nucleation, with rare exception [Esselink et al. 1994; Meyer and Muller-Plathe 2002]. Most studies of nucleation have found ways of accelerating dynamics, by looking at non-equilibrium systems. One way is to apply a large stress to

the system to induce amorphous orientation, and accelerate nucleation [Koyama et al. 2002; Lavine et al. 2003; Ko et al. 2004], as is seen during fiber spinning. Another method is to look specifically at chains in the vapor phase [Kavassalis and Sundararajan 1993; Yamamoto 1998; Fujiwara and Sato 1999]. Low molecular weight, chain rigidity, and orientation all appear to accelerate homogeneous nucleation of an ordered phase. Exploratory simulations of these effects are discussed briefly in Appendix A. In addition, one can simulate chains near a crystal surface, thus eliminating the need for homogenous nucleation, and focusing specifically on crystal growth [Yang and Mao 1997; Shimizu and Yamamoto 2000; Yamamoto 2001]. To our knowledge, no one has yet attempted to use molecular dynamics to attain a quantitative measure of polymer crystal growth.

Recent simulations have suggested that realistic experimental results for chains in dilute solution can be obtained using Langevin dynamics as an alternative to molecular dynamics [Liu and Muthukumar 1998]; the number of time steps required to achieve crystallization is orders of magnitude less, as well (although it is difficult to correlate with real times, since the effect of solvent in implicit). Langevin dynamics is a method of timescale separation that allows implicit representation of solvent in cases when the timescale of the solvent is faster than that of the solute. When the timescale of the solvent is smaller, its effects can be mimicked by a combination of stochastic forces and frictional drag [Allen and Tildesley 1987], where the two are connection by the general fluctuation-dissipation theorem [Van Kampen 1992]. Although altering the pathway by use of Langevin dynamics can affect the final structure of the crystal, our attempts to duplicate these simulations yielded a globule of polymer without much residual order. In addition, we found that the mobility of chains on the surface of the globule always

resulted in disorder on the surface. Furthermore, in the work by Liu and Muthukumar, the apparent distribution of torsional angles in the equilibrated uncrystallized state and the temperature of crystallization (near 600 K) do not reflect those of polyethylene. We were able to duplicate that result by stiffening the chain, by either decreasing the depth of the *gauche* wells, or allowing non-bonded forces for 1-4 interactions, as is commonly done in the DREIDING implementation of the interatomic potential. In addition, by doing so, we found that we were able to duplicate the final folded state, using either Langevin dynamics or molecular dynamics. The effects of the stiffening of the forcefield are shown in Fig. 2.4. Our attempts to use Brownian dynamics to study the high-density crystalline part of polymer systems are discussed in Appendix B.

Variations on molecular dynamics have been suggested to accelerate modeling. Some variations are designed to reduce computational time. This can be accomplished by several methods, such as decoupling the time scales of bonded and non-bonded interactions or spatial decomposition of simulation cells for parallel processing. Other approaches are based on transition-state theory. Voter has developed an array of techniques for accelerating dynamics, by specifically considering methods for rapidly identifying infrequent events and biasing the potentials to accelerate transitions [Voter 1997; Voter 1998; Sorensen and Voter 2000]. These techniques require detailed knowledge of the energy surface to locate energy wells, in order to be able to perform the simulation accurately. For polymer crystallization, where the energy surface is complex, no one has yet been able to apply this class of accelerated techniques to these systems.

Kinetic Monte Carlo (KMC) is a similar technique, also based on transition-state theory, that is designed to accelerate the modeling of dynamic processes by sampling the

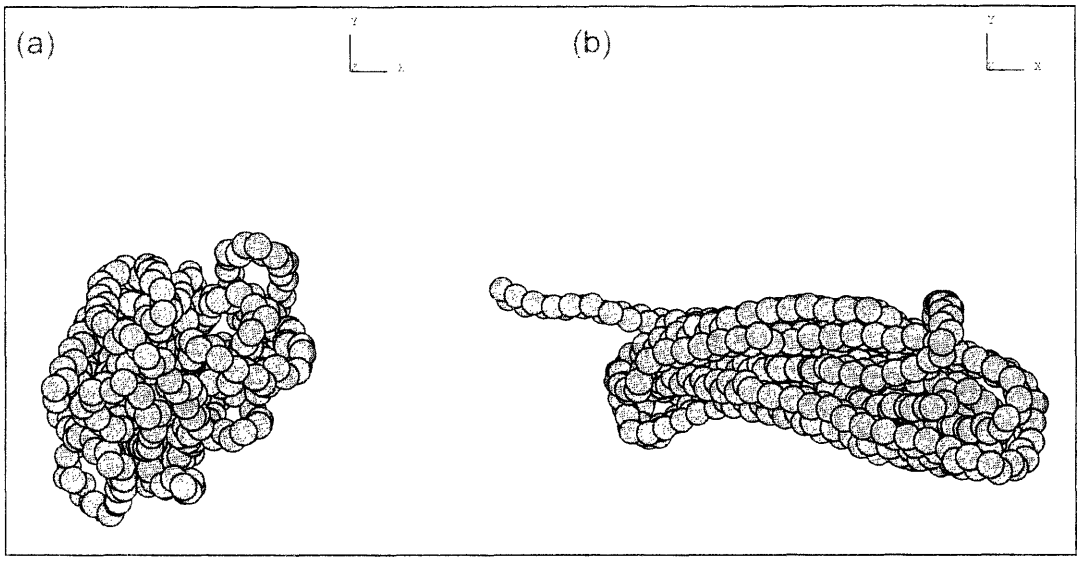

Figure 2.4 Final configurations after temperature ramping from 700 K to 500 K over 5 ns, using two forcefields. (a) Forcefield of Paul *et al.* 1995; (b) Stiffened forcefield by including 1-4 non-bonded interactions to the Paul *et al.* forcefield, which duplicates the result of Liu *et al.* 1998.

occurrence of the infrequent events [Bortz et al. 1975; Fichthorn and Weinberg 1991]. KMC requires knowledge of the mechanisms or events in the modeled system, as well as the rates at which these events occur. This simulation technique has been applied to atomic systems, such as defect clustering and dislocation glide in silicon [Cai et al. 1999; La Magna et al. 1999], but, due to the complex topology, determining events for a polymer system can be difficult. Early work focused on duplicating the Rouse behavior of amorphous polymer melts [Carmesin and Kremer 1988] and the shift in behavior near surfaces [Eisenriegler et al. 1982]. There have been a few groundbreaking works, which modeled polymer crystallization by KMC. Several of them have focused on the formation of a primary nucleus in dilute solution [Chen and Higgs 1998; Toma et al. 1998; Hu et al. 2003]. The more advanced of these simulations have allowed for the study of sectorization of crystals in three dimensions as well [Hu et al. 2003]. Models for crystal growth stemmed from a shift in approach to polymer crystallization from Hoffman's thermodynamic model to Sadler and Gilmer's "entropy barrier model." [Sadler and Gilmer 1986] Work in this area focused on the growth of single-chain crystals in two dimensions, by modeling the crystalline phase on a lattice and assuming the amorphous phase can be modeled as a "lumped state" [Sadler and Gilmer 1988; Doye and Frenkel 1998; Doye and Frenkel 1999]. However, there has been difficulty in linking the simulations to realistic polymer crystal growth rates. Goldbeck-Wood related KMC and MD rates using a two-dimensional growth model, but we are not aware of any attempts to link three-dimensional KMC simulations with growth rates from the melt phase [Goldbeck-Wood 1990; Goldbeck-Wood 1994].

One reason for the difficulty in developing a realistic KMC algorithm is the enumeration of all relevant KMC moves. Unlike traditional Monte Carlo, which may use any move that leads to a more complete sampling of phase space, kinetic Monte Carlo requires that the moves be based on physical events observed in the molecular system. Although it is possible to postulate the moves based on intuition, previous work by Voter has revealed that important moves are sometimes overlooked [Voter 1997]. Therefore, it is preferable to base moves on molecular level observations, which molecular dynamics can provide. Also, once we know which moves take place, it is necessary to know the rates for the moves, in order to link to realistic times. The ability to relate rates to actual simulation times by statistical theory is one of the main advantages of KMC.

Another subtle challenge exists in creating a simulation general enough to yield a variety of crystal structures. Most previous models have been restricted to a single chain crystallizing from a melt or dilute solution. While this is a good starting point for the application of this technique, the inevitable result is a tightly-folded polymer single crystal, which is only one of the numerous possible morphologies observed in reality. In addition, crystallization from dilute solution may not utilize the same mechanisms as melt crystallization. Without properly addressing these concerns, a simulation may drive itself to a particular result and predict it by default, rather than by a mechanistic selection of several possible outcomes.

Chapter 3

Molecular Simulation Model

3.1 Modeling Approach for Crystal Growth

The simulation technique we selected is non-equilibrium molecular dynamics (NEMD). Langevin dynamics was found not to allow for faster observation of crystallization. In addition, the assumptions inherent in Langevin dynamics include a separation of timescales, which is not appropriate for melt crystallization, since all molecules are of the same timescale.

The molecular dynamics simulations are non-equilibrium, such that we begin with an equilibrated melt, quench the system to below the melt temperature, and observe the evolution of the system to its new equilibrium state. A quenched system often stays in a metastable state for a duration before homogeneous nucleation takes place. However, the growth process is isolated in our simulations by including a potential that mimics a crystal surface at two opposing walls of the simulation. This allows for the simulation to proceed immediately to secondary or surface nucleation, without waiting for a primary nucleation event, which may have induction times on the order of the length of the simulation. In addition, the presence of a crystal surface at a known location allows

growth to progress in a recognizable direction, making the identification of the growing crystal front a geometrically simply problem.

Traditional statistical ensembles in molecular dynamics include the canonical ensemble and the isothermal-isobaric ensemble. In the canonical ensemble, the number of particles N, the volume simulation cell volume V, and the system temperature T are held constant for the duration of the simulation. In the isothermal-isobaric ensemble, the number of particles N, the system pressure P, and the system temperature T are held constant. Neither of these simulations is appropriate for the non-equilibrium simulation we are conducting. In our simulation, a constant volume simulation would not allow for the changes in density that occur as crystallization takes place in the system. Also, a constant pressure system would allow three-dimensional volume change that would prevent us from using a periodic potential to mimic the crystal surface. Therefore, we use an ensemble with a constant number of particles, a constant temperature, a constant cross-sectional area in the x-y direction, and constant stress in the z direction. With this constant $NA\sigma_{zz}T$ ensemble, we are able to allow for the volume change associated with crystallization, and at the same time, maintain the periodicity of the cell in the x and y directions. A schematic of the simulation setup is shown in Fig. 3.1.

3.2 Interaction Potential

We use a united atom polyethylene forcefield, in which chains consist of CH_2 and CH_3 beads that interact through bonded and nonbonded interactions.; this is justified since the C-H vibration is fast enough that we can consider the beads as "equilibrium units." Simulations using the anisotropic united atom forcefield were also tested, and

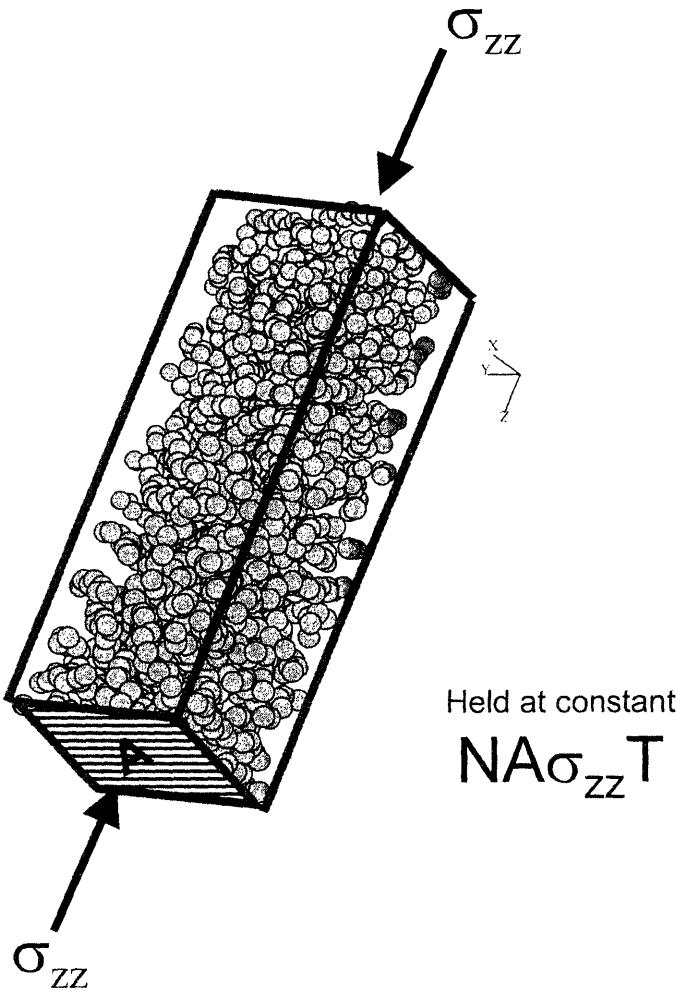

Figure 3.1 Schematic of a simulation cell; simulated surfaces are located at the *x*-*y* boundaries of the cell, which are kept constant to maintain periodic surfaces in the *x* and *y* directions.

were found to lead approximately four-fold increase in computational time, while still not being able to model the crystal structure significantly better. Both forcefields produce hexagonally packed crystal structures, instead of the orthorhombic structures found in polyethylene. The forcefield is unable to maintain a fixed setting angle in the crystal unit cell. Instead the chains have more mobility around the chain axis. Estimates of this mobility have not been tested for the crystal phase, although the effects also manifest in the amorphous phase and are discussed below. As a consequence of this inability to differentiate between these phases, we will not be able to offer validation to the ideas of Keller, discussed in Chapter 2, suggesting that the hexagonal phase is present at the growth front.

We have discussed the importance of using realistic potentials in modeling this process. Accurate values for the barriers between torsional states are essential in capturing the balance between the orienting process and the crystal packing process. It is the proper balance of these forces that allows one to determine correctly which of several credible mechanisms is the pathway to loop formation. Therefore, our research focuses on modeling the process using potentials that are well-parameterized for polyethylene. We use the interaction parameters for angles, torsions, and excluded volume interactions, calibrated by Paul *et al.*, for united atom polyethylene, where CH_2 and CH_3 beads behave identically [Paul et al. 1995]. This forcefield currently is best at duplicating the P-V-T behavior of short alkanes, and is based on the most recent experimental and ab initio calculations. The total potential E_{TOTAL} consists of several terms:

$$E_{TOTAL} = E_{BOND} + E_{ANGLE} + E_{TORSION} + E_{NONBOND} + E_{SURFACE} \tag{3.1}$$

The harmonic bond length potential E_{BOND} for bonded atoms is given by

$$E_{BOND} = k_b(r - r_{eq})^2 \tag{3.2}$$

where k_b = 350 kcal/(mol Å^2) and r_{eq} = 1.53 Å. The harmonic bond angle potential E_{ANGLE} for atoms separated by two bonds is given by

$$E_{ANGLE} = k_\theta(\theta - \theta_{eq})^2 \tag{3.3}$$

where k_θ = 60 kcal/(mol rad^2) and θ_{eq} = 1.91 rads (109.5°). The torsional or dihedral potential $E_{TORSION}$ for atoms separated by three bonds is given by

$$E_{TORSION} = \tfrac{1}{2}k_1(1 - \cos(\varphi)) + \tfrac{1}{2}k_2(1 - \cos(2\varphi)) + \tfrac{1}{2}k_3(1 - \cos(3\varphi)) \tag{3.4}$$

where k_1 = 1.6 kcal/mol, k_2=-0.867 kcal/mol, and k_3=3.24 kcal/mol. The zero-point for the torsional angle φ is the *trans* state. All interactions between atoms separated by three bonds are explicitly accounted for in the torsional potential. For atoms separated by more than three bonds and for intermolecular atoms, the non-bonded potential $E_{NONBOND}$ is modeled by the Lennard-Jones relation:

$$E_{NONBOND} = 4\varepsilon[(\sigma/r)^{12} - (\sigma/r)^6] \tag{3.5}$$

where the well depth $\varepsilon = 0.112$ kcal/mol and the zero-energy atomic radius $\sigma = 4.01$ Å, and with a 12 Å interaction cutoff. These parameters have been tested by Paul *et al.*, for structure and dynamics for the melt phase, but not the crystal phase.

To model the secondary nucleation process specifically, we create two crystal surfaces on the *xy*-planes of the simulation cell. To represent the initial crystal surface, we use the surface potential previously calibrated for Lennard-Jones beads by Steele [Steele 1973]. The potential used in our simulation is an exponential fit to the Steele potential, which uses the same Lennard-Jones parameters from the non-bonded interactions. The potential is periodic in the *x* direction, with a wavelength of 4.33 Å, and in the *y* direction with a wavelength of 2.5 Å. This creates a [110]-like surface that is corrugated in *x* and *y*. The *y*-direction corresponds to the *c*-axis of the crystal. The crystal exhibits hexagonal packing normal to the *c*-axis of the crystal. In Steele's formulation, the surface interaction has been calibrated by integrating over an infinitely thick crystal lattice. Therefore, its effective ε is 9 times stronger than the bare carbon-carbon interaction. The potential is divided into two parts:

$$E_{SURFACE}(x,y,z) = U_0(z) + U_1(z)\left[\cos\left(\frac{2\pi x}{\lambda_x}\right) + c_y\left(1 - \cos\left(\frac{2\pi y}{\lambda_y}\right)\right)\right] \tag{3.6}$$

where the crystal periodicity in the *x* direction $\lambda_x = 0.433$ nm, the periodicity in the *y* direction $\lambda_y = 0.125$ nm, and the strength of the relative strength of the *y* corrugation to the *x* corrugation $c_y = 0.1$. The terms $U_0(z)$ and $U_1(z)$ are the first two components of a Fourier series that Steele derived to capture the effects of an infinite crystal; the higher

order terms are neglected. The potential $U_0(z)$ is an attractive potential similar to the Lennard-Jones potential, given by

$$U_0(z) = \frac{2\pi\varepsilon}{\lambda_x r_0}\left(\frac{2\sigma^{12}}{5z^{10}} - \frac{\sigma^6}{z^4} - \frac{\sigma^6}{3d(z+z_c)^3}\right) \tag{3.7}$$

where ε and σ are the Lennard-Jones parameters, the displacement of the underlying layer $r_0 = 0.125$ nm, the z-distance to the next underlying layer $d = (\text{sqrt}(3)/2)\lambda_x$, and $z_c = 0.61d$, as given in Steele's formulation. $U_1(z)$ is a repulsive potential that represents the translational barrier in the x and y directions. In Steele's formulation, it is given by

$$U_1(z) = \frac{4\pi\varepsilon}{\lambda_x r_0}\left(\frac{\sigma^{12}\pi^5}{30(z\lambda_x)^5}K_5\left(\frac{2\pi}{z\lambda_x}\right) - \frac{2\sigma^6\pi^2}{(z\lambda_x)^2} - K_2\left(\frac{2\pi}{z\lambda_x}\right)\right) \tag{3.8}$$

where K_2 is a modified Bessel function of the second kind, and K_5 is a modified Bessel function of the fifth kind. To ease in computation, we conducted a numerical non-linear least squares fit to this function, in the region to 0.3 nm (where the energies are sufficiently high) to 1.2 nm (the cutoff distance), using the parameters for our system, and replaced Eq. (3.8) with the following equation,

$$U_1(z) = \frac{4\pi\varepsilon}{\lambda_x r_0}\left(c_1 \exp\left(-c_2\frac{z}{\sigma}\right)\right) \tag{3.9}$$

where $c_1 = 7.122 \times 10^4$ and $c_2 = 16.31$. Our functions for $U_0(z)$ and $U_1(z)$, given by Eq. (3.7) and Eq. (3.9), respectively, are shown in Fig. 3.2. The total surface potential $E_{SURFACE}(x,y,z)$, given by Eq. (3.6) is shown for the x-z plane and x-y plane in Fig. 3.3.

3.3 Simulation Details

In this work, we employ molecular dynamics in the presence of a surface potential to study physical mechanisms underlying the growth process. We attempt to observe growth rates for short alkanes such as n-eicosane ($C_{20}H_{42}$, denoted as C20) over a range of quench temperatures. This scenario is similar to that described by Eder *et al.*, where a supercooled crystallization zone precedes the physical crystallization front, when heat transfer occurs faster than the characteristic time for crystallization [Eder et al. 1990]. Because we only assume the system is thermally equilibrated in the range of a few nanometers, our simulation would be applicable to both cases presented by Eder, the large crystallization zone in which a supercooled slab crystallizes slowly, or the narrow crystallization zone in which crystallization occurs rapidly.

A simplified heat balance adapted from Eder and Janeschitz-Kreigl is include to justify the isothermal assumption for the melt near the growth front. The heat created by the crystallization is balanced by the heat removed from the boundary through the melt, shown in the following one equation:

$$\lambda\left(\frac{\partial T}{\partial x}\right) = \rho h \frac{dx_c}{dt} \tag{3.10}$$

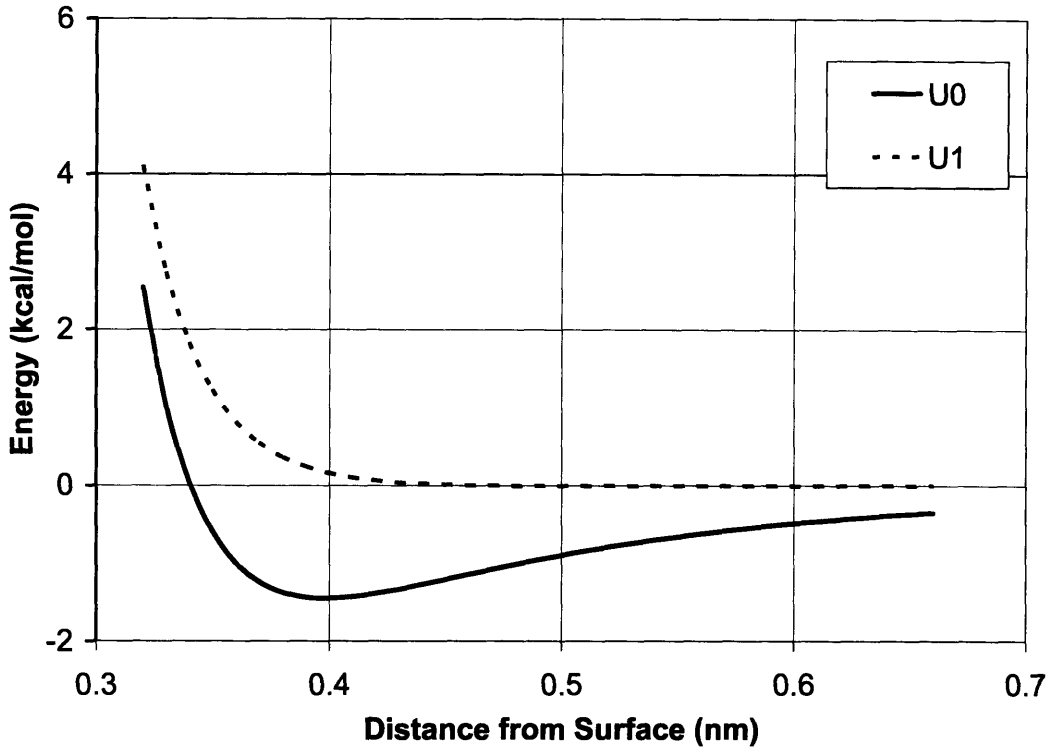

Figure 3.2 Two components of the Steele potential; U_0 is an attractive potential that is the first Fourier component of the cumulative effect of the Lennard-Jones beads in the surface, and is solely a function of z, the distance from the surface; U_1 is a repulsive potential that is the second Fourier component, and is the translational barrier in the x and y directions.

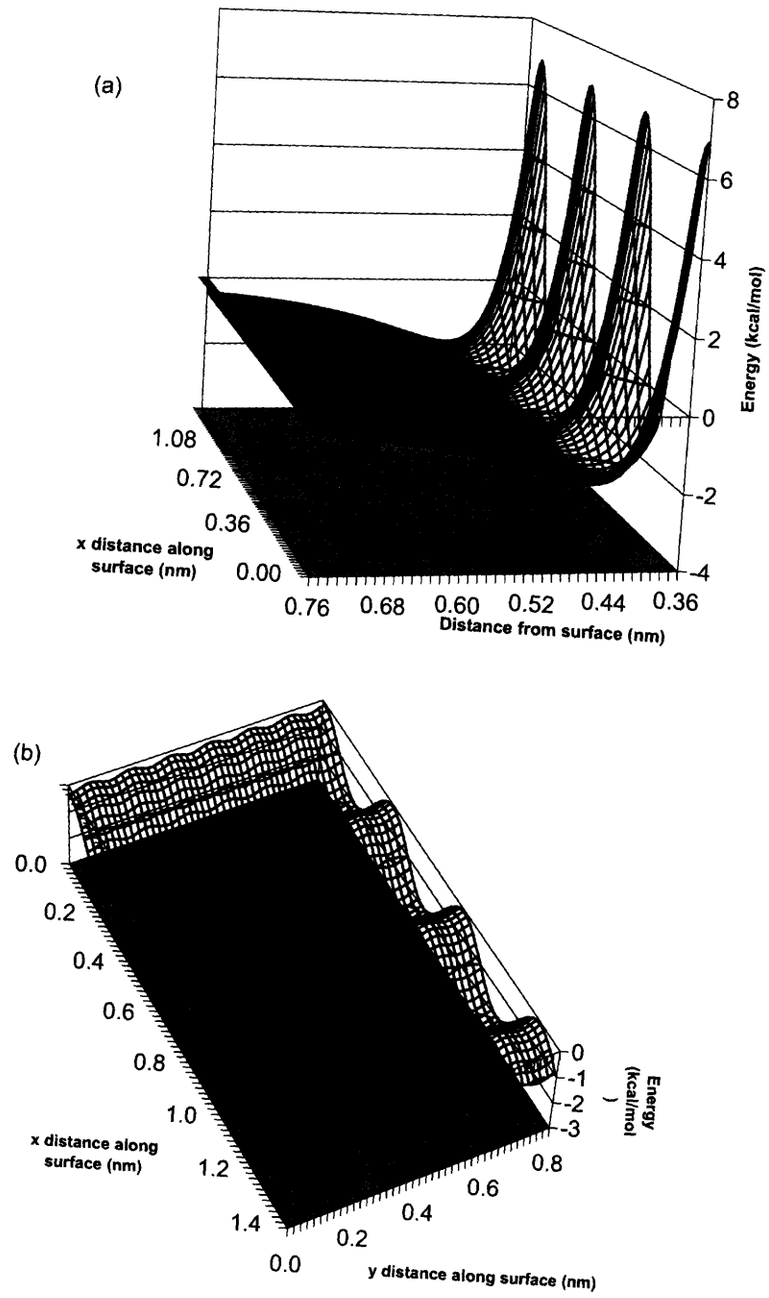

Figure 3.3 Two dimensional projections of our implementation of the surface potential. (a) The energy of the potential in the *xz*-plane at y= 0.5 nm; (b) the energy of the potential in the *xy*-place at z=0.4 nm.

where λ is the thermal conductivity, T is the local temperature, x is the direction normal to the surface, ρ is the crystal density, h is the latent heat of crystallization, and x_c is the location of the crystallization front. The term for heat transfer into the crystalline phase is dropped to determine the limiting case where all heat is transported back into the melt phase. Density change is also not considered, and the upper limit of crystal density is assumed, providing the maximum heat generation. For the example of C20, we use a thermal conductivity of 0.1522 W/(m K) [Vargaftik et al. 1996], a crystal density of 0.9361 g/cm^3, and a latent heat of crystallization of 16.8 kcal/mol [Small 1986]. Assuming that the growth front moves at approximately 0.1 m/s (as is seen near the maximum crystallization rate for C20), we can compute the gradient of temperature into the melt phase $\partial T/\partial x$ at the growth front to be approximately 1.5 x 10-4 K/nm. Over a typical simulation size of 10 nm in the direction of the surface normal, this temperature change is insignificant. Therefore, we may assume our simulation system is isothermal, when using a value for the thermostat that allows for fast heat removal. This allows us to calculate parameters for a Ziabicki-type rate equation, which is temperature dependent, yielding isothermal growth data.

We then consider systems of the longer alkanes $C_{50}H_{102}$ and $C_{100}H_{202}$, denoted C50 and C100, for the purpose of studying the molecular weight dependence of the crystal growth rate and to investigate additional characteristics of the growth process, such as chain folding, that are observed in polyethylene crystallization, but that are not observed in the C20 simulations. It is worth noting that these simulations are considerably more time-consuming than those for C20, not only due to the larger simulation cells required in order to avoid artifacts of the finite simulation cell size, but

also due to the longer simulation times required in order to capture the slower crystallization kinetics. Despite these limitations, molecular dynamics, through its resolution on the atomic length scale, provides information that cannot be obtained through any other source.

Initial configurations were generated at a reduced density of 0.3 g/cm^3 by growing each polymer chain with fixed bond lengths, fixed bond angles, and a torsional state of *trans*, *gauche plus* or *gauche minus*, selected according to probabilities generated from a Boltzmann weighting of the torsion angle potential at 400 K, discretized into the three rotational isomeric states. Overlap during chain construction was avoided by rejecting any steps that resulted in interatomic distances less than 5 Å during initialization; in the event that numerous unsuccessful attempts to grow a chain were encountered at the n-th united atom, it was deleted and the process started again from the n–1'th atom, until all atoms were successfully placed.

The initial simulations consist of 102 n-eicosane chains in a box of fixed x and y dimensions to match the periodic boundary conditions of the x- and y-corrugated surface potential. In the z direction, the box dimension (the distance between the surfaces) is held at a constant stress of 1 atm, in order to accommodate the volume change associated with thermal contraction and crystallization. The initial box size is 20.0×20.0×90.0 Å and, after building using the above-described method, was allowed to equilibrate to bulk density at 400K and 1 atm for 1 ns. After equilibration, the identical C20 samples were quenched to 225 K, 240 K, 250 K, 260 K, 265 K, 275 K, 285 K, 290 K, 295 K, and 300 K.

Subsequent simulations consist of 42 C50 chains, or 40 C100 in a box of fixed x and y dimensions. In the z direction, the box dimension (the distance between the surfaces) is held at a constant stress of 1 atm. The initial box size for the C50 simulations is 25.9×65.0×39.3 Å, and The simulation cell was then equilibrated to bulk density using molecular dynamics at 400 K and 1 atm for 1 ns. The C100 simulations start from a simulation cell that is 52.0×80.0×31.3 Å, after being equilibrated for 1 ns at 500 K. After the equilibration phase, the systems were quenched below the melting point to begin the crystallization process. Identical C50 samples are quenched to 290, 300, 315, 330, 345 and 360 K. C100 samples were quenched to 350, 375 and 400 K.

The forces are integrated using a Velocity-Verlet integration method [Swope et al. 1982], as shown,

$$\mathbf{r}(t + \delta t) = \mathbf{r}(t) + \delta t\, \mathbf{v}(t) + \tfrac{1}{2}\delta t \mathbf{a}(t) \tag{3.11}$$

$$\mathbf{v}(t + \delta t) = \mathbf{v}(t) + \tfrac{1}{2}\delta t[\mathbf{a}(t) + \mathbf{a}(t + \delta t)] \tag{3.12}$$

where $\mathbf{r}(t)$ is the position vector at time t, $\mathbf{v}(t)$ is the velocity vector at time t, and $\mathbf{a}(t)$ is the acceleration vector at time t, which is computed from Newton's law, where the forces are the negative of the gradient of the interatomic potential. We use an integration time step δt of 5 fs. A preliminary run using C20 was conducted with an integration time step of 1 fs, to evaluate the errors associated with the larger time step. Using a 5 fs time step results in an increase in the magnitude of the bond energies and angle energies by approximately 10%. There is negligible effect on the torsional and Lennard-Jones interactions. The chain orientation autocorrelation functions were computed, and the

relaxation times increased by approximately 10%. The use of a thermostat (see below) mitigates the consequences of using a large time step. No effects in the dynamics of the crystallization, or in the calculated rates, were detected. The large time step aids in looking at longer the long time scales required for secondary nucleation.

Constant temperature and stress are maintained using velocity and position rescaling as described by Berendsen et al. [Berendsen et al. 1984]. Simulations were also tested using the Nose thermostat [Nose 1984], but it was found to be too unstable for the range of temperature quenches and phase changes occurring in the system; so Berendsen's algorithm was chosen. The thermal and volume inertial time constants used were 3.3 ps and 5.0 x 10^3 ps, respectively. A factor of two increase or decrease in the inertial time constants results in less than 5% change in the relaxation time estimated from the chain orientation autocorrelation function, suggesting that the observed crystallization kinetics are relatively insensitive to the dynamics of the thermostat and barostat employed at these values.

3.4 Metrics for Measurement of Crystallization

To monitor the progress of the simulation, we use two order parameters, the first based on density and the second based on orientation. The "zero-th order" measure of phase change is a change in density. We define an "atomic density" as the inverse of the volume attributable to a single atom. Rather than a van der Waals volume, we use a 3D Voronoi tessellation of space based on atom positions, which uniquely and completely divides up the system volume into polyhedra comprising the space nearest to each atom,

as shown in Fig 3.4. Any point within a polyhedron is closer to its associated atom than to any other atom in the system. We use the algorithm of Gerstein, *et al.* [Gerstein et al. 1995]. The densities ($1/V_i$) calculated for each atom are then smeared in the z-direction using convolution to create a density profile of the system at any point in time. The distribution of local density data is given by

$$f_\rho(z,t) = \sum_{i=1}^{n} \frac{V_0}{V_i(t)} \delta(z - z_i) \tag{3.13}$$

where V_0 is the Voronoi volume of a crystal at absolute zero, based on analysis of classical lattice dynamics simulations [Lacks and Rutledge 1994], and V_i is the volume given for the atom by Voronoi tesselation. The local density for a particular slice z is obtained by only considering atoms within the box function $g(u_i)$:

$$g(u_i) = \begin{cases} 0 & -\infty < u_i < -\frac{\mu}{2} \\ 1/\mu & -\frac{\mu}{2} < u_i < \frac{\mu}{2} \\ 0 & \frac{\mu}{2} < u_i < \infty \end{cases} \tag{3.14}$$

where μ is the convolution width. The local density at z is computed by considering atoms within the range of the convolution width, $[z-\mu/2, z+\mu/2]$. This is done by convolving $f_\rho(z,t)$ with $g(u)$, yielding

$$P(z,t) = \int_{-\mu/2}^{\mu/2} \frac{1}{\mu} \sum_{i=1}^{n} \frac{V_0}{V_i(t)} \delta(z - z_i - u) du \tag{3.15}$$

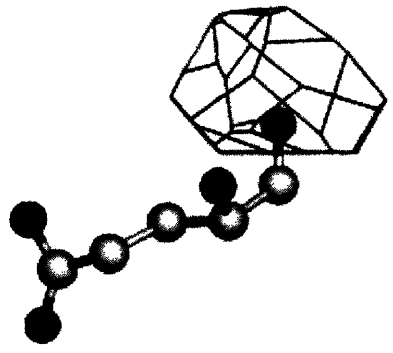

Figure 3.4 Schematic of Voronoi polyhedra, applied an atomic system. Adapted from Gerstein webpage: http://bioinfo.mbb.yale.edu/geometry/.

In order to obtain an average, analogous to the system density, we also need to know the density of beads at z at time t, given by $n(z,t)$, the convolution of an atomic distribution data with $g(u_i)$:

$$n(z,t) = \int_{-\mu/2}^{\mu/2} \frac{1}{\mu} \sum_{i=1}^{n} \delta(z - z_i - u) du \tag{3.16}$$

Now $\rho(z,t)$, the local density parameter, is given by

$$\rho(z,t) = \frac{P(z,t)}{n(z,t)} \tag{3.17}$$

The value μ controls the volume over which data is averaged. For μ=L_z, the system thickness in the z-direction, one recovers the system density. The function is normalized to yield $\rho(z)$=1 for a crystal at absolute zero, which yields a $\rho(z)$ in the range of 0.75 to 0.8 for an amorphous state for our temperature range for 225 K to 300 K. Because of large fluctuations that the Voronoi volume yields in any given snapshot, an analogous convolution was performed in time over a 1 ns box function, using snapshots at 10 ps intervals.

Another measure of phase change that has become a standard for polymer systems is orientational order. The order parameter used to measure this is the global bond orientation parameter at time t,

$$S(t) = \frac{3\left\langle \left[\nu_i(t) \cdot \nu_j(t) \right]^2 \right\rangle}{2} - \frac{1}{2} \tag{3.18}$$

where $\mathbf{v}_i(t)$ is the orientation vector of atom i at time t, defined by the chord from atom i-1 to atom i+1, and the average is taken over all pairs i and j. However, in order to calculate the spatial distribution of order within the simulation cell, a local orientation order must be defined, using convolutions of the local chain orientation vectors with spatial box functions.

The orientational order at a particular z value and time t is a function of the distribution of local order data $\mathbf{f}_v(z,t)$ as described below,

$$\mathbf{f}_v(z,t) = \sum_{i=1}^{n} \nu_i(t)\delta(z - z_i) \tag{3.19}$$

where z_i is the z-component of the position vector of atom i. For convolution, we use a box function $g(u_i)$

$$g(u_i) = \begin{cases} 0 & -\infty < u_i < -\frac{\mu}{2} \\ 1/\mu & -\frac{\mu}{2} < u_i < \frac{\mu}{2} \\ 0 & \frac{\mu}{2} < u_i < \infty \end{cases} \tag{3.20}$$

where μ is the convolution width. The orientation order density at z is computed by considering pairs of atoms within the range of the convolution width, $[z-\mu/2, z+\mu/2]$. This is done by convolving $\mathbf{f_v}(z,t)$ with $g(u_i)$ and $g(u_j)$, yielding

$$s(z,t)=\frac{3}{2}\left[\int_{-\mu/2}^{\mu/2}\int_{-\mu/2}^{\mu/2}\sum_{j=1}^{n}\sum_{i=1}^{n}\left(\nu_i(t)\cdot\nu_j(t)\right)^2\frac{1}{\mu^2}\delta(z-z_i-u_i)\delta(z-z_j-u_j)du_i\,du_j\right]-\frac{1}{2} \quad (3.21)$$

In order to obtain an average, analogous to the global orientational order parameter $S(t)$ in Eq. (3.18), we also need to know the density of pairs of beads at z at time t, given by $n(z,t)$, the convolution of an atomic distribution data with $g(u_i)$ and $g(u_j)$:

$$n_2(z,t)=\int_{-\mu/2}^{\mu/2}\int_{-\mu/2}^{\mu/2}\frac{1}{\mu^2}\sum_{j=1}^{n}\sum_{i=1}^{n}\delta(z-z_i-u_i)\delta(z-z_j-u_j)du_i du_j \quad (3.22)$$

Now $S(z,t)$, the local orientational order parameter, is given by

$$S(z,t)=\frac{s(z,t)}{n_2(z,t)} \quad (3.23)$$

Choosing $\mu=L_z$, the simulation cell z dimension, reduces Eq. (3.23) to the global bond order parameter $S(t)$, as defined in Eq. (3.18), while choosing a small value, such as $\mu=$ 0.5 nm, as we have usually done, yields $S(z,t)$, the orientational order parameter at a particular location z at time t. An analogous convolution was performed in time over a 1

ns box function, using snapshots at 10 ps intervals, in order to filter fluctuations caused by individual bond and angle movements.

Other metrics that we employ include volume change of the entire system, radial distribution functions, percentage of *trans* torsional states, and distribution of sequences of *trans* torsional states. We define the radial distribution function as the distribution of distances between atoms, which is given by

$$g(r) = \frac{V}{4\pi r^2 N^2}\left\langle \sum_{i=1}^{N}\sum_{j\neq i}^{N} \delta(r - r_{ij}) \right\rangle \tag{3.24}$$

where N is the number of atoms in the system, V is the system volume, and r_{ij} is the distance between any two atoms i and j. We define a torsional state as a *trans* state if the torsional angle lies between $-\pi/3$ and $+\pi/3$, where the maximums in the *trans-gauche* barriers are. In addition, we study the simulations visually, by using Xmol molecular viewer and the CAEFF Genmol viewer for viewing primary and secondary structure.

Other metrics were also explored, including atomic density, atomic energy density, radial orientation distribution, rates of torsional flip, radius of gyration of chains, and mean-square-displacement of atoms. While these are useful metrics for different applications, we found that for determining the rate of crystal growth, the movement of the density and orientational order fronts were most relevant.

Chapter 4

Application of Molecular Dynamics to n-Eicosane

4.1 Simulation Description

We begin with two types of simulations with n-eicosane. The first one is a melting simulation, where the temperature increases, in order to characterize our expected melting point. The second type is the undercooled crystallization simulations, which are isothermal, in order to calculate rates, which follow the methodology we described previously in Chapter 3. As mentioned before, the molecular dynamics technique allows us to integrate the gradient of the configurational energy of the system over time. We use a united atom polyethylene forcefield, in which chains consist of CH_2 and CH_3 beads; this is justified since the C-H vibration is fast enough that we can consider the beads as "equilibrium units." We employ an interatomic potential for united-atom polyethylene calibrated by Paul, Yoon, and Smith (PYS) [Paul et al. 1995].

In both simulations a surface potential is present at the *x-y* planes of the simulation cell. In the melting runs, the initial crystal structure of the cell is hexagonal-packed to match the surface potential. Melting begins with the homogeneous nucleation

of the melt phase in the crystal, which is allowed by the variability of the pressure in the z-direction, with a 1 atm pressure exerted on this surface.

All eicosane simulations consist of 102 n-eicosane chains in a box of fixed x and y dimensions to match the periodic boundary conditions of the x- and y-corrugated surface potential. In the z direction, the box dimension (the distance between the surfaces) is held at a constant stress of 1 atm, in order to accommodate the volume change associated with crystallization. For the melting runs, the initial simulation cell consists of 17 layers consisting of 6 eicosane chains each, equilibrated at 200 K. For the crystallization runs, the initial box size is 25.98 Å by 28.75 Å by 90 Å; they are built randomly at a density of 0.3 g/cm^3, and then allowed to equilibrate to bulk density for 1 ns. To check for finite size effects in our simulations, we tested a simulation cell with an x-y area four times as large, and found no difference ingrowth behavior within the error of the simulation. The forces are integrated using a Velocity-Verlet integration method, with an integration time step of 5 fs. The simulation is conducted at constant temperature, constant length in x and y dimensions, and constant stress of 1 atm in the z-dimension. Constant temperature and stress are maintained using velocity and position rescaling as described by Berendsen *et al.* [Berendsen et al. 1984]. The thermal and volume inertial time constants used were 3.3 ps and 5.0 x 10^3 ps, respectively.

4.2 Simulation Results

The melting point of the n-eicosane crystal structure was determined in a simulation with a constant heating rate of 0.0125 K/ps from 200 K to 500 K. The initial structure was an n-eicosane crystal with hexagonal packing, as opposed to the triclinic

phase observed experimentally. The simulation cell consists of 102 molecules, in 17 layers of 6 fully extended chains equilibrated for 1 ns at 200 K. Figure 4.1 shows the density change that occurs as temperature is increased over an interval of 24 ns. The discontinuity at 345 K marks the melting transition from crystal to liquid. The experimentally-determined melting point for n-eicosane is 310 K [Kraack et al. 2000]. The higher calculated T_m is due to the fast heating rate and to the fact that real materials usually melt from the surface inward, whereas our simulation must, by construction, nucleate a melt phase within the crystal itself. The linear thermal expansion coefficient of the crystal and of the liquid, estimated from linear fits shown in Fig. 4.1(a), are 1.736 x 10^{-4} K^{-1} and 1.002 x 10^{-3} K^{-1}, respectively. This is in close agreement with experimental values for the thermal expansion of liquid n-eicosane of 8.6 x 10^{-4} K^{-1} found by Small [Small 1986]. The crystal value is in good agreement with the lattice dynamics results of Lacks and Rutledge for polyethylene (α_a= 1.43 x 10^{-4} K^{-1}, α_b= 0.845 x 10^{-4} K^{-1} at 300 K) [Lacks and Rutledge 1994]. Davis *et al.* report experimental values of α_a=2.07 x 10^{-4} K^{-1} and α_b=0.645 x 10^{-4} K^{-1} for linear thermal expansion of polyethylene lateral to the chain axis at 300 K [Davis et al. 1970]. Closer inspection of the crystal phase behavior reveals an apparent second order transition in thermal expansion around 290 K, as shown in Fig. 4.1(b). No corresponding transition is observed in the order parameter or *trans-gauche* torsional distribution at this temperature. The significance of this transition will be discussed later.

Careful inspection of the melting run seems to indicate that there is a transition that occurs in the crystal phase, shown in Fig. 4.1(b), before the phase change that occurs at 345 K. This transition, which occurs at approximately 290 K, is evidenced by the

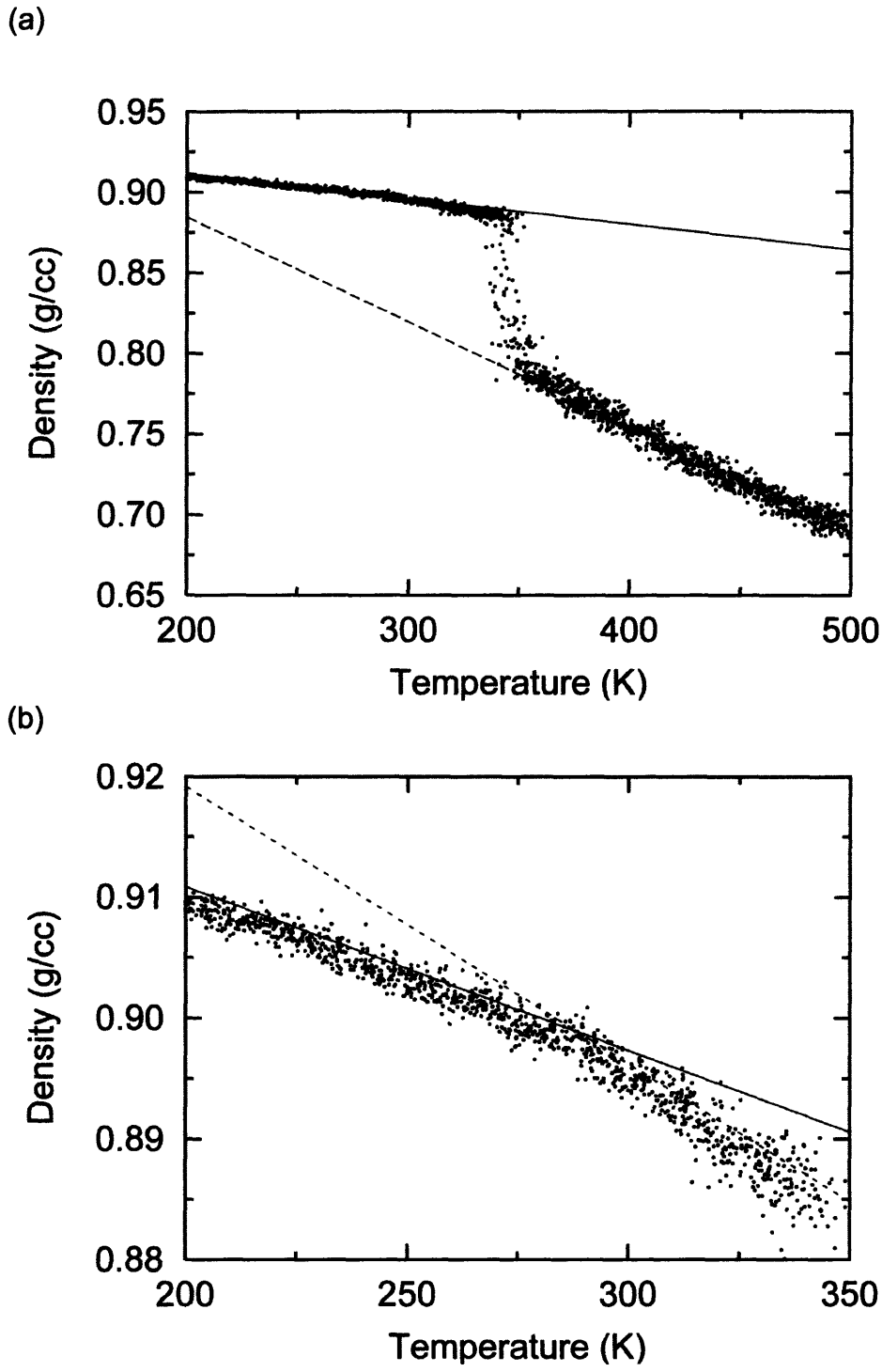

Figure 4.1 Density of the simulation cell as a function of temperature, during heating at a rate of 0.0125 K/ps, starting from the crystal phase, (a) Density variation for entire simulation run; (b) magnification of the density variation in the vicinity of the melting transition for the same run. Linear fits to the data are shown to illustrate trends: crystal (solid line); melt (long dashed); intermediate phase (short dashed).

change in the thermal expansion coefficient of the crystal. While individual chain angles were not monitored, this change in thermal expansion is consistent with the observation of a plastic-crystalline rotator phase in n-eicosane by Kraack *et al.* [Kraack et al. 2000]. This is a phase where order is exhibited in the position and orientation of the chain along its axis, but not in orientation of the molecule about the chain axis.

Furthermore, there is no discontinuity in the first derivative of the *trans-gauche* torsional ratio or the global order parameter, which is in accordance with a transition to a rotator phase. It is also of note that isothermal crystallization at temperatures greater than 295 K were not only slower, but exhibited multilayer growth and melting, a phenomenon not observed at lower temperatures. These large-scale stochastic events also made calculating rates difficult for temperatures above 295 K. The increased melting and growth may be due to the onset of rotator dynamics, which may lower the barrier to nucleation, but decrease the stability of the extended chains.

Next, isothermal crystallization simulations were conducted. An n-eicosane melt was equilibrated at 400 K, and then quenched to a temperature below the simulated melting point of 345 K. The system begins a gradual transition from an amorphous to a crystalline structure, in which the n-eicosane chains become fully extended and arranged in a hexagonal packed structure. The crystallization transition is notably slower than the corresponding melting transition. Figure 4.2 shows snapshots of the simulation as the phase change progresses through the cell. Crystallization fronts begin at both surfaces and progress to the center of the cell.

The crystallization can be characterized by the conversion of torsional states from a Boltzman distribution of *trans* and *gauche* states, in the melt phase, to predominantly

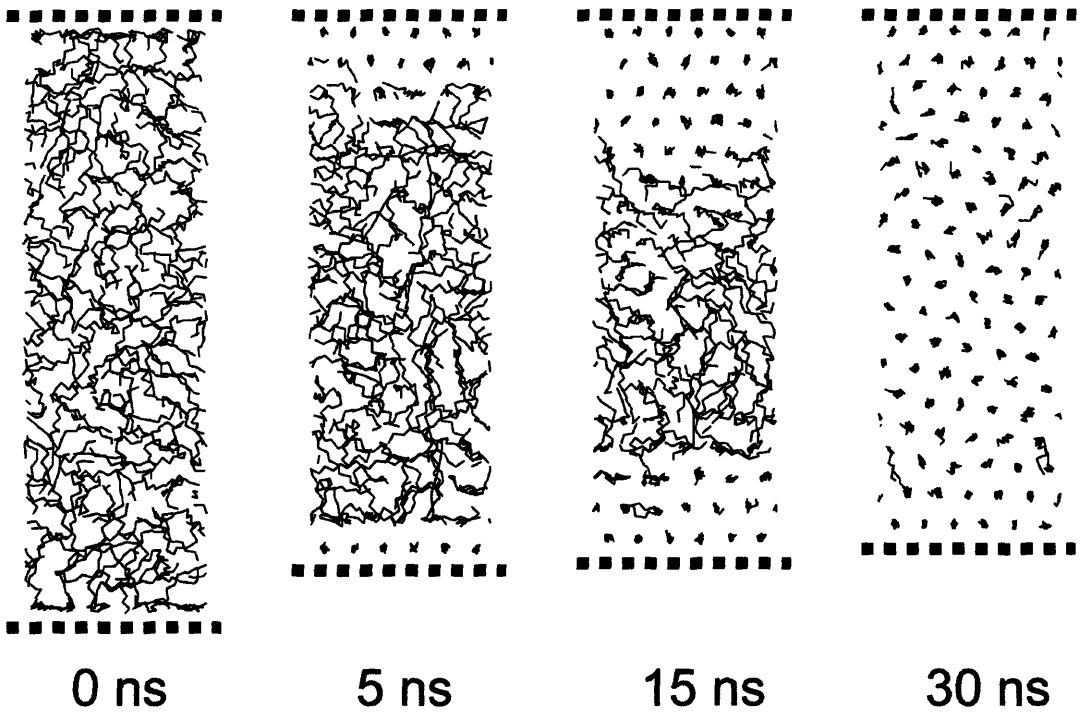

Figure 4.2 Snapshots from a simulation of 102 n-eicosane chains between two surface potentials quenched from 400 K to 285 K at t=0 ns, and then allowed to evolve dynamically at 285 K. Thick dashed lines are representative of location of surface potentials.

trans states, in the crystal phase. Figure 4.3 shows the conversion to *trans* states and the associated volume change for isothermal crystallization at 285 K. Following the initial sharp volume change associated with the thermal contraction of the melt between 400 K and 285 K, one observes the more gradual decrease in volume caused by the phase change as high density crystal replaces lower density melt. The latter volume change is accompanied by the simultaneous increase in *trans* states, which can pack into the crystal structure. Furthermore, the change in the radial distribution function over time reveals the onset of crystal packing as the broad amorphous peak is converted to sharp crystalline peaks, as shown in Fig. 4.4.

Finally, we also note that in a few cases we observed crystallization with one or more layers oriented such that the *c*-axis in the layer is inclined in the *x*-*y* plane at an angle with respect to the *c*-axis imposed by the Steele potential. At 250 K, several layers formed with the chain axis in the *x*-direction rather than the *y*-direction, where previous layers had formed. These misoriented crystalline layers occurred in runs where the temperature was near or below T_{max}, and the thermodynamic driving force for crystallization was high. In addition, at 275 K, a new layer formed in which the chains were tilted by 18 degrees with respect to the *y*-direction. This new layer is consistent with the observed triclinic phase of n-eicosane, which displays a γ lattice angle of 107.4°, with α and β values close to 90° [Luth et al. 1974]. Once the new layer formed, subsequent layers were in registry with the new layer, forming the triclinic crystal structure. The simulation cell size is long enough to allow for full extension of the chain, which does not bias the cell to either the triclinic or hexagonal structure. In addition, the periodicity

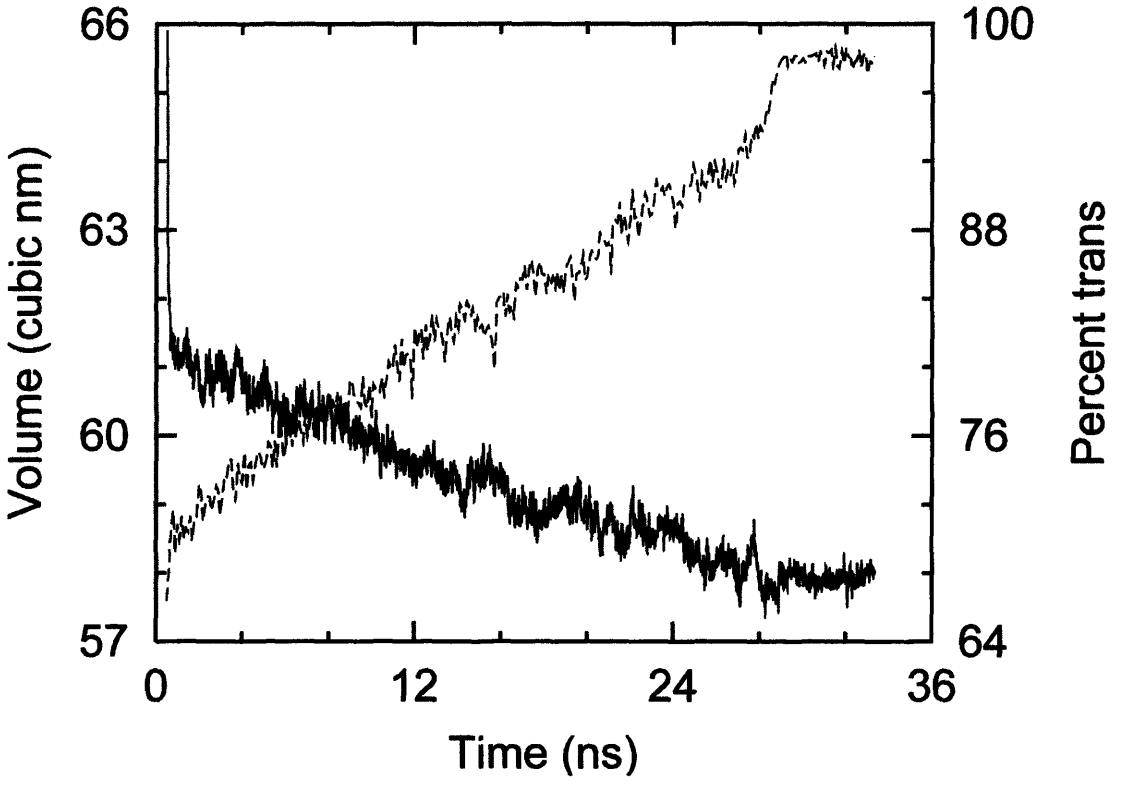

Figure 4.3 Simulation cell volume (solid line) and percent of torsions in the *trans* state (dashed line) during isothermal crystallization of 102 n-eicosane chains at 285 K. The rapid drop in volume near t=0 is due to quenching the system from 400 K.

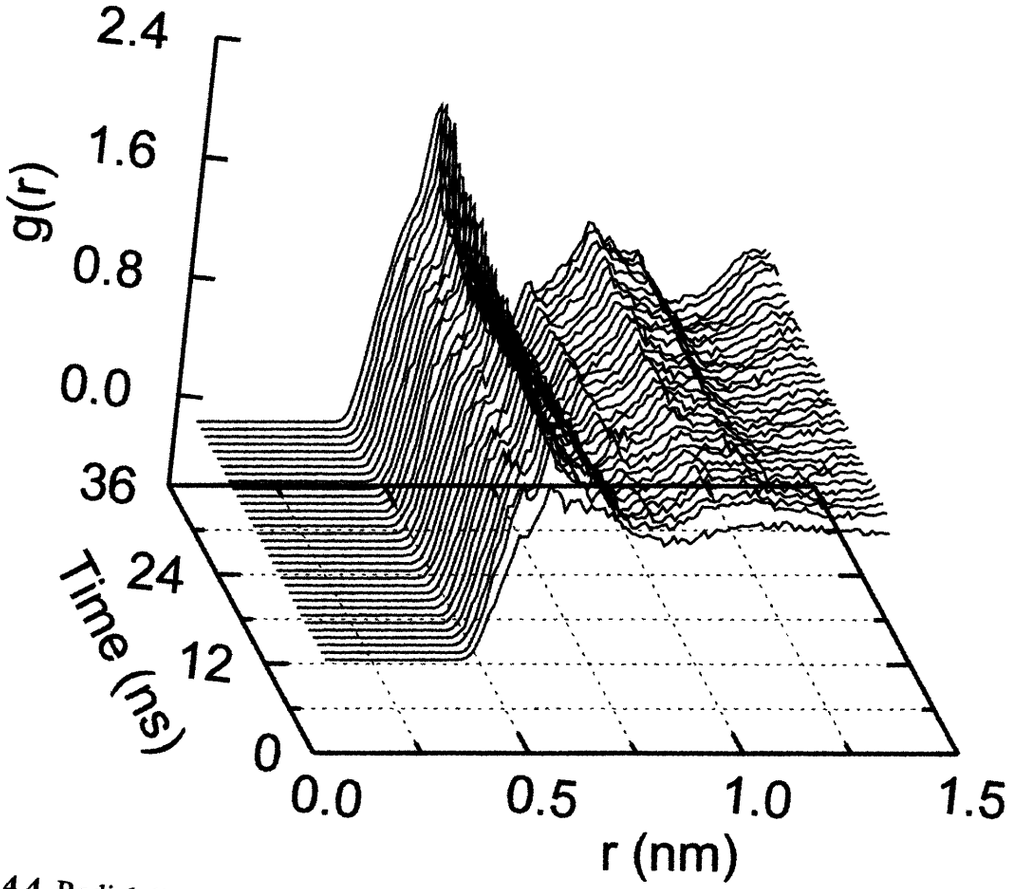

Figure 4.4 Radial distribution function $g(r)$ vs. r as a function of time, in a crystallizing simulation cell of 102 n-eicosane chains at 285 K.

in the x and y directions allows for a cell shape that does not influence the selection of one of these two crystal phases.

4.3 Order and density fronts

The orientational order parameter for the system exhibits a change from near 0.0, for a completely disordered state, to 1.0, for a completely ordered state by the end of the simulation, with chains fully extended and aligned. By choosing a σ of 10 Å and δz of 1 Å, we obtained order fronts as a function of z, for each time interval. Figure 4.5(a) shows the time evolution of the $S(z)$ profiles for the system isothermally crystallized at 285K. The location of the $S(z)$=0.5 contour is highlighted, as a guide to the eye. Because two surfaces are present, two estimates for the growth front movement are obtained by simulation. A similar time evolution of the $\rho(z)$ profiles at 285 K is shown in Fig. 4.5(b), with the $\rho(z)$=0.5 contour highlighted. The Voronoi analysis, however, is noisier, making it harder to obtain reliable fits for the order transition fronts (as described below) than is the case for orientational order profiles. Thus, results based on density profiles were computed over a restricted range of space and time, and are reported here only where reliable.

The order fronts were fit to a function that models each of the two fronts with a hyperbolic tangent, using a Levenberg-Marquardt non-linear least squares algorithm, e.g.:

(a)

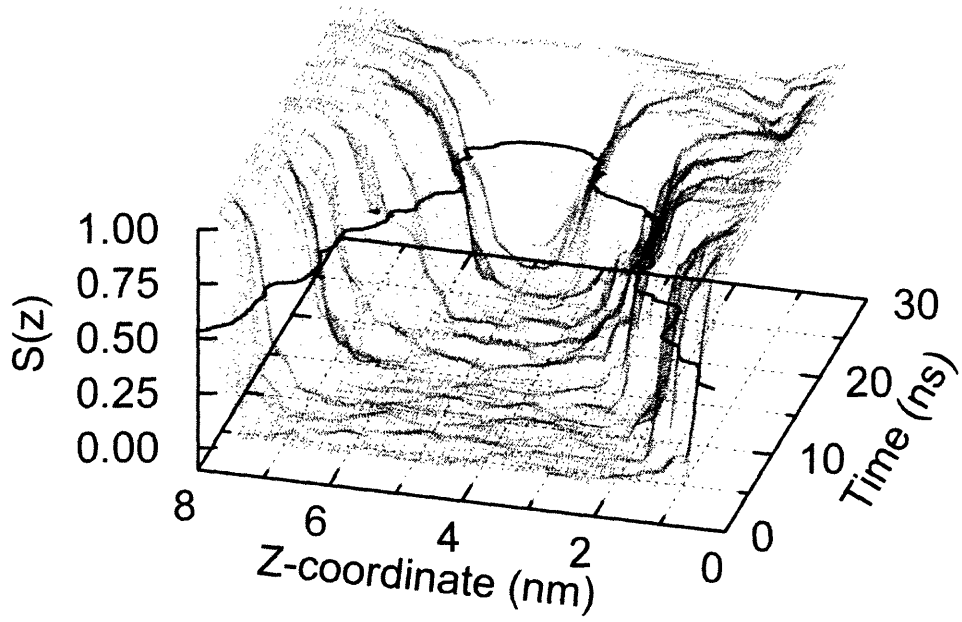

(b)

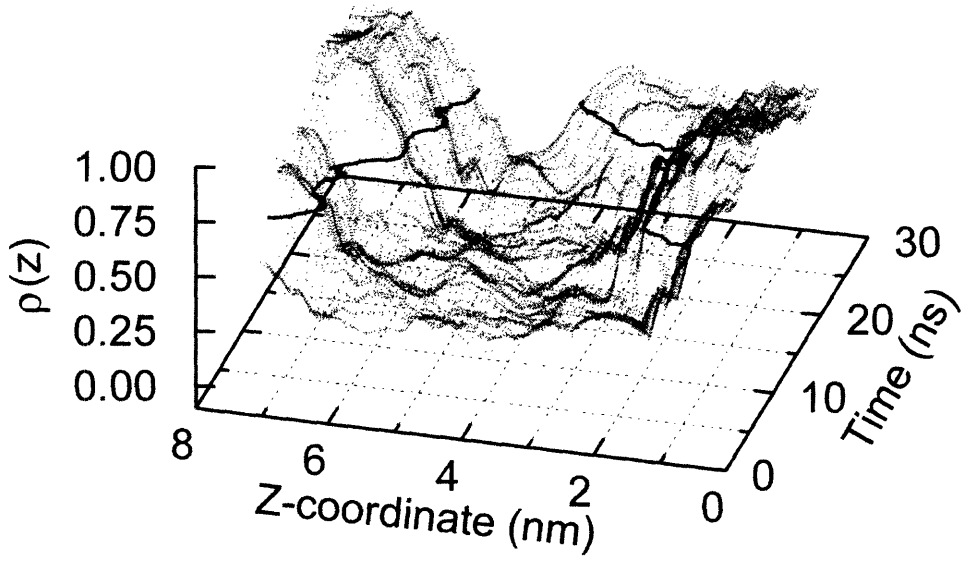

Figure 4.5 Progression of the growth front for 102 n-eicosane chains isothermally crystallized at 285 K. The z-coordinate is the direction normal to the surface. In each case, the contour at which the order parameter is halfway between the crystal and melt values is highlighted. Data has been normalized to the range from the minimum to the maximum value of the order parameter, for plotting purposes. (a) Orientational order $S(z)$; (b) packing density order $\rho(z)$.

$$S(z) = H_1 - 0.5(H_1 - L)\left[1 + \tanh\left(\lambda_1(x - \zeta_1)\right)\right] + 0.5(H_2 - L)\left[1 + \tanh\left(\lambda_2(x - \zeta_2)\right)\right] \quad (4.1)$$

where H_i is the asymptotic value of the order parameter for the crystal growing at surface i, L is the asymptotic value of the order parameter for the amorphous phase between surfaces, λ_i is the interfacial width of phase boundary i, and ζ_i is the inflection point, or the midpoint, of phase boundary i. In computing Eq. (4.1), the data was averaged over 1 ns to allow for relaxation of any instantaneous chain orientation in the amorphous phase. An example of the fitting of order front $S(z)$ is shown in Fig. 4.6, after 20 ns of isothermal crystallization at 285 K. The translation of the inflection point along the z-direction provides a measure of the growth of the crystal. From each simulation, we obtain two estimates of the crystallization rate based on change in orientational order, one for each front, and two estimates of the crystallization rate based on change in density (packing order). The positions of the inflection points in both orientational order and density are shown in Fig. 4.7, averaged over both surfaces. From the slopes of these curves, we obtain estimates of the linear growth rate. At very short times, the rigidity and approximate nature of the Steele surface perturb the growth rate, resulting in faster crystallization initially, while at long times the impingement of the two growth fronts near the center of the cell influences the data in that range. Excluding results from both the first 10 Å and last 10 Å of crystallization, we obtain growth rates of 0.107 m/s and 0.114 m/s, based on orientational order and density, respectively. While these values are orders of magnitude higher than those of polyethylene, they are reasonable for C20,

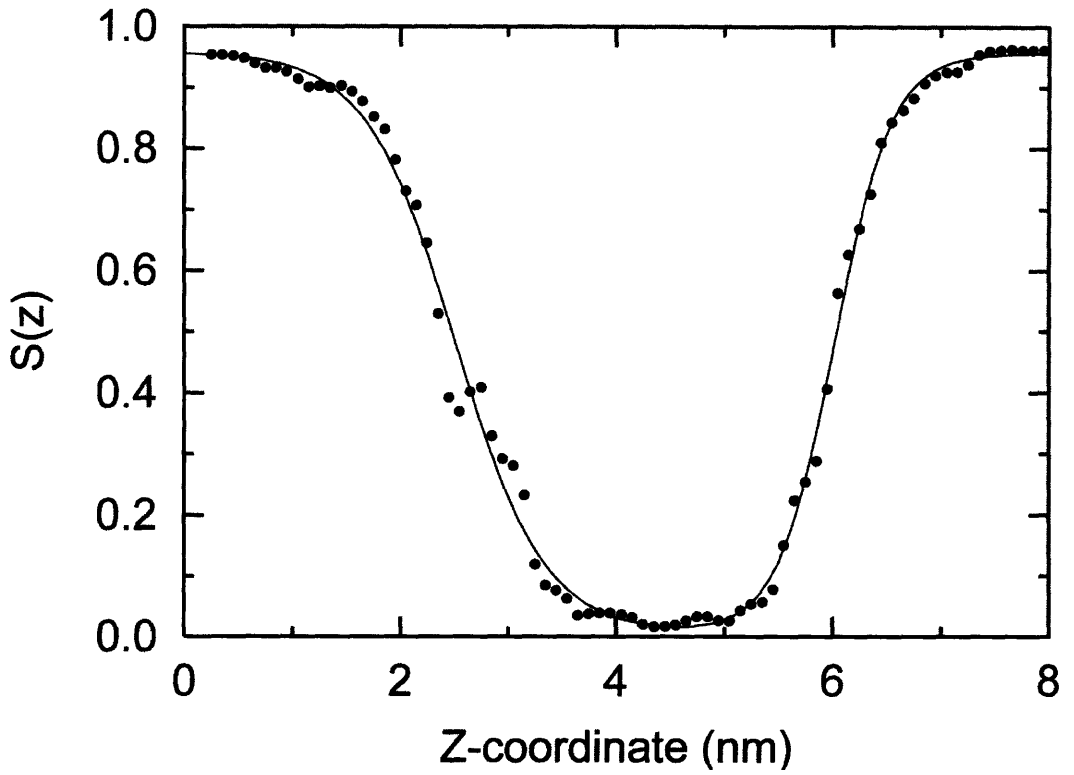

Figure 4.6 Order parameter $S(z)$ after 20 ns of isothermal crystallization at 285 K. The curve is a non-linear least squares fit of Eq. (4.1) for both surfaces that yields the midpoint for each surface.

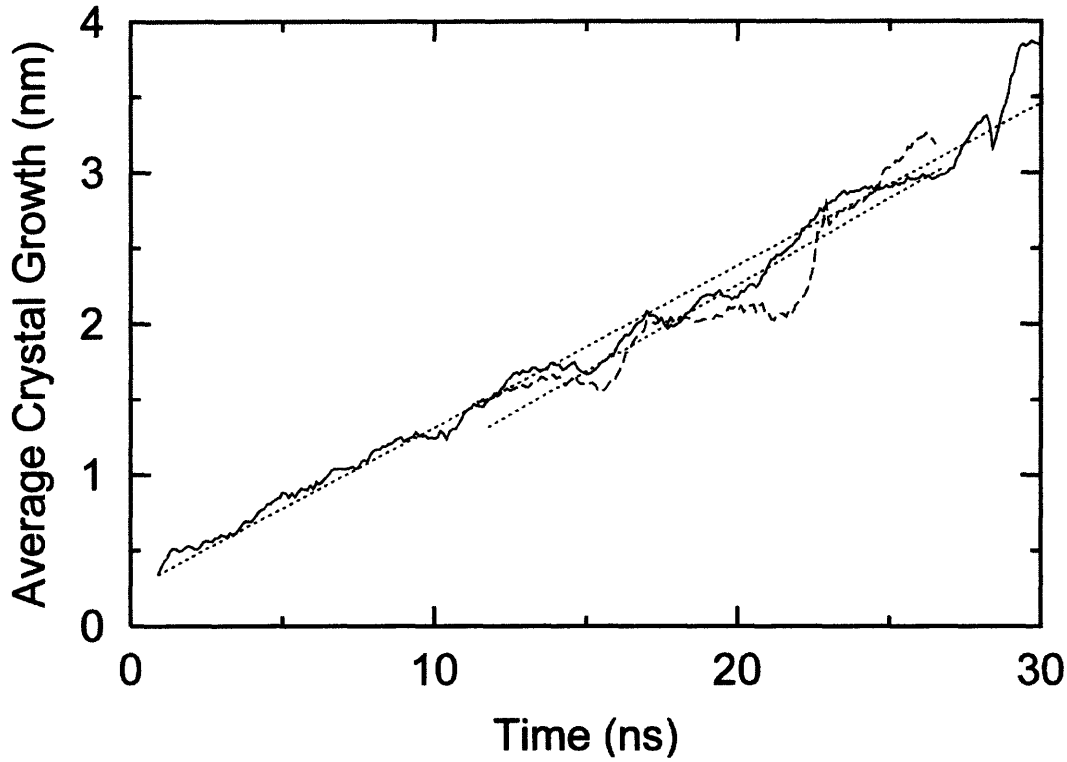

Figure 4.7 Average growth rate for n-eicosane isothermally crystallized at 285 K. The curves are the average displacement of the midpoints of each surface from the fixed crystal boundary: midpoints obtained from orientational order profile (solid line); midpoints obtained from packing order profile (dashed line); linear fits to data (dotted lines).

which had a very low molecular weight. The significance of molecular weight will be discussed in more detail in Chapters 6 and 7.

The analysis described above was repeated for several isothermal crystallization temperatures ranging from 225 to 300 K. From these, we obtained the temperature dependence of growth rate for both orientational order and density metrics. Figure 4.8 shows the data for translation of the orientational order inflection point at several temperatures, to illustrate the reliability of the growth rate estimates. Figure 4.9 shows the dependence of growth rate on temperature. Figure 4.9(a) shows results based on orientational order, while Fig. 4.9(b) shows results based on density. At each temperature, the error bar is indicative of the high and low estimate obtained from each of the two fronts. Interestingly, at the highest growth rates, near T_{max}, the discrepancy between growth rate at the two fronts is also highest, indicative of considerable dispersion in growth rates. Nevertheless, the average appears to be reliable. Above 295 K, crystal is forming and re-melting throughout the simulation, and a growth rate can no longer be calculated. Below 240 K, mobility of the molecules is too slow to obtain a growth rate in the simulation time scale.

4.4 Model fitting

Constants for the Ziabicki model were determined from the data shown in Fig. 4.9 by non-linear least squares fitting. The fitted curves are included in Fig. 4.9, and the calculated values of Ziabicki's parameters provided in Table 4.1. The average maximum

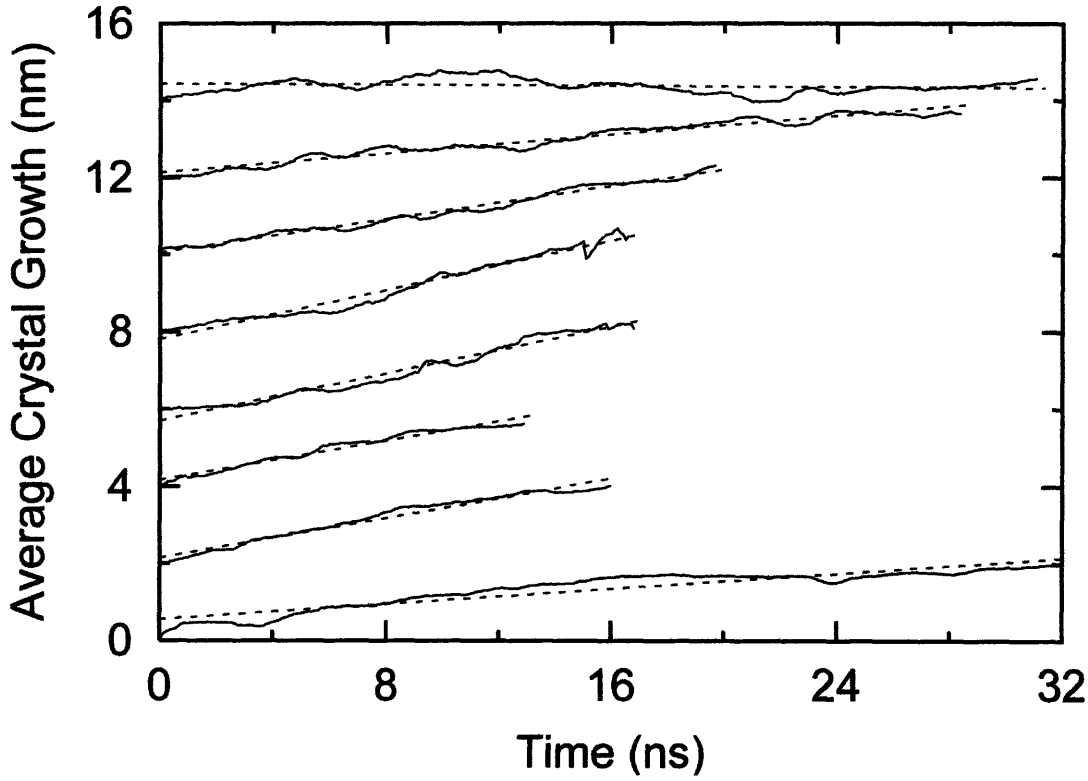

Figure 4.8 Average growth rate of crystals for isothermal crystallization at each of several temperatures. Data for each temperature is displaced vertically by 2 nm for clarity; from bottom of plot to top of plot, in order: 240K; 250K; 260K; 265K; 275K; 285K; 290K; 295K. Simulation data (solid lines); linear fits (dashed lines). The slope of the fitted lines gives the linear growth rate.

(a)

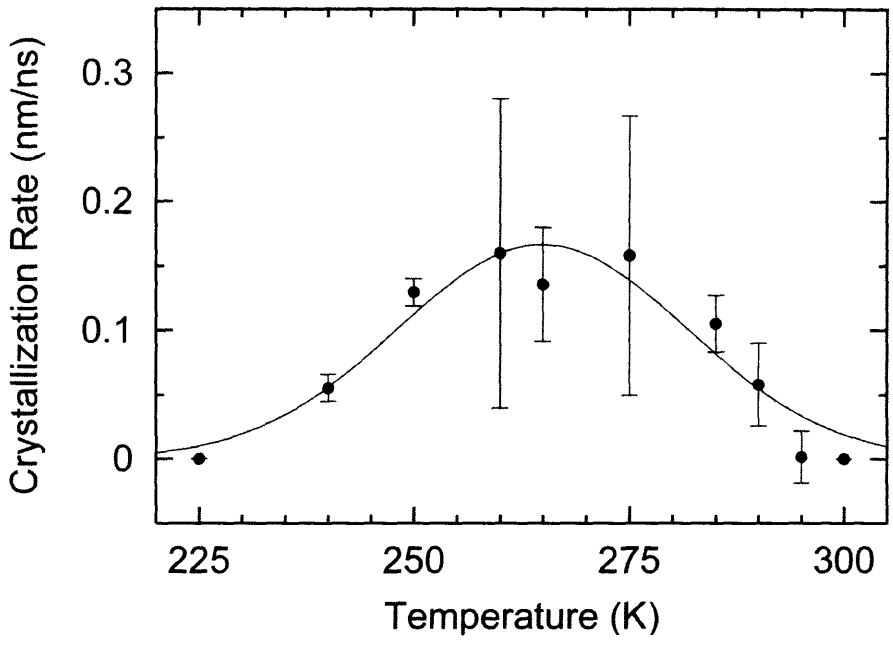

(b)

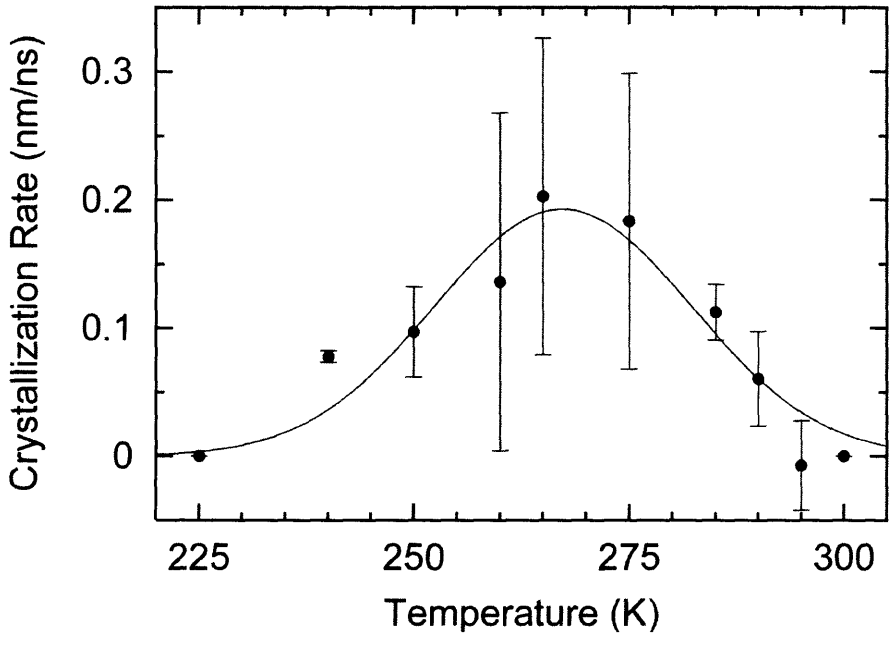

Figure 4.9 Temperature dependence of growth rates. Average growth rate (filled circles); individual growth rates obtained for each surface are indicated by error bars; Non-linear least squares fit to the Ziabicki model (solid line). (a) orientational order; (b) packing order.

Table 4.1 Calculated parameters for the Ziabicki model Eq.(2.1), for the fits presented in Fig 4.9, calculated by non-linear least squares regression.

Calculated Parameter	Order-based values	Density-based values
T_{max}	264.8 K	267.3 K
G_{max}	0.167 nm/ns	0.193 nm/ns
D	39.7 K	35.2 K

linear growth rate, for the two methods is 0.185 m/s, which occurs at 266 K. However, it should be emphasized that the resulting model, while similar in form to that for total crystallization rate, includes secondary nucleation only; it does not include primary nucleation, which would be present in empirical parameterizations of the model. As noted earlier, primary nucleation rates depend strongly on whether or not the mode of nucleation is homogeneous or heterogeneous. In one isothermal crystallization simulation at 250 K, we observed a spontaneous primary nucleation event in the middle of the cell, which led to creation of additional surfaces and an enhanced crystallization rate. Eder *et al.* point out that the occurrence of "diffuse crystallization" in the melt would be expected at high supercoolings, where the crystallization zone is large and the growth rate is small [Eder et al. 1990]. The temperature range for this event is also consistent with the range of increased primary nucleation found by Shimizu *et al.* [Shimizu and Yamamoto 2000]. Upon reproduction of the simulation at 250 K starting from another melt configuration, primary nucleation did not occur. (For the results presented in Fig. 4.9, only the latter set of data at 250K is reported.)

The maximum growth rates observed by simulation are considerably higher than those observed either for n-alkanes or for polyethylene. Recent experiments on primary nucleation rates for n-eicosane indicate that T_{max} occurs at 295 K, which is where we find the onset of appreciable secondary nucleation. This may explain why overall conversion rates appear continuous, such that Ziabicki's model may be applied to overall conversion at a temperature range higher than we predict. The majority of experimental studies for short n-alkanes are performed at fractions of a degree of undercooling, T-T_m, where growth rates are slow enough to be optically observable [Yoon et al. 1989]. It is difficult

to compare simulation results obtained on the scale of nanoseconds, with this large body of data obtained on the scale of seconds. For polyethylene, van Krevelen reported an estimated maximum crystallization rate of 3.0×10^{-5} m/s, estimated from the rate of change of a spherulite diameters observed by microscopy, occurring at a temperature near 300 K [van Krevelen 1978]. The recent experimental work by Ratajski *et al.* was only able to reach temperatures as low at 350 K, but did find rates on the order of 10^{-4} m/s [Ratajski and Janeschitz-Kriegl 1996]. This is significantly lower than the results we present for n-eicosane, but given that the diffusive barrier for polymers is orders of magnitude larger than that for eicosane, and that the free energy gain is larger because of the lack of a fold surface, these large differences are not unexpected. We also expect that since the diffusion is limiting for longer chains, while the free energy gain per CH_2 unit is very similar, T_{max} would be shifted to higher temperatures for the longer polyethylene chains.

4.5 Elementary Rate Analysis

Taking a closer look at Figs. 4.7 and 4.8, one observes both forward and backward motion of the inflection point of the growth front, implying that the growth mechanism may be comprised of two elemental processes: crystal surface ordering and crystal surface re-melting, which occur in rapid succession and for variable duration. As a first approximation, we separate these processes by estimating the first derivative of the inflection point movement, and classifying steps that had positive derivatives as surface ordering, and ones that had negative derivatives as re-melting. This approach makes the

implicit assumption that crystal ordering and re-melting are not occurring simultaneously in different regions of $[z-\sigma/2, z+\sigma/2]$; this assumption is valid when the x-y plane is small, such as ours (which can contain at most 6 extended chains). Then we integrated the derivatives to form cumulative functions of surface ordering (chain attachment) or re-melting (chain detachment), by the following criteria:

$$k_{ordering} = \frac{1}{t}\int_0^t \max\left(0, \frac{\partial \zeta}{\partial \tau}\right) d\tau \tag{4.2}$$

$$k_{re-melting} = \frac{1}{t}\int_0^t \min\left(0, \frac{\partial \zeta}{\partial \tau}\right) d\tau \tag{4.3}$$

where k_i is the linear rate of the process i, and ζ is the coordinate of the inflection point of the phase boundary. The results of this analysis are shown in Fig. 4.10, for isothermal crystallization at 285 K. The actual ordering rate appears to be more than twice the observed crystal growth rate, but is mitigated by competition with re-melting. Repeating this analysis over the entire range of temperatures for which crystallization was observed, we obtain Fig. 4.11, which shows the temperature dependence of the underlying ordering and re-melting processes. The method is approximate and quite noisy. However, the trend appears to be that the ordering rate increases at low temperatures, but levels off above T_{max}. Above T_{max}, the thermodynamic driving force for ordering obtains a limiting value. Meanwhile, the re-melting rate increases monotonically with temperature, governed by thermal energy.

This description of the crystallization of n-eicosane is consistent with a Sadler-type model for secondary nucleation in polymers, where the elementary steps of the

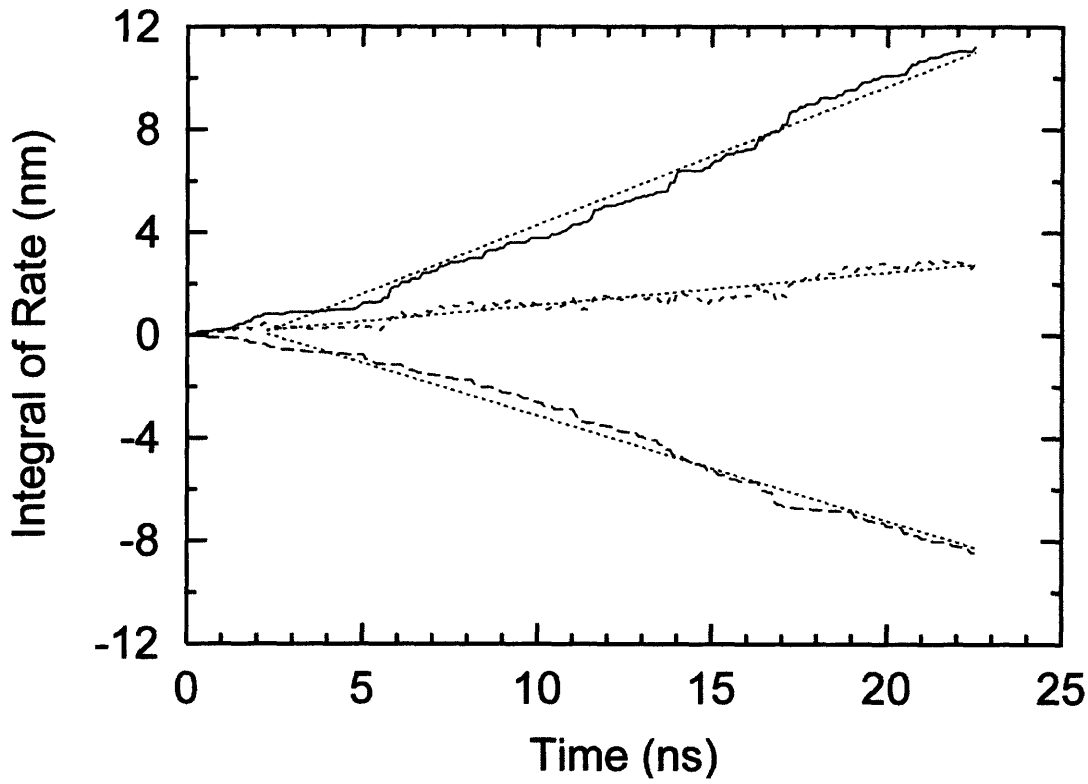

Figure 4.10 Integrals of the rates of the elementary processes of ordering (solid line) and re-melting (long dashed), computed by Eqs. (4.2) and (4.3), respectively. The observed rate (short dashed) is included for reference. The slopes of the linear fits (dotted lines) give the rate of each process.

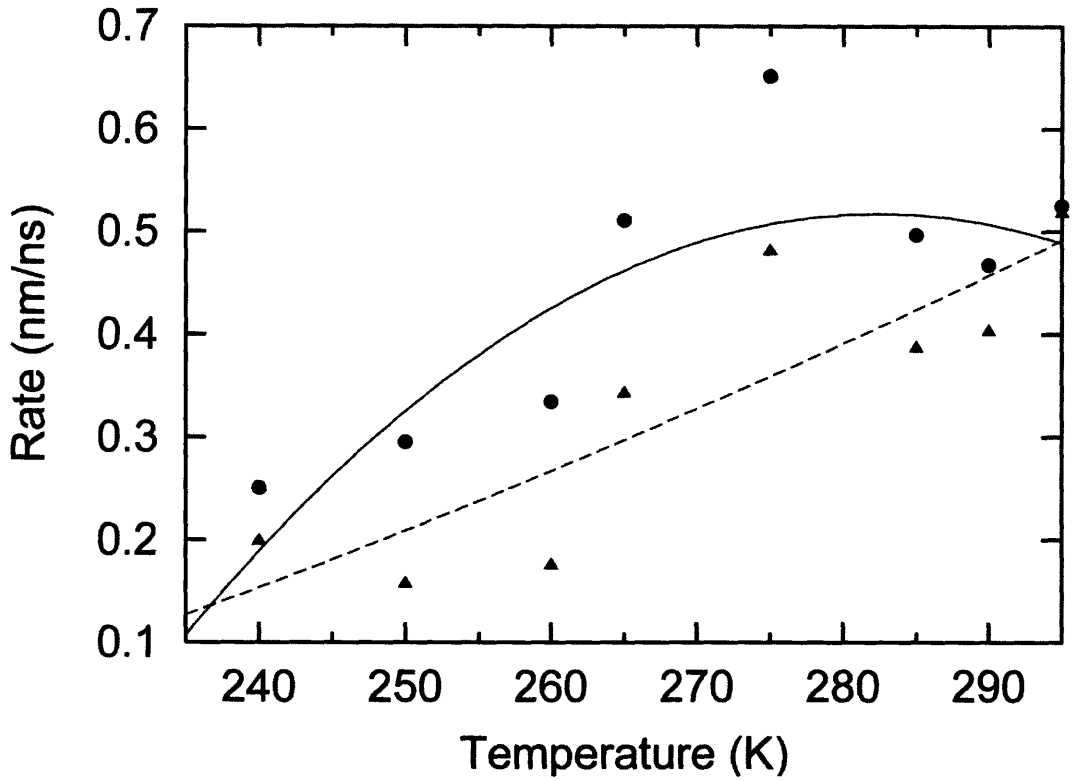

Figure 4.11 Temperature dependence of the average rate of elementary processes: ordering process (filled circles); re-melting process (filled triangles). Least squared fits of quadratic functions are provided as guides: ordering process (solid line); re-melting process (dashed line).

model include reversible detachment and attachment of short-chain sequences of at least 20 carbons. If re-melting is observed in the simple case of short chains, we anticipate that it may also be observed in the case of long chains, where the connectivity of a chain segment to the melt adds an addition degree of complexity. These results may also be interpreted as consistent with Strobl's model, at least for growth occurring only on the granular crystalline layer rather than the lamellar crystal. Strobl describes this layer a having a mesomorphic, hexagonal phase, which is also in accordance with our findings. Our decomposition of the growth into elementary attachment and detachment steps, with their own temperature dependence, lends itself nicely to a more course-grained kinetic Monte-Carlo algorithm that could model more long range growth, using input parameters with a molecular basis, once more reliable measurements are obtained.

Chapter 5

Molecular Weight Dependence of Rates

5.1 Simulation Description

We use the same non-equilibrium molecular dynamics (NEMD) technique as was used for C20, as discussed in Chapter 4. In this chapter, we consider systems of the longer alkanes $C_{50}H_{102}$ and $C_{100}H_{202}$, denoted C50 and C100, for the purpose of studying the molecular weight dependence of the crystal growth rate. In addition, we investigate the additional characteristics of the growth process, such as chain folding, that are observed in polyethylene crystallization, but that were not observed in our n-eicosane simulations.

It is worth noting that these simulations are considerably more time-consuming than those for C20, not only due to the larger simulation cells required in order to avoid artifacts of the finite simulation cell size, but also due to the longer simulation times required in order to capture the slower crystallization kinetics. Despite these limitations, molecular dynamics, through its resolution on the atomic length scale, provides information that cannot be obtained through any other source.

Again, the united atom interaction potential is used, in which polymer chains are represented by CH_2 and CH_3 beads that interact through bonded and nonbonded

interactions, along with the surface potential modeled for the united atom beads. The details of potential are found in Chapter 3.

The simulations consist of 42 C50 chains, or 40 C100 in a box of fixed x and y dimensions. In the z direction, the box dimension (the distance between the surfaces) is held at a constant stress of 1 atm. The initial box size for the C50 simulations is 25.9×65.0×39.3 Å, and the initial configuration was generated at a reduced density of 0.3 g/cm^3, as described in Chapter 3. The simulation cell was then equilibrated to bulk density using molecular dynamics at 400 K and 1 atm for 1 ns. The C100 simulations start from a simulation cell that is 52.0×80.0×31.3 Å, after being equilibrated for 1 ns at 500 K. After the equilibration phase, the systems were quenched below the melting point to begin the crystallization process. Identical C50 samples were quenched, resulting in crystallization data at 290, 300, 315, 330, 345 and 360 K. C100 samples were quenched, resulting in data at 350, 375 and 400 K. It is worth noting that the experimental melting point of C100 is 388 K [Small 1986], but crystallization at 400 K was attempted after successful crystallization was observed for 350 K and 375 K.

For our previous study of C20 and for the simulation of C50 here, the y dimension of the cell was readily chosen large enough to accommodate fully extended chains in the crystal phase, and fully extended chain crystallites were formed, in accord with experimental observations. Full chain extension during crystallization has also been observed for C102 from solution at small undercoolings [Ungar et al. 1985], but at the large undercoolings used here, the kinetics were expected to prevent the fully extended crystallization of C100 from occurring. Therefore, in the interest of shorter simulation

time, the y-dimension of our C100 simulation is only 8 nm, sufficient to allow for the case of once-folded chains.

We integrate the equations of motion using the velocity-Verlet integration described in Chapter 3, using a 5 fs time step. The simulation is conducted at constant temperature, constant length in x and y dimensions, and constant stress of 1 atm in the z dimension. Constant temperature and stress are maintained using velocity and position rescaling as described in Chapter 3, with thermal inertial time constant τ_T and volume inertial time constant τ_P of 3.3 ps and 5.0 x 10^3 ps, respectively.

Before discussion of these results, it should be reiterated that the late stage of crystallization and completion of ordering in each layer may be affected by the finite size of the simulation cells used. However, it is possible to conclude that these finite size effects exert less influence on the early stage of crystallization and initial ordering in each layer, and hence their affect on the observed growth rates will also not be as strong. As mentioned in the Results section, the surface nucleus is small and will not be affected by the periodic boundary. In addition, the development of the secondary nucleation event in the subsequent layer occurs prior to completion of ordering in the underlying layer, and thus should not be affected by finite size effects. Only the final stages of layer completion are expected to incur finite size effects.

5.2 Visual Assessment

Once the systems have been quenched below the melt temperature, the hallmarks of crystallization are almost immediately observable near the simulated surface, for both

C50 and C100. Although these two systems manifest similarities, there are also some differences that can be immediately seen visually. Figure 5.1(a) shows snapshots of the C50 system at times t=0, 30, 60 and 90 ns after quenching to 330 K. Figure 5.1(b) shows a similar set of snapshots for the C100 system at times t=0, 20, 40 and 60 ns after quenching to 375 K. In both cases, the crystallization begins at the x-y walls of the simulation cell, where the simulated crystal surfaces (not shown) promote the addition of new crystal layers. As shown in Fig. 5.1(a), the typical C50 simulation first forms clearly defined, well-ordered layers of fully extended chains at the x-y boundaries of the cell, layering which proceeds throughout the volume of the simulation cell. By 90 ns, the cell consists of 6 fully ordered crystalline layers. Figure 5.1(b), however, reveals a somewhat different picture for crystallization of C100. The crystallization process still proceeds through a sequence of layer ordering stages starting at the x-y boundaries of the cell, but the progression is much slower. By 60 ns, the crystallization has not yet completely filled the simulation cell, and defects persist within all layers, including those nearest the Steele surface, until the end of the simulation. Rather than fully extended chains as seen in C20 and C50 or once-folded chains as seen experimentally near T_m, in C100 at high undercoolings, only sections of chains are extended and packed.

The processes exemplified by Fig. 5.1 can be seen more clearly if viewed layer by layer. Figure 5.2(a) shows the three layers closest to one surface of the cell, at various times for C50. With this view, we can see that two processes are occurring: ordering and extension of chains within a layer, and the propagation of that order from one layer to the next. For example, between 30 and 60 ns, the average length of chain residing entirely in layer 1, not counting short segments less than 10 beads long which appear to be melt-like

(a)

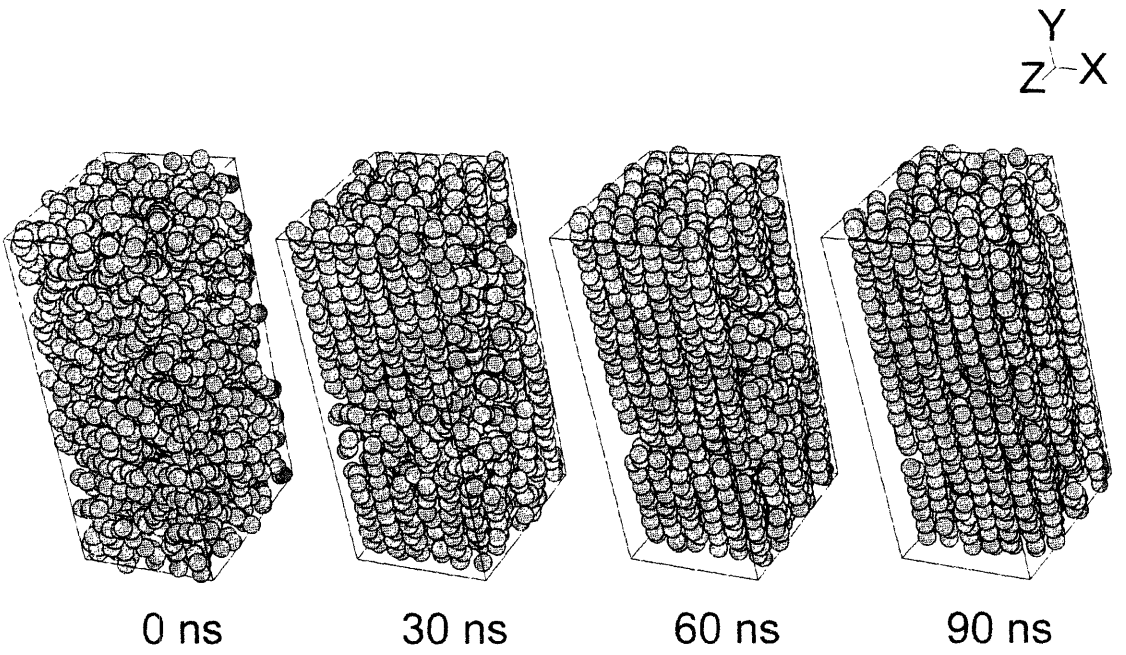

(b)

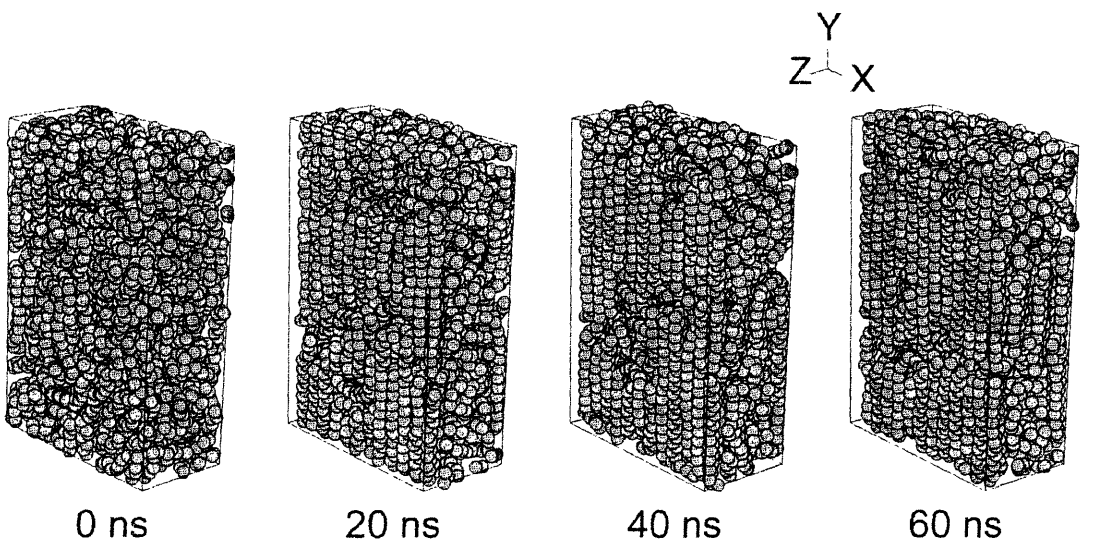

Figure 5.1 Simulation cells for C50 and C100 systems where simulated surfaces are located at the *x-y* walls; (a) Chain configurations for the 42 C50 chain system quenched to 330 K at times t= 0, 30, 60, and 90 ns. (b) Chain configurations for the 40 C100 chain system quenched to 375 K at times t= 0, 20, 40, and 60 ns.

(a)

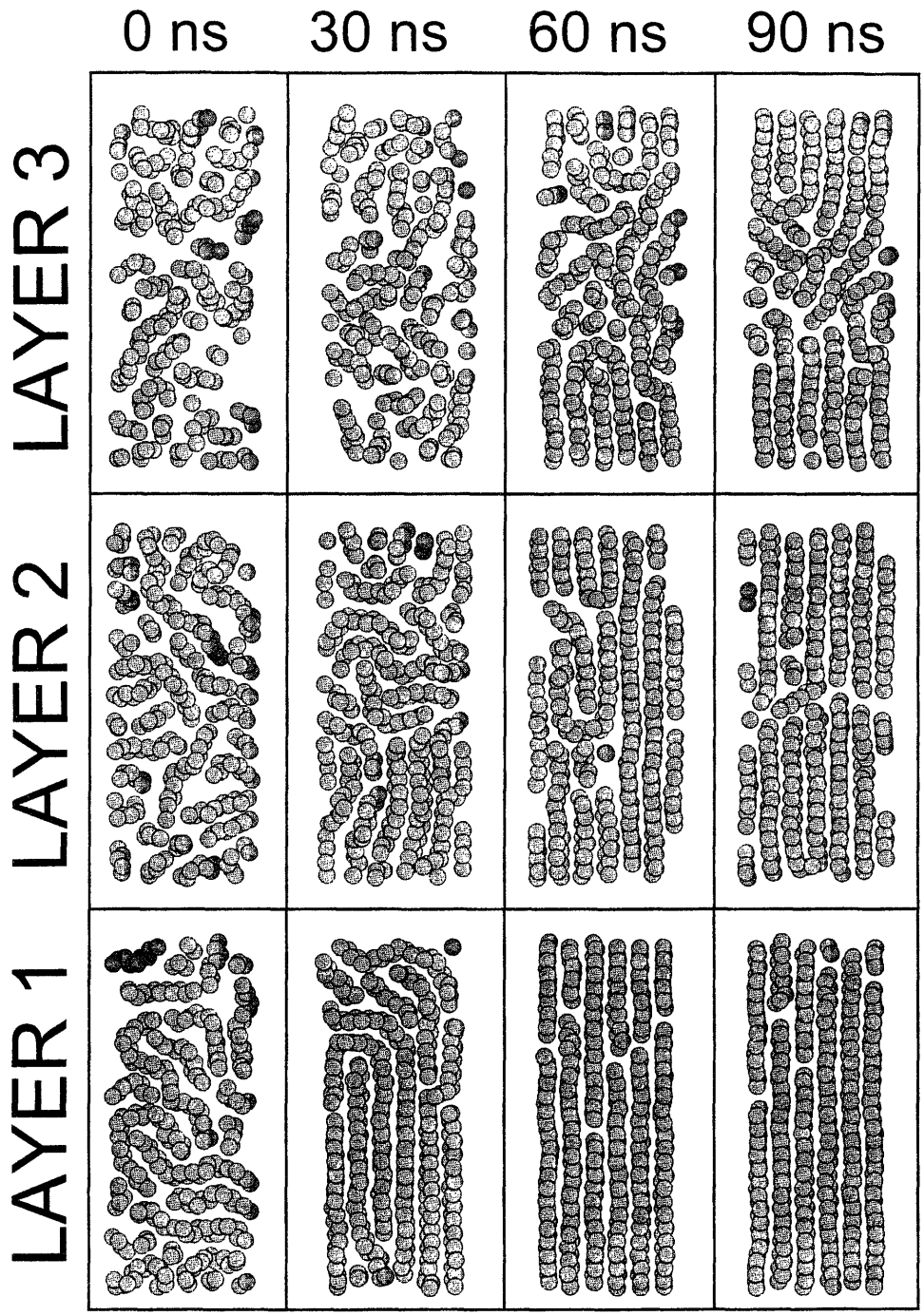

Figure 5.2(a) The three layers closest to $z = 0$ plane for 42 C50 chains after quench to 330 K at $t = 0$ ns.

(b)

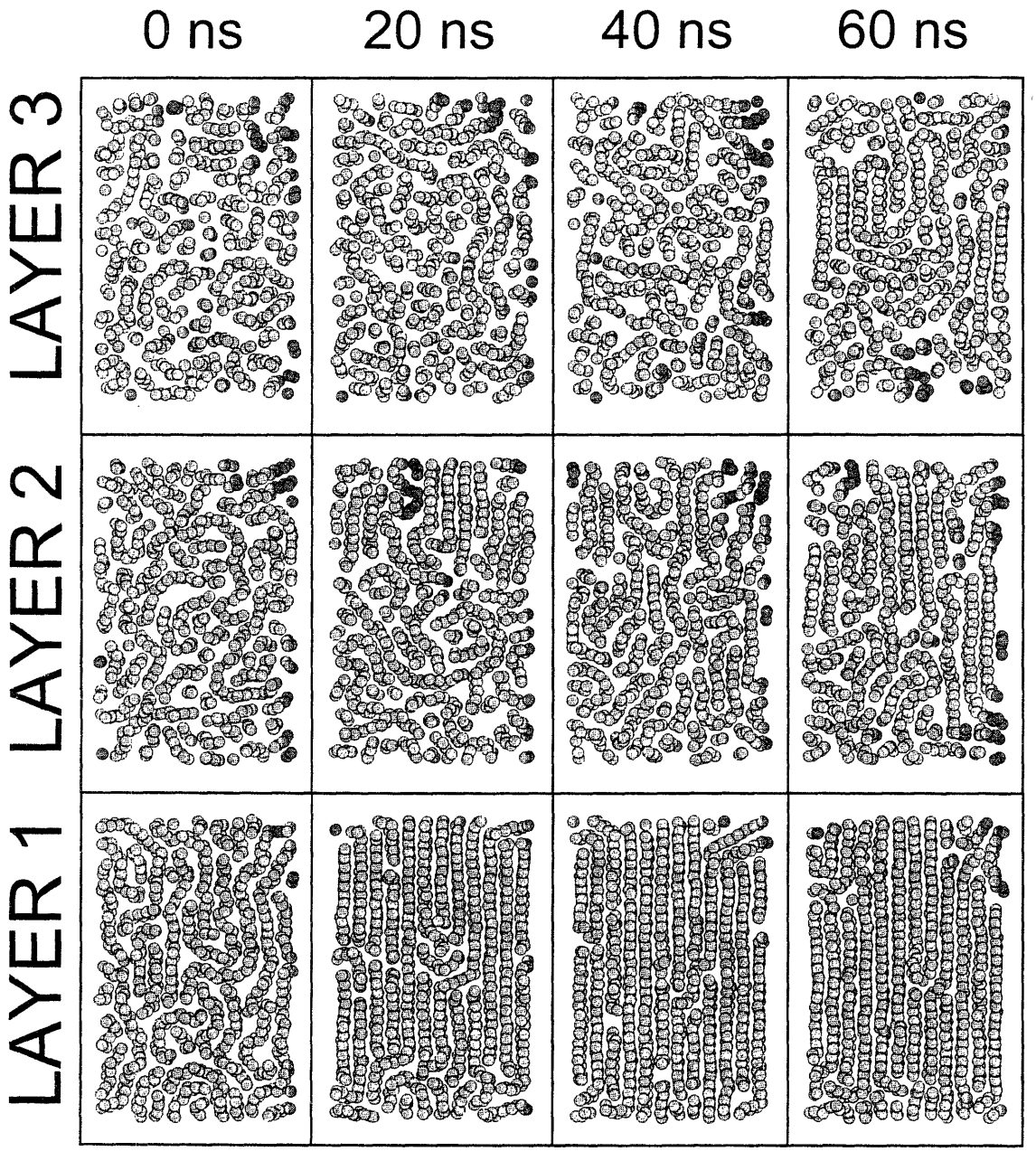

Figure 5.2(b) The three layers closest to the $z = 0$ plane for 40 C100 chains after quench to 375 K at t =0 ns.

loops, increases from approximately 20 to 50, through a process of drawing chains in from the melt. By 30 ns, one observes a band of partially extended, aligned, all-*trans* chain segments, approximately 20 CH_2 segments long and 6 chains wide (the entire width of the cell in the x dimension). In subsequent snapshots of the same layer, the chains become fully extended and the chain ends move into approximate registry through a process of chain sliding (longitudinal diffusion) within the layer. Simultaneously, in layer 2 at the next snapshot in time (60 ns), a similar band, 6 chains wide and 20 segments long overlays the ordered band in layer 1, and the process of perfection though chain sliding is repeated. A similar process appears to be occurring in layer 3 sometime between 60 and 90 ns. The ordering within a layer thus appears to be a stochastic process of drawing chains in from the melt, bringing them into crystallographic registry, and sliding them into different lattice positions to increase the stem length, over a period of 60 ns for each layer. *Gauche* states migrate away from the growing nucleus, until they either transform spontaneously into *trans* states or reach the chain end. Figure 5.2(b) shows a similar sequence of events for C100. Although slower than in the C50 case and incomplete within the 60 ns of simulation, small regions of order approximately 20 CH_2 segments long and 10 chains wide are nevertheless apparent in layer 1 in the 20 ns snapshot and proceed to lengthen within the layer in subsequent snapshots. In layer 2 at 60 ns, ordered regions approximately 20 CH_2's long and 3 chains wide are only just apparent. Surface nuclei form on the regions of the previous layer that are crystalline.

Some of the observations made regarding the mechanisms of ordering and propagation have implications for secondary nucleation theory for alkanes and polymers. Lauritzen and Hoffman assumed that the critical rate-limiting step was a stem segment

extending to a length matching the underlying lamellar thickness, and in turn parameterized the thermodynamics of this in terms of the surface energy of the lateral surfaces and fold surfaces associated with these steps. Estimates for the fold energy of a polymer lamella are often made by applying this assumption to measurements of spherulitic growth rates. We have not seen any evidence of this full-length extended stem nucleation; instead, we observe the initial formation of surface nuclei of stems of length 20. Similarly, Mandelkern's assumption of a monomolecular surface nucleus is also not supported by these simulations; instead, we observe a surface nucleus that involves several segments of different chains locking into surface registry. This different picture of growth has implications for the determination of surface energies from the thermodynamic constant C, discussed in Chapter 2.

We observe multiple chains adsorbing and desorbing on the crystal surface. When a group of chains adsorb onto the surface stochastically in the same area, a critical nucleus may be formed. Although the nature of this surface nucleus is difficult to recognize analytically, there are some comments we can make based on general observation. This nucleus does not involve chains extended to the length of the underlying surface. It typically consists of a group of chains that are 20-24 beads long and 4-5 chains across at T=330 K (C50) or T=375 K (C100), corresponding to the low temperature side of the growth rate curve. This is in close agreement with predictions by Wagner and Phillips [Wagner and Phillips 2001], who estimated that the critical nucleus size for polyethylene is 3-4 stems at T= 392 K, based on rate measurements for polyethylene and ethylene-octene copolymers. The stability of this critical nucleus depends on the extra surface the nucleus has created, as Hoffman and Mandelkern

postulated from classical nucleation theory, but it also depends on the number of defects within the nucleus, and the topology of the melt to which the monomer beads in the surface nucleus are connected. It is difficult to conclude whether the nucleation occurring on the surface is that of a mesomorphic or metastable phase, as Strobl and Keller have suggested, or whether the nucleus is temperature-dependent; qualitatively, we did not observe significant differences in the surface nucleus at the different crystallization temperatures. Nevertheless, it appears essential that the initial nucleus is shorter than the fully extended stem length in the final crystal and that it involves multiple chains. The united atom force field used here crystallizes in a hexagonal form, which exhibits the same symmetry as the proposed mobile rotator phase in polyethylene. Binsbergen's assertion that polymer crystal growth is stochastic, involving several addition and removal steps, may be applicable not only to the addition and removal that creates a critical nucleus, but the sliding movement of the chains that allow thickening after the critical nucleus is formed. Growth of a nucleus consisting of a group of chain segments involves reorganization of the initial nucleus.

The energy of the fold surface of the lamella is often assumed to be the energy of the "fold" surface of the surface nucleus, based on the fact that this is the surface through which chain connectivity is maintained. However, this surface of the surface nucleus does not compare well with the lamellar fold surface. As surface nucleation occurs, there does not appear to be any recognizable "folds". The energy of that surface can be better characterized as the energy associated with changing the torsional conformation of the chain from the crystalline all-*trans* state, to the Boltzmann-weighted torsional states of the melt. It seems that it is not until later that a lamellar fold surface fully develops, as

the lengths of the extended stems grow. In our C50 simulations the chains eventually extend fully, while in the C100 simulations, they are limited by impingement of the chains on their periodic image.

5.3 Order Assessment

We can estimate the distribution of partially extended chain segments, thereby identifying the distribution of the length of all-*trans* segments. We define a torsional state as a *trans* state if the torsional angle lies between $-\pi/3$ and $+\pi/3$, where the maximums in the *trans-gauche* barriers are. We use a convolution in time over a 1 ns box function to reduce fluctuations. Figure 5.3(a) shows the distribution of sequences of consecutive *trans* torsions along a chain during the course of the simulation of C50 at 330 K. Initially, the *trans* torsional states are distributed in segments of length ten CH_2's or shorter. With time, this distribution shifts towards a population around 22 CH_2's long, through accretion of approximately 3 beads every 4 nanoseconds. Remarkably, the shift in the distribution to fully extended chains 50 CH_2's long occurs in a single, large step, with very few all-*trans* segments of intermediate length. This indicates that the jump from chain segments of 20 to 50 is activated, so that there is not a gradual shift in the entire population of the stems as might be expected for a diffusion-like process, but rather individual stems or groups of stems that grow in size fast enough that we do not observe significant numbers of intermediate length stems over any appreciable time.

In contrast to the C50 case shown in Fig. 5.3(a), Fig. 5.3(b) suggests that the mechanism for the crystallization in C100 at 375 K is quite different. There remain a

(a)

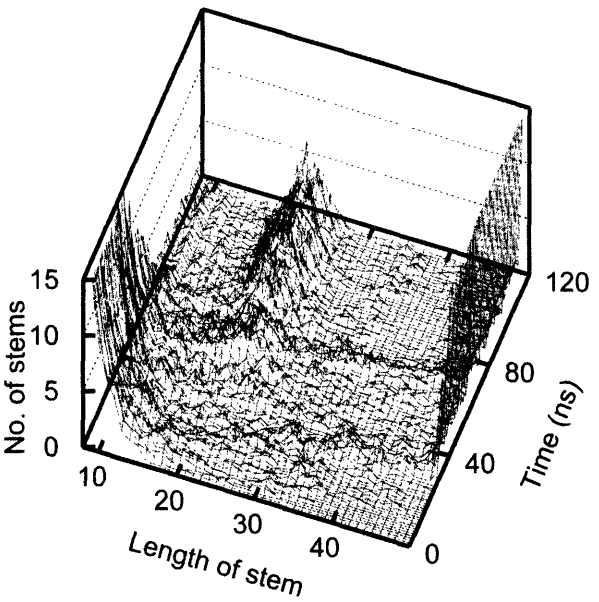

(b)

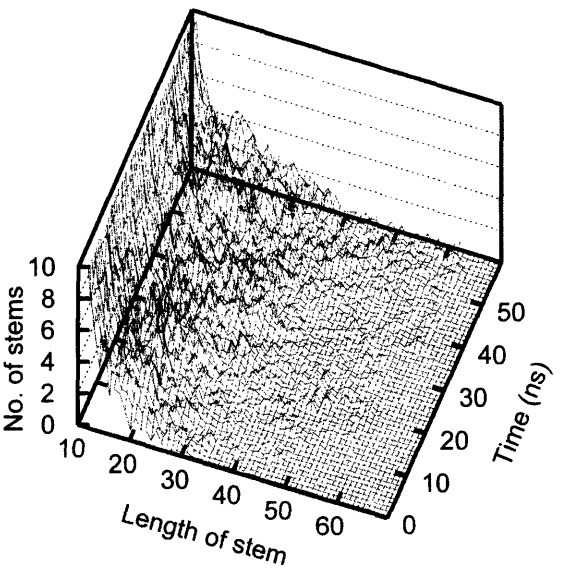

Figure 5.3 Distribution of all-*trans* stem segments over time for (a) 42 C50 chains quenched to 330 K at $t = 0$ ns; (b) 40 C100 chains quenched to 330 K at $t = 0$ ns.

large number of short stems during the course of the simulation, and the occurrence of longer stems is sparse and often short-lived. There is a small population of chains that have extended the full y-dimension of the simulation cell, around 60 beads long. However, at the end of the simulation, a peak for stems of length 20 does develop; the simulation is not long enough to observe the increase in population of stems of length 20, and the subsequent activated growth.

In order to quantify this series of events, we evaluate the order parameter $S(z,t)$ for each layer. This is accomplished by evaluating Eq. (3.23) at z=0.45 nm, 0.85 nm and 1.25 nm from the x-y boundary for layers 1, 2 and 3, respectively, with a convolution width μ of 0.4 nm. Figure 5.4(a) shows the results of this analysis over time for the first 3 layers for the C50 case. Full ordering of the first layer is accomplished in two stages, the first occurring between 0 and 15 ns, and the second between 25 and 35 ns. Ordering in the second layer begins concurrent with the second stage of layer 1. The large increase in $S(z,t)$, as it approaches its equilibrium crystalline value for a given layer, is in part due to the increased mobility of the chain ends, which are the last ones to be drawn into the layer, and in part because as $S(z,t)$ approaches one, the layer is almost filled, and the periodic boundaries enhance the stability of the ordered layer. Because of the small system size, fluctuations in $S(z,t)$ reflect the conformational changes in individual stems; in a larger simulation, we would expect these fluctuations to be damped, as is the case in the larger C100 simulations, shown in Fig. 5.4(b). One might expect the existence of a critical nucleus size for secondary nucleation to be reflected in a critical value for $S(z,t)$, but this is not obvious from Fig. 5.4. Such a critical value, if it existed, would be different for the C50 and C100 simulations in any case, since the x-y dimension differs

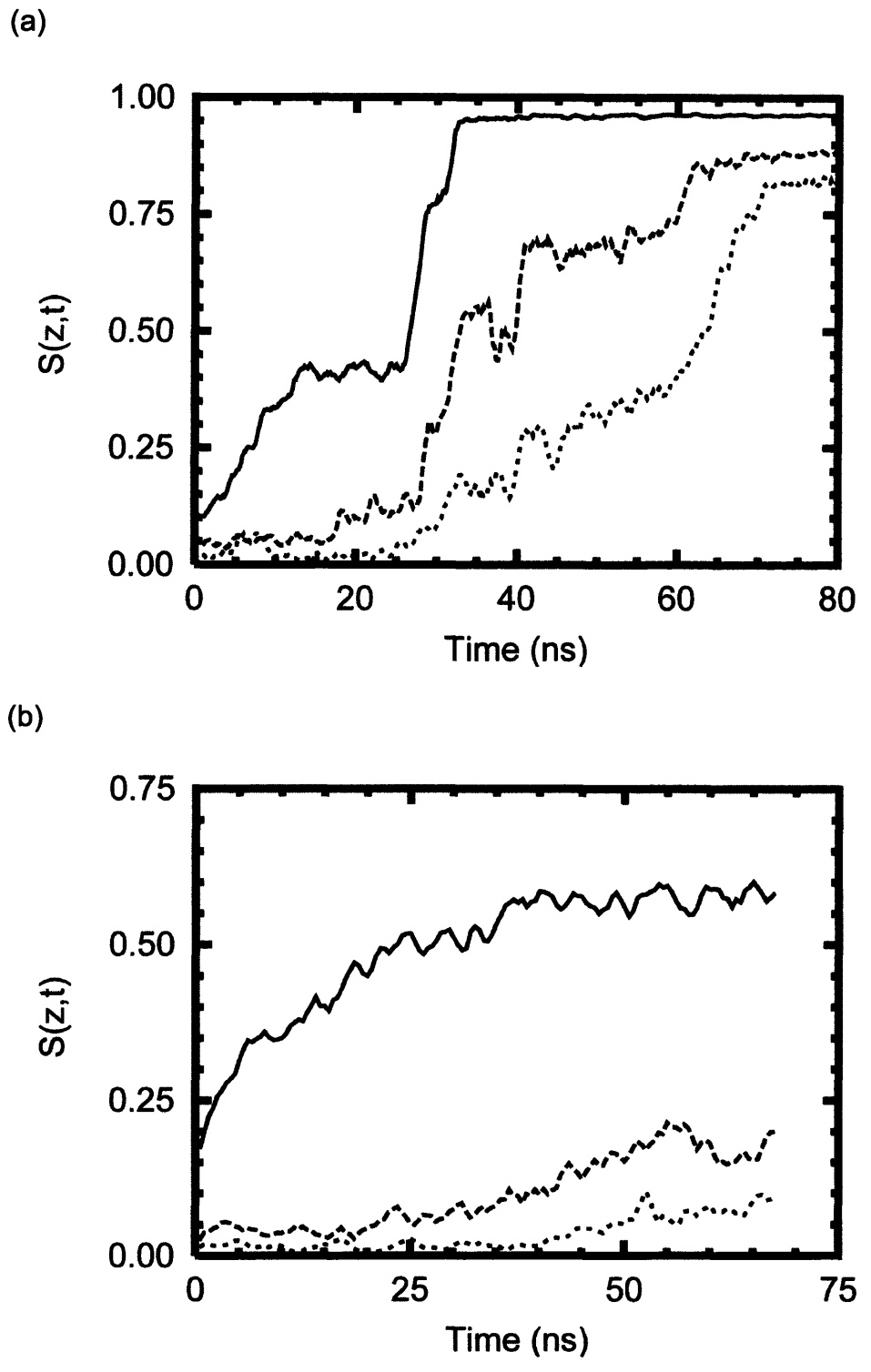

Figure 5.4 Local order parameter $S(z,t)$ as a function of the layer, over the convolution width of 0.40 nm, at the locations of the three layers closest to the simulated surface: z= 0.45 nm (Layer 1, solid line); z = 0.85 nm (Layer 2, dashed line); z = 1.25 nm (Layer 3, dotted line); for (a) 42 C50 chains quenched to 330 K at t = 0 ns; (b) 40 C100 chains quenched to 375 K at t = 0 ns.

for these two simulations. For the C100 case, we never observe a fully oriented layer due to the fact that the y-dimension is only 8 nm, sufficient only to accommodate stems up to length 60 CH_2's without a defect. Thus, the dynamics of stem growth only up to 1/2 the fully extended chain length can be studied in this case. For this reason, the C100 simulation only obtains a value for $S(z,t)$ of around 0.55, indicating that part of the layer does not crystallize. The behavior in this region is analogous to the impingement of two surface nuclei, which has been observed by Yamamoto [Yamamoto 2004].

The two different processes seen in Fig. 5.2, ordering within a layer, and propagation of that order to the next layer, can be quantified clearly in a three dimensional plot of the order parameter $S(z,t)$ versus distance and time. Figure 5.5(a) shows the profile of the orientation parameter $S(z,t)$, using a convolution width of 0.5 nm. It reveals the growth front for the C50 system after quench to 330 K, and its movement with time. Initially, the simulation cell begins from an amorphous state, and $S(z,t)$ is approximately zero throughout the cell. As the simulation progresses, order develops first near the z boundaries, as evidenced by the rise in $S(z,t)$ near z=0 and 3.35 nm, and then propagates towards the centerline of the cell. The growth front can be identified as the z-region through which $S(z,t)$ makes the transition from amorphous to crystal. Figure 5.5(b) shows the orientation profile $S(z,t)$ as a function of time, for the C100 system after quenching to 375 K. The movement of the orientation front is slow but steady. The asymptotic limit of $S(z)$ is near 0.90, as the layers always contain some amount of disorder as the stems impinge on themselves in the y-direction.

(a)

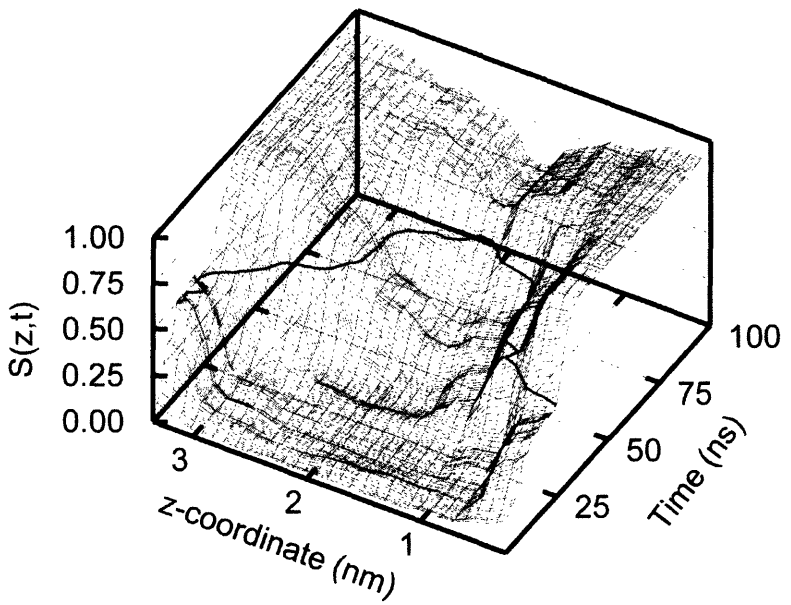

(b)

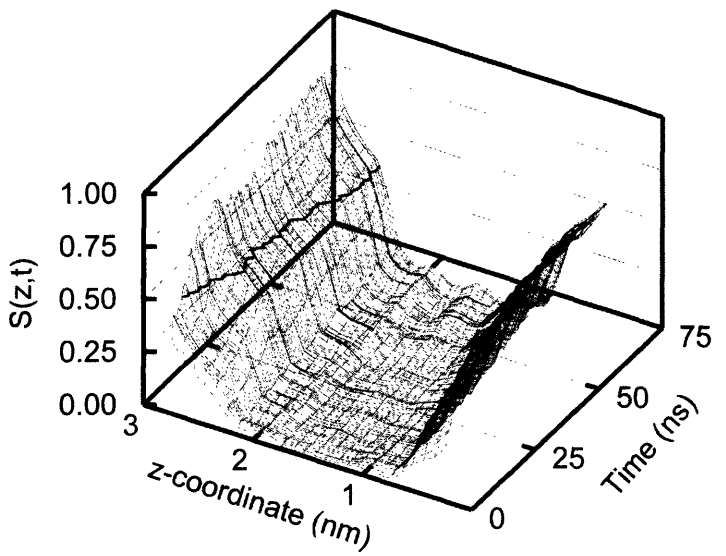

Figure 5.5 Progression of the orientational order $S(z,t)$ growth front for (a) 42 C50 chains quenched to 330 K at $t = 0$ ns, and (b) 40 C100 chains quenched to 375 K at $t = 0$ ns. The z-coordinate is the direction normal to the surface. The convolution width is 1.0 nm. In each case, the contour at which the order parameter is halfway between the crystal and melt values is highlighted.

5.4 Growth Front Description and Movement

The order profile can be fit by a hyperbolic tangent function, as described previously in Chapter 4, in Eq. (4.1). Since there are two surfaces in the simulation cell, there are two growth fronts moving towards each other. The entire z profile, including both growth fronts, can be modeled with two hyperbolic tangents. We give Eq. (4.1) again, as a reference:

$$S(z) = \tfrac{1}{2}\left[H_1 + H_2 - (H_1 - h)\tanh\left(\lambda_1\left(x - \xi_1\right)\right) + (H_2 - h)\tanh\left(\lambda_2\left(x - \xi_2\right)\right)\right] \qquad (5.1)$$

where H_i is the asymptotic value of the order parameter for the crystal growing at surface i, h is the asymptotic value of the order parameter for the amorphous region between the crystals, $1/\lambda_i$ is the interfacial width of phase boundary i, and ξ_i is the inflection point of phase boundary i. Fitting is done using a Levenberg-Marquardt nonlinear least squares algorithm. The movement of the inflection point ξ_i is approximately linear in time, in accord with experiments on spherulites. The growth rate is given by the average value of $d\xi_i/dt$.

Approximately 75% of the change in the order parameter between crystal and melt occurs in the z-region $[\xi - (1/\lambda), \xi + (1/\lambda)]$. The width of the interface should be that of a single layer if growth resembles Regime I or II in Hoffman's analysis. Regime III growth occurs over many layers, and should be reflected in a larger interfacial width. If a crystal grows a single layer at a time, then the interfacial width remains small. However, if there are multiple layers of surface nuclei with terraces and holes to be filled, it will take a larger value. Figure 5.6 shows the time-averaged value of interfacial width $1/\lambda$

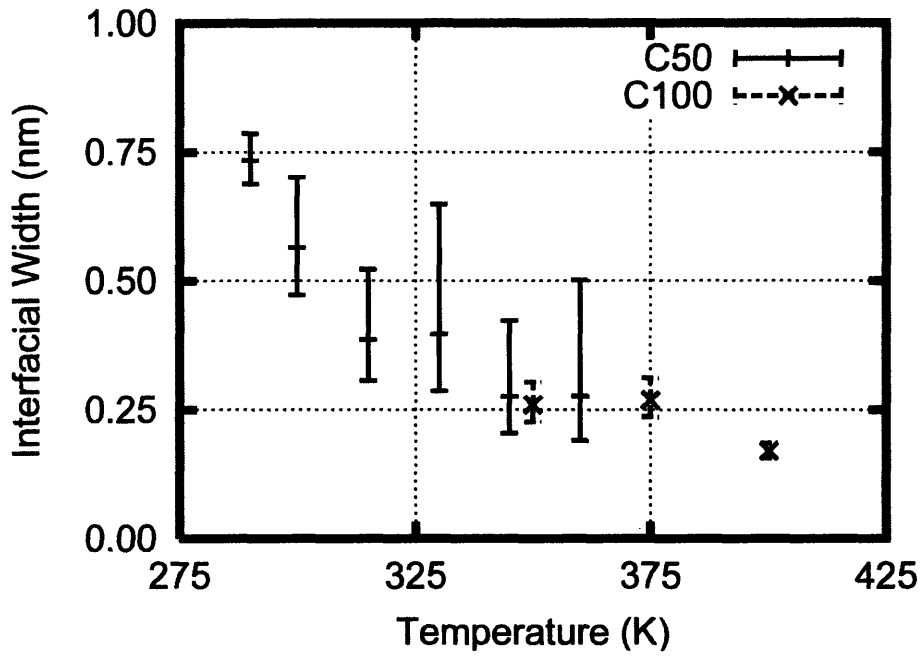

Figure 5.6 The average interfacial width of the growth front, as given by $1/\lambda_i$ in Eq. (5.1), as a function of temperature for the 42 C50 chain systems (+) and the 40 C100 systems (×); error bars show standard deviations.

versus temperature for both C50 and C100. Both sets of data follow the same trend, decreasing in interfacial width with increasing temperature. In addition, it is worth noting that the standard deviation from the average value, which is a measure of the variability of the surface roughness, shown by the error bars, is much less for C100 than for C50.

The interfacial width appears to be mainly a function of temperature, rather than undercooling, with interfacial width decreasing as temperature increases. The width of the interface does not appear to depend explicitly on molecular weight. However, because higher molecular weight polymers have higher melting temperatures and glass transition temperatures, the envelope in which they crystallize is shifted to higher temperatures. Therefore, our MD results suggest that higher molecular weight polymers would tend to have sharper interfaces. The decrease of the interfacial width with temperature reveals the gradual departure from "rough" or "normal" growth, where there are multiple layers of nucleation, to "layer" growth, where a single nucleation site occurs in a layer, and growth occurs mainly through addition on the terraces of that site. As temperature increases the interfacial width seems to level off around 0.25 nm, i.e. 75% of the change in the order parameter is occurring in a single layer. In the high temperature cases, it seems that the process of removal of chains that have locked into registry is energetically more likely, which leads to a more ordered growth front. This is similar to a transition from Hoffman's rough Regime III growth, to the more ordered Regime II. When C50 values are compared to C100, as in Fig. 5.6, the C100 runs seem to exhibit much less variability in the interfacial width, indicating that the connectivity constraints

play a large role in limiting stochastic nature of the growth front to a more stable number of layers.

Using this analysis we can also measure the growth rates for our simulations. We discard growth rates obtained at very short times, where the static nature of the Steele potential artificially accelerates the growth rate, and at very long time where impingement of the surfaces occurs; the data presented is only in the range where the inflection point ξ_i in Eq. (4.1) is further than the Lennard-Jones cutoff length from either of these singularities. The movement of the inflection points of the two growth fronts yields two measures for the linear growth rate normal to the surfaces, each one based on a linear fit to the front location vs. time. For C50, identical samples quenched to 285, 290, 300, 315, 330, 345 and 360 K provided data for the growth rate as a function of temperature, and the trend is apparent in Fig. 5.7(a), which reveals a maximum in the growth rate near 347 K. When we apply the same analysis to the C100 systems, we obtain the growth rates at each of the three temperatures we simulated, as shown in Fig. 5.7(b), with a maximum growth rate occurring near 395 K. The data shown in Fig. 5.7 is plotted with a corresponding line modeling Ziabicki's empirical form, given in Eq. (2.1). However, modeling of the data set for C20, C50, and C100 will be discussed in detail in Chapter 6.

(a)

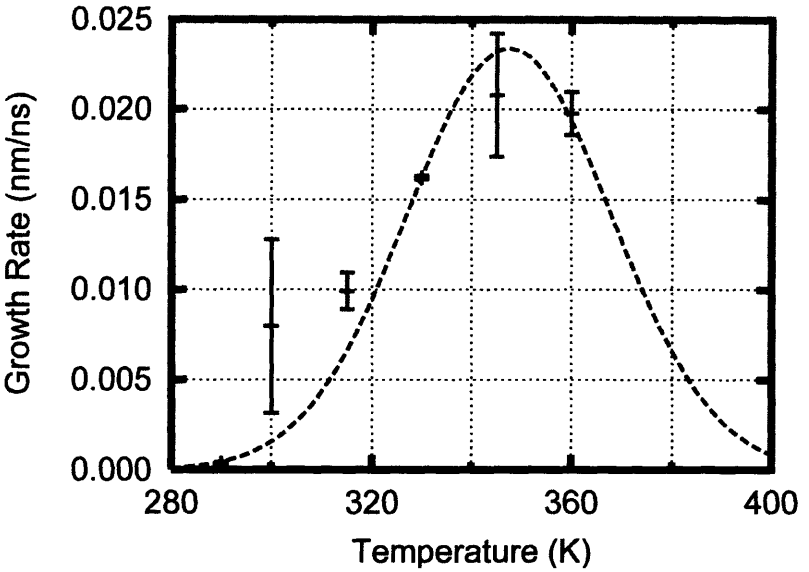

(b)

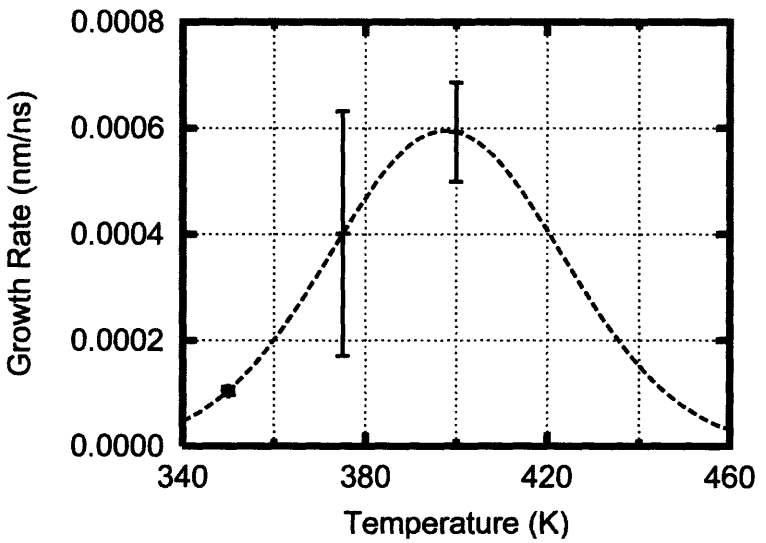

Figure. 5.7 Temperature dependence of growth rates, based on orientational order, calculated from the movement of ξ_i is Eq. (5.1). Average growth rate(+); individual growth rates obtained for each surface are indicated by error bars; nonlinear least squares fit to the Ziabicki model (solid line). (a) 42 C50 chain systems. (b) 40 C100 chain systems.

Chapter 6

A Simulation-based Model for Growth Rates in Alkanes

6.1 Derivation of Crystallization Rate Model

To recap our earlier report, our results for C20 were readily described by an empirical equation due to Ziabicki:

$$G = G_{\max} \exp\left[-4\log 2 \frac{(T - T_{\max})^2}{D^2} \right] \tag{6.1}$$

where G_{max} is the maximum growth rate, T_{max} is the temperature at which it occurs, and D is the half-width of the Gaussian curve [Ziabicki 1976]. However, despite its success in capturing the temperature dependence of the crystallization rate, it does not account for the effects of molecular weight or provide any connection to the underlying phenomena. To accomplish this, we develop the analytical form of the crystallization model from scratch, following the arguments described above in connection with combined theoretical/experimental models.

As a starting point, we note that most theoretical investigations [Hoffman and Weeks 1962; van Krevelen 1978] have started with the same basic equation, originally

suggested for nucleation by Turnbull and Fisher [Turnbull and Fisher 1949], whereby the energy barrier can be broken down into a thermodynamic part for the formation of a critical nucleus and a diffusive part for activated diffusion to the phase boundary. This allows for the parameterization of the growth rate in terms of energy barriers to nucleation and diffusive hopping:

$$G = G_0 \exp\left[-\frac{E_D}{RT}\right]\exp\left[-\frac{\Delta G_2^*}{RT}\right] \tag{6.2}$$

where G_0 is a pre-factor, E_D is the barrier to diffusive hopping, and ΔG_2^* is the free energy required to form a critical two-dimensional surface nucleus. Much of the prior work in this field has emphasized the second, thermodynamic term, which was formulated for a spherical drop by Gibbs [Gibbs 1948], and generalized by Turnbull and Fischer. The temperature dependence of this term is readily observed close to the melting point, where the process of crystallization is nucleation-limited. Mandelkern *et al.* observed this proportionality for polyethylene close to T_m [Mandelkern et al. 1968]. In this regime, the rate exhibits the following proportionality,

$$G \propto \exp\left[-K_g / T\Delta T\right] \tag{6.3}$$

where K_g is the surface nucleation constant reflecting the ratio of surface energy to bulk energy of a critical volume, and ΔT is (T_m-T), the undercooling below the equilibrium melting temperature. This constant K_g is a consequence of general nucleation theory and

is relatively independent of molecular weight, since the surface energies and free energy difference between the subcooled amorphous and crystal phase are a function of the chemical properties of the monomer unit only. This result has been theoretically derived for a general description of surface nucleation in polymers by Binsbergen [Binsbergen 1970], and has been applied to specific concepts of a surface nucleus by Hoffman and Weeks [Hoffman and Weeks 1962] and Mandelkern [Mandelkern 1964].

The diffusive term, on the other hand, has not been parameterized for alkanes; for polymers, it has been difficult to find a relation that applies over a large temperature range. Using Eq. (5.2), and the empirical data of Mandelkern *et al.* for E_D [Mandelkern et al. 1968], van Krevelen proposed a crystallization rate equation of the form:

$$G = G_0 \exp\left[-C_D \frac{T_m^{\,2}}{T(T_m - T_g)}\right] \exp\left[-\frac{C}{T}\left(\frac{T_m}{T_m - T}\right)\right] \tag{6.4}$$

where G_0 is 10^{12} nm/s, C_D is a dimensionless constant with a value of approximately 5 for most polymers, and C is a characteristic constant for every polymer, containing the ratio of the surface energy of a nucleus to the lattice energy gained by crystallization [van Krevelen 1978]. In this equation, the competing forces of secondary nucleation and thermal diffusion are described in terms of T_m, the thermodynamic melting point of a perfect crystal, and T_g, the glass transition temperature where diffusive motion is arrested, respectively. One feature of this model is that it allows for asymmetric curves for growth rate versus temperature, something that Ziabicki's empirical form does not capture. However, this equation has not been applied to both the diffusion-limited and thermodynamically-limited regions, because of the inability to parameterize the diffusive

term over the entire temperature range. In addition, while there has been some work to characterize the molecular weight dependence of G_0 [Van Antwerpen and van Krevelen 1972], we wish to provide here a more fundamental basis. Hoffman observed that E_D should be described by a Williams-Landel-Ferry (WLF) function for $T_g < T < T_g+100$ K, but invoked an Arrhenius relationship for temperatures close to the melting point [Hoffman and Weeks 1962].

The original concept for the diffusive energy barrier in Eq. (6.2) was the free energy of activation for short-range diffusion of atoms moving a fraction of the atomic distance to join the lattice [Turnbull and Fisher 1949]. In the limit that the free energy of crystallization is large and negative, the thermodynamic term becomes negligible, and the rate of crystallization is diffusion-limited. In classical reaction rate theory, a diffusion limited reaction is parameterized in terms of the self-diffusion constant D.

However, for polymers we can see that this rationale is problematic. In alkane and polymer crystallization is it not necessarily the translation of species towards the surface that yields the predominant energy barrier, but instead the conformational rearrangement (e.g. extension) of the chains at the surface. This concept is best captured in the relaxation time of the chain, in particular the relaxation time of the segment of the chain required for surface nucleation. Therefore, we parameterize the equation as a function of the relaxation time of the chain. In addition, this is the simplest quantity that captures diffusive mobility for which the temperature and molecular weight dependence is understood. There are two factors which influence mobility: the chemical properties of the monomer unit, and the number of monomer units in the chain. Previous models have not explicitly accounted for this fact, since for high molecular weight polymers, the

molecular weight dependence has proven difficult to quantify. The molecular weight dependence of the overall growth rate of entangled polymer chains is highly debated, with power law exponents ranging from -0.5 to -1.8, often depending on the temperature range [Umemoto et al. 2002]. For low molecular weights of the order of $M_w = 10^4$, the scatter in the experimental data has made it difficult to determine a relation [Hoffman et al. 1975]. However, for alkanes, by parameterizing in terms of the relaxation time, we can account for the temperature and molecular weight dependences. The mobility term is described by the term G_0, which is the diffusion-limited rate for a reference chain, τ_0, the relaxation time for the reference chain at some reference temperature, and τ, the relaxation time at the temperature and molecular weight of interest. The mobility is related to the reference chain by a ratio of relaxation times. The temperature and molecular weight dependence of the thermodynamic term is well described by the second exponential factor in Eq. (6.4). Combining the two contributions results in a growth rate given by

$$G(T,N) = G_0\left(\frac{\tau_0}{\tau(T,N)}\right)^n \exp\left[-\frac{C}{T}\left(\frac{T_m(N)}{T_m(N)-T}\right)\right] \tag{6.5}$$

where the exponent n is included to account for uncertainty regarding the dependence of crystallization rate on relaxation time.

The relevant relation for the relaxation time near a crystallizing surface is not clear from the literature. In particular, the debate centers on the behavior of the amorphous material near the crystal surface. It is generally agreed upon that diffusion

near a surface is more complex than bulk diffusion [Degennes 1981]; however the way the surface affects dynamics is still a matter of debate. Some researchers argue that the surface diffusion rates for short chains near a surface can be described by Rouse dynamics, where the relaxation time should have a power law dependence of 2 in the molecular weight [Semenov and Joanny 1995]. However, there is some indication that relaxation times of polymer chains near surfaces should have a power law dependence of 3 in molecular weight, indicating that chains with a 2D conformation behave more like reptating chains than Rouse chains [Sukhishvili et al. 2000].

Furthermore, a crystallizing surface is not the same as a static surface, since it is constantly converting amorphous material to crystal, and thus moving the surface forward in accord with the chain conformation rather than requiring the amorphous chains to conform to the (usually flat) shape of the surface. By this argument, the amorphous material near the surface still diffuses as a bulk where, for chains under the entanglement length (approximately 150 beads), Rouse dynamics are expected. Rather than committing to either assumption, we analyze our NEMD data here according to both the Rouse and reptation models for relaxation time.

According to Rouse theory, the longest relaxation time of a polymer chain is given by:

$$\tau_R = \frac{N^2 b^2 \zeta_0}{3\pi^2 kT} \tag{6.6}$$

where N is the degree of polymerization, b is the monomer diameter, T is temperature and ζ_0 is the monomeric friction coefficient. The Rouse formulation applies to short chains

in an unentangled melt. Reptation dynamics, which are observed in entangled systems, have a relaxation time given by the following,

$$\tau_D = \frac{N^3 b^4 \zeta_0}{\pi^2 kTa^2} \tag{6.7}$$

where a is a primitive segment length, defined as the distance between entanglements. In both Rouse and reptation dynamics, the relaxation time can be captured by the following general relation,

$$\tau(T,N) = \frac{C_\tau N^m \zeta_0}{T} \tag{6.8}$$

where C_τ is the constant containing the geometric and physical factors, and m is the molecular weight dependence, which is 2 for Rouse dynamics and 3 for reptation dynamics.

In a melt, ζ_0 represents the force per unit velocity required to move a monomeric unit through a sea of similar polymer chains, and thus is itself dependent on both temperature and molecular weight of the polymer [Ferry 1970]. The monomeric frictional force is closely related to the free volume associated with a monomer unit in the melt, and therefore exhibits a temperature dependence described by the Williams-Landel-Ferry (WLF) equation:

$$\ln\left(\frac{\zeta_0}{\zeta_{0g}}\right) = -\frac{2.303c_1(T-T_g)}{c_2+(T-T_g)} \tag{6.9}$$

where the WLF constants c_1 and c_2 are 17.44 and 51.66 K, respectively [Williams et al. 1955]. The monomeric friction coefficient at the glass transition temperature is ζ_{0g}, which has negligible dependence on molecular weight. The free volume at the glass transition temperature is considered a universal parameter, because it represents an iso-free-volume state; similarly ζ_{0g} should be the same for any polymer at its glass transition point [Ferry 1970].

By inserting Eq. (6.9) into Eq. (6.8) and taking a ratio of relaxation times as in Eq. (6.5), we find that the ratio of relaxation times takes the following form,

$$\frac{\tau_0}{\tau(T,N)} = \left(\frac{N_0}{N}\right)^m \exp\left[\frac{2.303c_1(T-T_g)}{c_2+(T-T_g)}\right] \tag{6.10}$$

where τ_0 is the relaxation time of a reference chain of a certain molecular weight at the glass transition temperature. The ratio of temperatures from Eq. (6.8) has been dropped, as is done in WLF theory, because it is a lower-order dependence and contributes negligibly to the temperature dependence of relaxation time. Inserting Eq. (6.10) into Eq. (6.5), we obtain the following final equation for the linear growth rate:

$$G(T,N) = G_0\left(\frac{N_0}{N}\right)^{mn} \exp\frac{2.303nc_1(T - T_g(N))}{c_2 + (T - T_g(N))}\exp\left[-\frac{C}{T}\left(\frac{T_m(N)}{T_m(N) - T}\right)\right] \qquad (6.11)$$

This results in a diffusive term that has a WLF dependence as Hoffman postulated, although now adjusted by n, and by tracing the WLF dependence to the relaxation time, also yields a molecular weight dependence. In addition to the explicit temperature dependence given by Eq. (6.11), the molecular weight also enters the equation implicitly through the glass transition temperature and through the melting temperature. Although the Fox-Flory equation is usually used to relate the glass transition and molecular weight, it does not hold for low molecular weights. Therefore, we use an alternative equation presented by Fox and Loshaek [Fox and Loshaek 1955], which does not present singularities at low molecular weights. Although there is debate regarding the value of the glass transition temperature for polyethylene[Davis and Eby 1973], best estimates for the glass transition temperature of alkanes, based on kinematic viscosities, suggest that this equation fits well[Miller 1968]. This relation can be described by:

$$\frac{1}{T_g(N)} = \frac{1}{T_g^{\infty}} + \frac{C_g}{\left(T_g^{\infty}\right)^2}\frac{1}{N} \qquad (6.12)$$

where T_g^{∞} is the asymptotic value of T_g at infinite molecular weight, and C_g is a constant. Data on molecular weight dependence of the melting temperature has been tabulated [Small 1986] and is found to fit to the same form:

$$\frac{1}{T_m(N)} = \frac{1}{T_m^\infty} + \frac{C_m}{\left(T_m^\infty\right)^2}\frac{1}{N} \tag{6.13}$$

where T_m^∞ is the asymptotic value of T_m at infinite molecular weight and C_m is a constant. The constants C_g and C_m are consequences of the chemical properties of the monomer. Molecular simulation can be used to determine these constants through a series of simulations. Methodology for these simulations has been described elsewhere [Meyer and Muller-Plathe 2002], as well as in Chapter 4. However, due to the large number of simulations that would be required to model the dependency, in this work we have treated them as fitting parameters in the solving of the rate equation, which results in three fitting parameters for Eq. (6.11), G_0, C, and n, and the four parameters that characterize the molecular weight dependence of the melting and glass transition temperatures, from Eqs. (6.12) and (6.13).

6.2 Parameterization of Model from Simulation Data

In order to parameterize the crystallization rate model presented above, a total of 7 unknown parameters need to be determined. There are 3 parameters in Eq. (6.11), related to the rate processes, G_0, C, and n. The parameter m is assigned the value of 2 or 3 depending on whether Rouse dynamics or reptation dynamics are assumed. There are also 4 parameters in Eqs. (6.12) and (6.13) that capture the molecular weight dependence of the phase transition temperatures: T_g^∞, C_g, T_m^∞ and C_m. In addition, we take C20 as the reference, which gives G_0 the interpretation of the value for the diffusion-limited rate pre-

factor for C20 at its T_g, which is expected to be a small value. We performed the seven parameter fit to Eq. (6.11) with Eqs. (6.12) and (6.13) for T_m and T_g, respectively, using a Levenberg-Marquardt nonlinear least squares algorithm. The resulting parameters and their standard deviations are given in Table 6.1 for both the Rouse and the reptation assumptions, and the best fit curves are plotted in Fig. 6.1. Because G_0 can change orders of magnitude during the fitting process, it is fitted as an exponential, and the standard deviation presented is the standard deviation of the exponent. Data near the maximum crystallization rate are better described by the curve, partly due to the lower statistical error associated with the determination of these values by molecular dynamics. When compared to the Rouse dynamics case, the exponential factor m=3 in the case of reptation dynamics is counteracted by increased values of C and n, and a widening of the envelope in which crystallization takes place, which can be seen by looking at the T_g and T_m values given by each model in Table 6.2.

Error analysis was conducted on the fits for the Rouse and reptation models to determine if the difference in the fits is statistically significant. The individual residual errors of the fit were normalized by the measurement error at each data point. Then a paired Student's t-test was conducted on the sample of 17 normalized errors using each model. The resulting probability of the null hypothesis is 0.108, indicating that the difference between the two models is not statistically significant.

The two models based on Rouse dynamics and reptation dynamics were statistically equivalent fits to the data. However, we can make some logical conclusions based on the values of the fitting parameters for the two models. Particularly noteworthy is the value of C in the reptation case, which is much larger than what is typically

Table 6.1
Calculated parameters for the model given by Eqs. (6.11), (6.12), and (6.13), assuming Rouse dynamics or reptation dynamics, for the fits in Fig. 6.1.

Parameter	Rouse dynamics		Reptation dynamics	
	Value	St. Dev.	Value	St. Dev.
$ln(G_0\ [m/s])$	-37.9	16.1	-41.3	15.5
$C\ [K]$	439	197	855	217
n	1.49	0.44	1.79	0.43
$T_m^{\infty}[K]$	500	11	535	8
$T_g^{\infty}[K]$	346	36	302	43
$C_m\ [CH_2 \bullet K]$	4.78e3	398	5.46e3	468
$C_g[CH_2 \bullet K]$	1.24e4	1224	8.70e3	1840

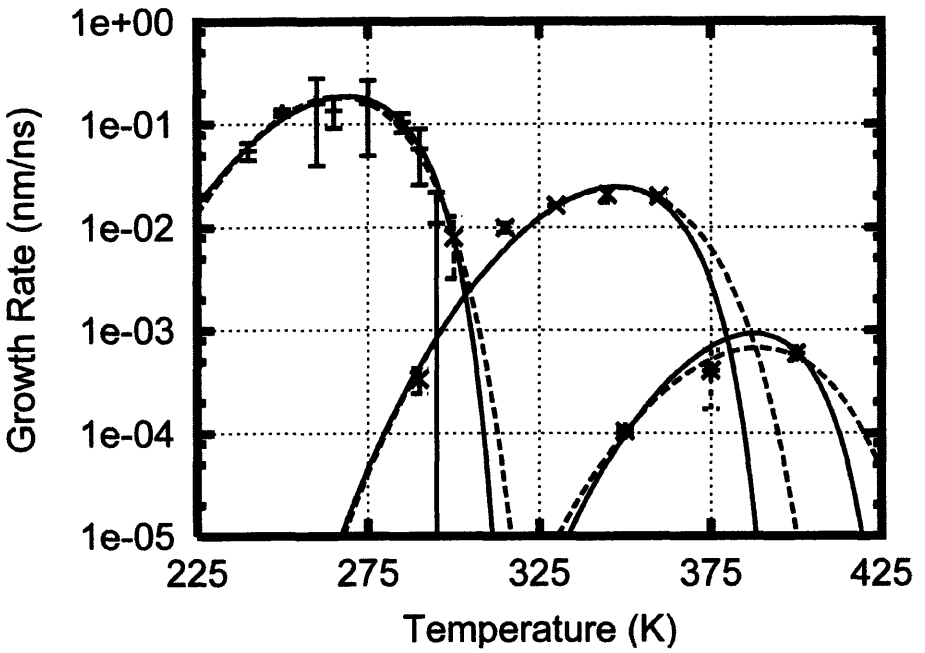

Figure 6.1 Fit of the model equation, Eq. (6.11), to the growth rate data for each molecular weight, assuming Rouse dynamics (solid lines) and reptation dynamics (dashed lines); fits are for the growth rate data shown: the 102 C20 chain systems (+), the 42 C50 chain systems (×), and the 40 C100 chain systems(∗).

Table 6.2
Values of the glass transition and melting temperatures, given by Eqs. (6.12) and (6.13), for the model fits shown in Fig. 6.1, for both the Rouse dynamics assumption and the reptation dynamics assumption.

Length	Rouse		Reptation	
	T_g	T_m	T_g	T_m
20	124 K	338 K	124 K	354 K
50	201 K	420 K	192 K	444 K
100	254 K	457 K	235 K	485 K

observed in nucleation-limited experiments. Furthermore, the occurrence of reptation dynamics for chains shorter than the entanglement molecular weight has not been observed, even for dynamics near a surface. In addition, the predictions for the melt temperature in the Rouse-based model, given in Table 6.2 are closer to the value we observed in the C20 case, which is above the experimentally observed values. These would suggest that the Rouse-based model predicts parameters closer to those experimentally observed. The Rouse-based model predicts a melt temperature of 339 K for C20, which is slightly lower than the value of 345 K that we previously determined in independent melting simulations, discussed in Chapter 4. We expect the temperature at which crystallization takes place upon cooling, determined using Eq. (6.11), to be slightly lower than the temperature at which melting takes place upon heating, determined by MD simulation as described in Chapter 4. In both cases, a metastable state is likely before the phase change occurs; for crystallization, the observed temperature for phase transition may be depressed, while for melting it may be elevated. The experimental melt temperature value for C20 is 310 K. We previously acknowledged that this force field overpredicts the melting temperature of n-eicosane. It also overpredicts the melting temperatures of C50 and C100 relative to the experimental values of 365 K and 388 K, respectively. Glass transition temperatures are more difficult to obtain, but comparison to recent simulation results with a similar potential suggest a T_g of 280 K +/- 32 K for a C768 chain [Capaldi et al. 2004]. If the molecular weight dependence of our model is extrapolated to C768 using Eq. (6.12), it yields a T_g of 330 K.

The discrepancy in the simulated melting and glass transition temperatures from experimental data is most likely a consequence of the fact that the forcefields are not

capable of duplicating all facets of the chain behavior. As was mentioned in Chapter 2, the forcefield used was based on reproduction of P-V-T data for alkane liquids. The ability to duplicate behavior in multiple phases is still a challenge for the researchers who create forcefields. However, the forcefield seems to systematically overpredict the glass transition temperatures and melt temperature for all chain lengths, which suggests that there may be a systematic issue with the strength of the interactions, which could be resolved with a simple scaling. However, it is possible that this will impact other, more important equilibrium and dynamic properties of the alkane melts, which have been parameterized correctly.

Regarding our processing model for crystallization rates, the model seems to capture the behavior well. It would be more correct to calculate the phase transition parameters from a series of equilibrium Monte Carlo simulations that could yield the molecular weight dependence of the phase transitions; both melting points [Meyer and Muller-Plathe 2002] and glass transition points [Capaldi et al. 2004] have been estimated using molecular dynamics simulations. However, a great number of simulations would be required to capture the molecular weight dependence effectively.

Other attempts were made to fit an equation to the experimental data. From models of diffusion-limited reactions, the parameterization of rates can be done from self-diffusion coefficients. We attempted this type of modeling but found the molecular weight dependence could not be captured with by the diffusion coefficient. This perhaps is because of the unique nature of polymer crystallization, where the barrier to crystallization is not the diffusion coefficient, but the time required to yield extension of chains and locking into crystallographic registry. In addition, polymer models by

Hoffman [Lauritzen and Hoffman 1973; Armistead et al. 1992] and others, were considered, but were again unable to capture the molecular weight dependence, since they are not designed for use for chains shorter than the entanglement molecular weight.

6.3 Implications for Polymer Growth Rate Models

Based on this model for alkane crystallization, we are able to draw some conclusions regarding the basis for a polymer crystallization model as well. The models available in the literature are capable of fitting the temperature dependence well, for a particular sample. We have fit the equations of van Krevelen, Strobl, and Umemoto to our C20, C50, and C100 data independently, and found that they too can capture the temperature dependence. Umemoto's equations require a temperature at which the maximum rate is observed, as well as a maximum rate, which we cannot generate from theory. Figures 6.2(a) and (b) show a comparison of our Rouse-based model to the best fit models of van Krevelen and Strobl, using all the data at all three molecular weights. Neither model accounts for an explicit molecular weight dependence, but there is an implicit dependence in the glass transition temperature and the melt temperature. While data at each molecular weight can be fit independently, Fig. 6.2 shows that the neither of these models can fit the entire range of data. There needs to be specific accounting for the molecular weight dependence. The Rouse-based alkane model, however, predicts reasonable trends in the crystal growth rate as a function of molecular weight and temperature; this is shown in Fig. 6.3.

(a)

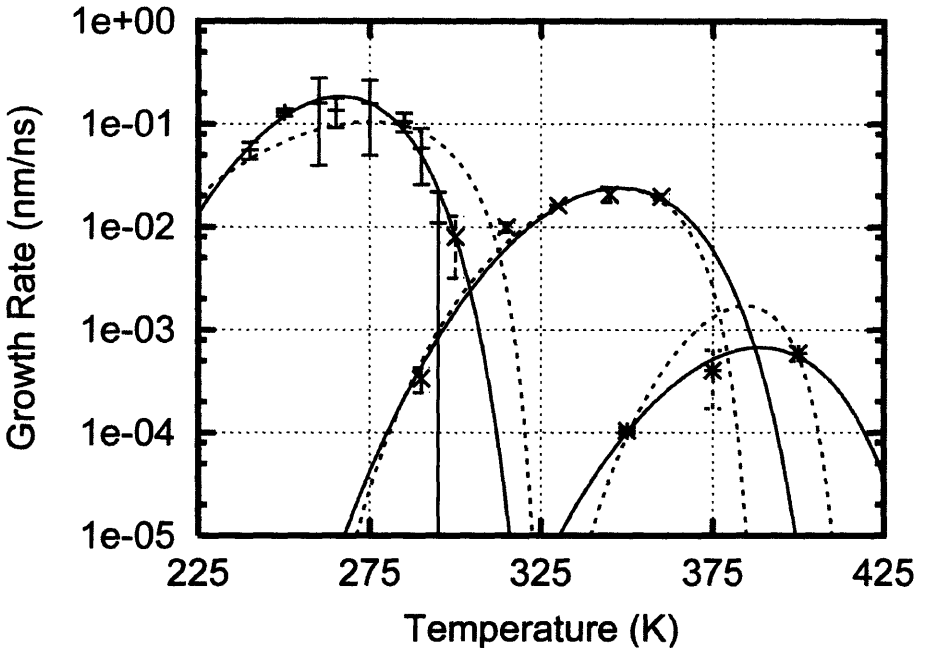

(b)

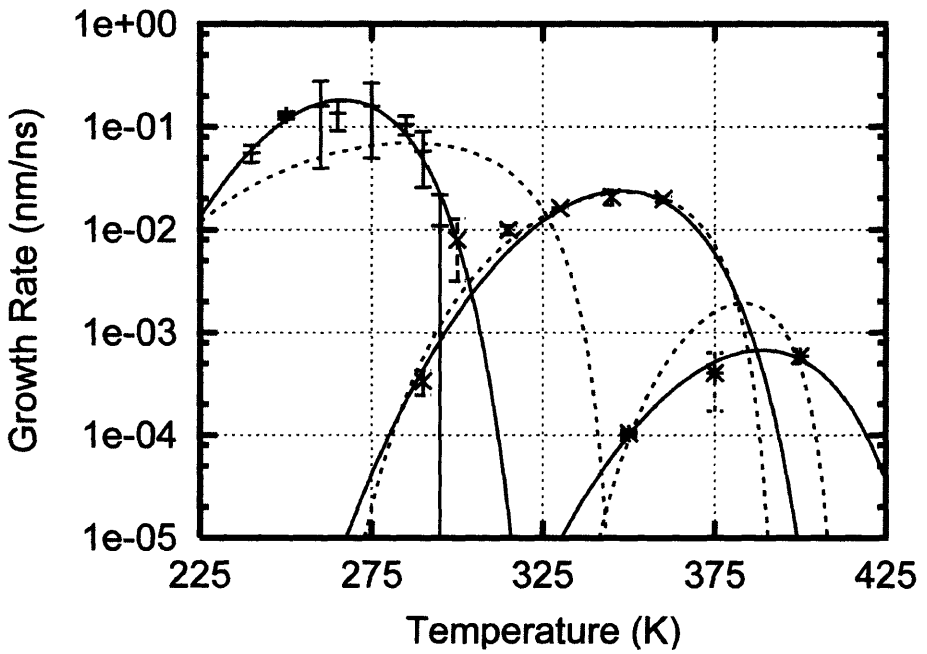

Figure 6.2 Our best fit equation for growth rate model as a function of temperature and molecular weight (solid lines), for the growth rate data shown: the 102 C20 chain systems (+), the 42 C50 chain systems (×), and the 40 C100 chain systems(*). Best fits for other models, where MW dependence is incorporated through the critical points using Eqs. (6.12) and (6.13), as in our model. (a) van Krevelen's model; (b) Strobl's model.

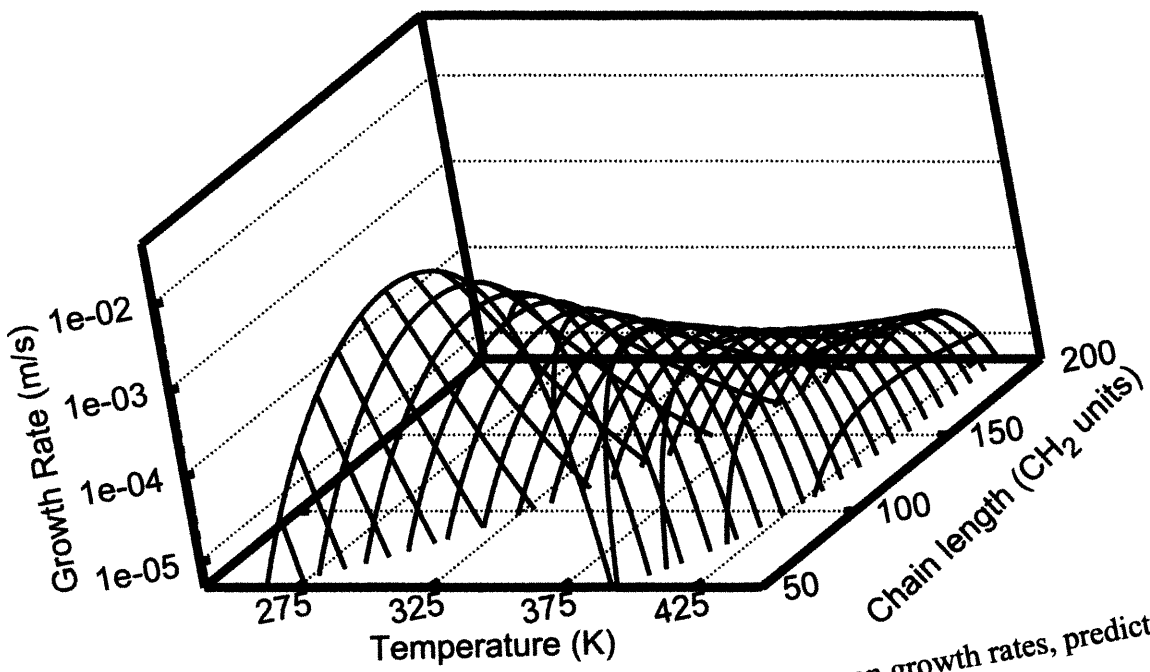

Figure 6.3 The effect of molecular weight and temperature on growth rates, predicted by our model equation Eq. (6.11), for Rouse dynamics.

Validation of these results from experimental observation is difficult, since our timescale of observation is much shorter than that of experimental methods. However, experimental and computational methods are beginning to converge towards the same timescale. Recent works on high speed crystallization have been able to measure crystallization rates for polyethylene over a wide range of temperatures from the melting temperature to near the temperature where the maximum rate occurs [Ratajski and Janeschitz-Kriegl 1996; Wagner and Phillips 2001]. It is worth noting that our predicted maximum crystallization rate for C100 is on the order of 10^{-3} m/s, while experiments indicate a maximum crystallization rate for polyethylene on the of order 10^{-4} m/s. This is in the range of our model extrapolations for the 150-200 chain length, as seen in Fig. 6.3. Beyond the entanglement length (approximately 150-200 beads), we do not expect that Rouse dynamics should be applicable; rather, reptation dynamics should come into play. However, the relatively weak molecular weight dependence of the maximum growth rate beyond the onset of entanglements [Hoffman 1982] and agreement between the predictions of our model for chains in the entangled regime and the experimental data for polyethylene suggest that the conformational relaxation of the length of the entangled segment may be the relevant kinetic barrier for high molecular weight polymers at large undercoolings.

Chapter 7

Extension of Alkane Growth Model to Polyethyelene

7.1 Model modification for the crossover from n-alkane to polyethylene behavior

In this chapter, we show how the model for n-alkane crystal growth at high undercooling, previously determined from molecular dynamics simulations in Chapter 6, can be used to model polymer crystallization during melt processing. During fiber spinning and film blowing, crystallization of polymers often takes place at large undercooling, where the crystallization behavior is least understood. Lauritzen and Hoffman estimated the kinetic restrictions at large undercoolings by modeling deviations from thermodynamically-limited experiments at small undercoolings [Lauritzen and Hoffman 1973]. This indirect approach was necessitated by the difficulty in obtaining reliable data for polymer crystallization rates at high undercooling using experimental techniques. Using molecular simulation, however, we can readily generate growth rates for alkanes at large undercoolings. Furthermore, the simulations can provide a first-principles basis for incorporating the kinetic restrictions into a polymer crystal growth rate model. By incorporating the best experimental data for high speed polyethylene

crystallization with our simulation data, we show that growth rates of n-alkanes and polyethylene can be described by the same relationship.

In Chapter 4, using non-equilibrium molecular dynamics simulations, we calculated crystal growth rates for n-eicosane (C20) at undercoolings of 50 to 100 °C where the rates are on the order of 10^{-1} m/s, too fast to measure by most experimental techniques. We subsequently reported growth rate data for C50 and C100, also as a function of temperature in Chapter 5.

There alkane crystal growth rates were modeled using the same form of equation as that used by Lauritzen and Hoffman for the thermodynamic driving force. However, unlike existing data for high molecular weight polymers, we observe a strong molecular weight dependence for crystal growth in alkanes [Lauritzen and Hoffman 1973]. This molecular weight dependence provides insight into the nature of the conformational barrier not only for alkanes, but also for polymers crystallizing at large undercooling, which is usually modeled by an Arrhenius-type free energy barrier [Armistead and Hoffman 2002]. By performing molecular dynamics simulation for alkanes of different molecular weights, we were able to quantify the molecular weight dependence of the growth rate for a range of alkanes below the entanglement molecular weight. For these alkanes, the molecular weight dependence was found to be well-described by that of the Rouse relaxation time. By applying the Rouse time to the model given by Eq. (6.11), the model for crystal growth rate of n-alkanes, as a function of temperature T and chain length N, is:

$$G(T,N) = G_0\left(\frac{N_0}{N}\right)^{2n} \exp\frac{2.303nc_1(T-T_g(N))}{c_2+(T-T_g(N))}\exp\left[-\frac{C}{T}\left(\frac{T_m(N)}{T_m(N)-T}\right)\right] \tag{7.1}$$

where G_0 is a rate pre-factor for a reference chain of length N_0 at its glass transition point T_g. T_m is the equilibrium melting temperature, and C is a characteristic thermodynamic constant for the polymer, quantifying the ratio of the surface energy of a nucleus to the lattice energy gained by crystallization. The first half of Eq. (7.1) captures the kinetic barrier for crystallization. The molecular weight dependence is determined from the ratio of Rouse relaxation times, raised to the power of n. The temperature dependence arises from the monomeric friction coefficient, which can be described by the WLF relation, modified by n, using the WLF constants c_1 and c_2 [Williams et al. 1955]. In addition, there is a molecular weight dependence of the glass transition temperature, based on the Fox and Loshaek equation that was given previously as Eq. (6.12). We use this relation again, which is described by

$$\frac{1}{T_g(N)} = \frac{1}{T_g^{\infty}} + \frac{C_g}{\left(T_g^{\infty}\right)^2}\frac{1}{N} \tag{7.2}$$

where T_g^{∞} is the asymptotic value of T_g at infinite molecular weight, and C_g is a constant. The similar molecular weight dependence of the melting temperature, given by Eq. (6.13) is also used once more, described by

$$\frac{1}{T_m(N)} = \frac{1}{T_m^\infty} + \frac{C_m}{\left(T_m^\infty\right)^2}\frac{1}{N} \tag{7.3}$$

where T_m^∞ is the asymptotic value of T_m at infinite molecular weight and C_m is a constant.

While the model given in Eq. (7.1) predicts growth rates for short alkanes with precision, it must be adapted in order to address the behavior of entangled systems. Interestingly, we observe that the predictions of the model for growth rates near the entanglement molecular weight (~ 150 CH_2 units) converge to recent high-speed crystallization rates for polyethylene. As we expect, the equation does not hold past the entanglement length, where a change in the relaxation mechanism occurs. For entangled chains, reptation dynamics are typically observed in the bulk phase. However, while Rouse behavior adequately describes the conformational relaxation required for crystallization in unentangled systems, reptation behavior does not properly describe the relaxation relevant for crystallization of an entangled system [Hoffman 1982].

Both theory and our previous work suggest that reptation is not the relevant mode of motion of chains relevant to crystallization. Reptation would imply growth rates with enhanced molecular weight dependence past the entanglement molecular weight, when in fact, a sharp drop in the molecular weight dependence is observed for most polymers, instead. Furthermore, our observations of the surface nucleus from molecular dynamics simulations at high undercooling indicate that growth proceeds before full extension of chains even for C50 and C100 chains. In addition, the formation of the surface nucleus, which is the rate-limiting step in growth, involves multiple short stems near the crystallizing surface, instead of a long length of a single chain. These observations

suggest that conformational rearrangement is the mechanism for conversion of chain segments at the surface into crystal stems, rather than the "drawing in" of a chain by reptation. Hoffman suggested that the lack of molecular weight dependence of the transport factor in highly undercooled systems (Regime III), could be explained if the kinetic barrier referred not to a reptation barrier (as might be the case in Regime I and II), but instead to "the retardation associated with slack portions of the pendant chains."[Hoffman 1982] However, the lack of a precise interpretation of this effect has so far created a gap between alkane and polyethylene crystal growth models. We suggest that the kinetic barrier to crystal growth for entangled polymers can be interpreted as that associated with the Rouse relaxation for chain segments of length equal to the entanglement molecular weight.

The transport term for polymer crystallization can be formulated in the same way as it was for alkanes, since we have addressed how the restrictions of chain movement affect crystallization though our alkane simulations. In accord with Hoffman, we postulate that the relaxation time of a segment of the entanglement length is the relevant relaxation time for crystallization, rather than the reptation relaxation time for the full chain. This concept suggests that, for long chains, the dependence of the relevant relaxation on the chain length is fixed by the entanglement length, resulting in an equation similar to Eq. (7.1) that can be used to model polymer crystal growth:

$$G(T, N > N_e) = G_0 \left(\frac{N_0}{N_e} \right)^{2n} \exp \frac{2.303 n c_1 (T - T_g(N))}{c_2 + (T - T_g(N))} \exp \left[-\frac{C}{T} \left(\frac{T_m(N)}{T_m(N) - T} \right) \right] \tag{7.4}$$

where N_e is the entanglement molecular weight. Because the glass transition temperature and melt temperature still retain slight molecular weight dependences, this equation still allows for the weak molecular weight dependence that is observed empirically for polymers. This approach provides a theoretical basis to the commonly accepted model for polymer crystal growth, and extends it to encompass alkane crystal growth as well.

7.2 Parameterization from Both n-Alkane and Polyethylene Data

We apply Eq. (7.1) and Eq. (7.4) to model both simulated and experimental data for crystal growth. For alkanes, we used the simulated data reported previously for C20, C50 and C100. For polymers we use the recent experimental data for high-speed crystal growth of polyethylene generated by Ratajski and Janeschitz-Kreigl[Ratajski and Janeschitz-Kriegl 1996], and independently by Wagner and Phillips [Wagner and Phillips 2001]. In addition, several clarifications are necessary. First, due to forcefield inaccuracies and limitations of the simulation methods, T_g and T_m for the simulated alkanes are not known accurately. In this case, we invoke Eq. (7.2) and Eq. (7.3) and include the parameters T_m^∞, T_g^∞, C_m, and C_g in our fitting procedure. For the experimental polymer system, we use the experimentally determined T_m and T_g. Second, by using a single value of C for both alkanes and polymers, we imply a single common mechanism for nucleation, which we believe to be appropriate at large undercooling (Hoffman's Regime III). This may not be appropriate for low undercoolings (Regimes I and II), but should be the relevant range for most polymer processing operations. Finally, it should

be emphasized that this is only a model for crystal growth, not crystallization in its entirety. For the latter, a model for primary nucleation is also required.

We solve iteratively for parameters of Eq. (7.1) through (7.4). As an initial guess, we use the parameters reported previously for the simulated alkanes in Chapter 6. G_0 and C were then refined by non-linear least squares fitting to get the best fit to the data of Ratajski and Janeschitz-Kreigl and Wagner and Phillips. The new values of G_0 and C were then used to refine the values of n, T_m^∞, T_g^∞, C_m, and C_g, by non-linear least squares fitting to the alkane data. This two-step procedure was performed iteratively until converged. The results are shown in Table 7.1.

Figure 7.1(a) shows the fit to the alkane simulation data. Figure 7.1(b) shows the fit to the experimental data using T_g=190 K and T_m=416 K, as reported by Wagner and Phillips for their sample. Reasonable fits are obtained to all 5 sets of data. Deviations occur at low undercooling, where presumably the nucleation mechanism changes from Regime III (normal) growth to Regime II (layer) growth. The ability to model alkanes and polyethylene with the same parameters lends support to the interpretation of the conformational barrier described above and in Eq. (7.1) and Eq. (7.4). The explicit molecular weight dependence becomes a constant at high molecular weights, as this local relaxation of an entangled system is effectively unaltered by the length of the chain. An implicit molecular weight dependence still exists though the glass transition temperature and melt temperature.

If we assume T_g and T_m to have molecular weight dependence given by Eq. (7.2) and (7.3), then we can calculate the maximum growth rate as a function of molecular weight for polymers, which has proven to be difficult to quantify, due to polydispersity of

Table 7.1
Calculated parameters for the model given by Eqs. (7.1),(7.2), (7.3), and (7.4), based on iterative fits between our simulation data and polyethylene experimental data.

Parameter	Overall Fit	
G_0	1.946e-25	m/s
C_{therm}	341	K
N	2.03	
T_m^{∞}	496	K
T_g^{∞}	304	K
C_m	5.08e3	CH_2•K
C_g	1.17e4	CH_2•K

(a)

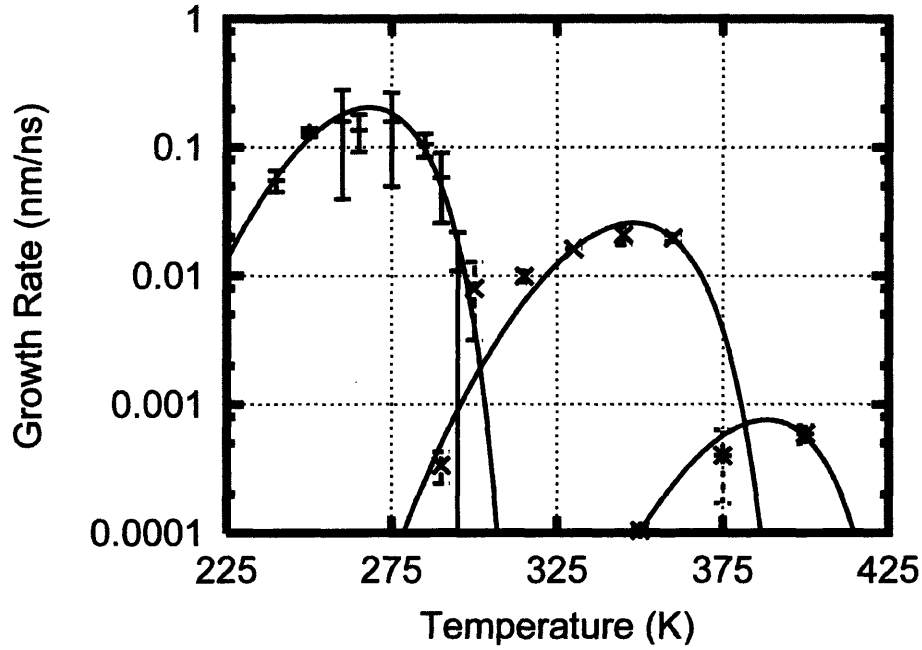

(b)

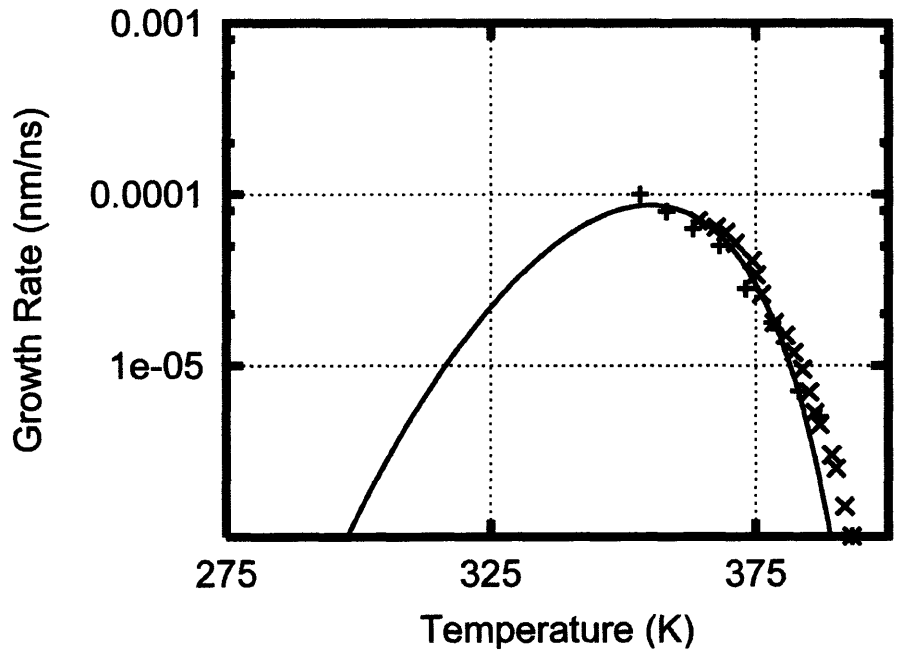

Figure 7.1 Fit of the model equation to simulation and experimental data. (a) simulated growth rates of alkanes fit to Eq. (7.1): C20 (+), C50 (×), and C100 (*). (b) experimental growth rates of polyethylene samples fit to Eq. (7.4): data of Ratajski *et al.* (+), and Wagner *et al.* (×).

experimental samples. This is shown in Fig. 7.2, where the transition at the entanglement molecular weight is highlighted. The maximum rate increases with molecular weight for short alkanes, where it is dominated by the width of the temperature window ($T_m - T_g$) available for crystallization, until it passes through a maximum. Beyond the maximum, the maximum rate for alkanes is dominated by the power law dependence of Eq. (7.1) up to the entanglement molecular weight, M_e. Beyond M_e, the molecular weight dependence is purely a consequence of Eq. (7.2) and Eq. (7.3), and may explain why different scaling laws seem to be observed in different regions of this curve [Umemoto and Okui 2002].

7.3 Application of Model to Fiber-Spinning Process

To illustrate the use of Eq. (7.4), we model crystal phase growth in a "representative volume element" (RVE) of polyethylene, as it moves through the different temperature environments of a fiber-spinning process. This analysis is also applicable for several other processes, including film blowing and injection molding. To model two-phase growth, we use the Schneider rate equations [Schneider et al. 1988], which have recently been applied to the different morphologies of semi-crystalline polymer crystals [Huetter et al.]. We assume spherulitic crystallization, where 100% conversion implies a fully semi-crystalline material. For primary nucleation, we use the data of Eder *et al.*, who report that quiescent nucleation density is approximately 5×10^{14} nuclei/m^3, independent of temperature, for both high and medium density polyethylene [Eder et al. 1990]. The temperature profiles reflect the removal of heat by cooling air. We do not account for coupling of the temperature profile to heat evolution due to crystallization.

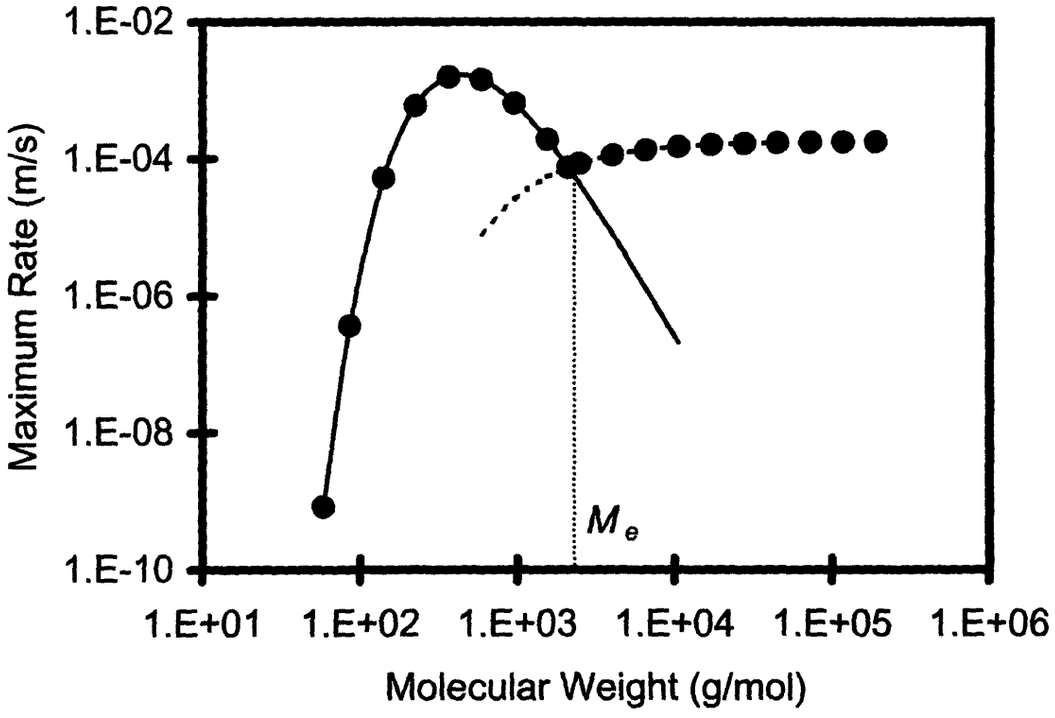

Figure 7.2 The maximum growth rate, where $\partial G(T,N)/\partial T = 0$, as a function of molecular weight, where $G(T,N)$ is obtained from Eq. (7.1) (solid line) for chains of length up to the entanglement molecular weight M_e of 150 beads (2.1e3 g/mol), and from Eq. (7.4) (dotted line) for lengths greater that 150 beads.

We consider two temperature profiles, one slow-cooled and the other fast-cooled, suggested by experimental spinline temperature profiles [Doufas et al. 2000; Paradkar et al. 2003]. For the two systems, we assume processing temperature profiles given in Fig. 7.3(a). Nucleation occurs instantaneously at $t = 0$. Using Eq. (7.4), we calculate the crystal growth rate, shown in Fig. 7.3(b). We then integrate the rate numerically, to obtain the unimpinged radius of a spherulite, shown in Fig. 7.3(c). The surface area and volume for each spherulite can be easily computed from the radius, using the spherical Minkowski functionals. Then using the density of nuclei and the growth rate, we can apply Avrami's statistical approximation for volume filling to get the degree of transformation from amorphous to semi-crystalline material as a function of residence time in the spinline:

$$\frac{\theta(t)}{\theta_\infty} = 1 - \exp\left(-\alpha \cdot \frac{4\pi}{3} \left(\int_0^t G(T(t'), N) dt' \right)^3 \right) \tag{7.5}$$

where the density of nuclei $\alpha = 5.0 \times 10^{14}$ nuclei/m^3 and $G(T(t),N)$ is given by Eq. (7.4). The result for the degree of transformation is shown in Fig. 7.3(d).

Interestingly, we predict different morphologies as a result of the different cooling rates. Under slow-cooling conditions, the residence time at high temperature, where growth rates are fast, is long enough to reach the point where impingement of nuclei occurs. The resulting fiber is nearly 100% semi-crystalline. In the context of fiber spinning, a segment of the fiber is completely crystallized by the time it reaches the draw wheel. Under fast-cooling conditions, one observes a brief surge in the rate of

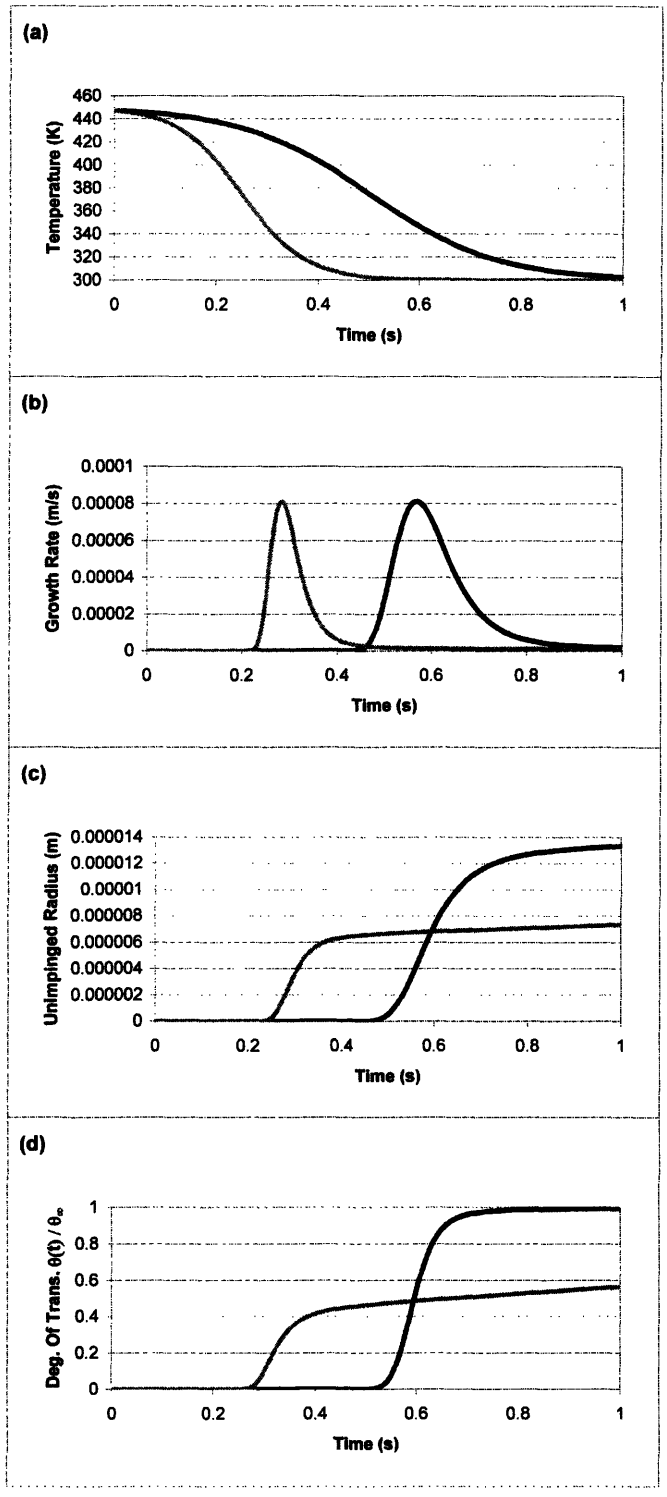

Figure 7.3 Crystal growth characteristics as a function of two a priori temperature profiles: slow-cooling (black), and fast-cooling (gray); (a) the temperature profiles as a function of time, (b) the growth rate as a function of time, calculated from Eq. (7.4), (c) the unimpinged radius of a spherulite, calculated by integration of the growth rate, (d) the degree of transformation of the system, calculated by Eq. (7.5).

crystallization as the temperature quickly passes though the range where crystallization is fast. The radius of the spherulite increases, but does not reach the level of impingement of the spherulites before such low temperatures are reached that crystallization is significantly slowed. The result is a degree of transformation that levels off far from a fully semi-crystalline system. In the fast-cooled fiber-spinning system, the crystallization is not complete by the time the RVE reaches the draw wheel. A large fraction of the RVE is still a subcooled amorphous melt with very little mobility, which still retains its visco-elastic behavior and continues to crystallize slowly through the post-draw phase. The difference in the rate of cooling allows for stretching and secondary crystallization to take place during post-spin drawing at room temperature, where relaxations are slow. This kind of process history can significantly improve properties, such as the stress-strain behavior of the final material.

Chapter 8

A Simplified Model via Kinetic Monte Carlo

8.1 Model Construction

In this chapter, we report a new generalized implementation of the kinetic Monte Carlo algorithm discussed in Chapter 2, and apply it specifically to model crystal growth rates in melt polymers. This algorithm allows for nucleation of multiple chain segments in three dimensions on a pre-existing surface. We classify states based on the occupancy, availability for growth, and connectivity of chains and calculate rates for KMC moves based on occupancies of neighbor sites. The KMC moves that are employed are based on observation of mechanisms from molecular dynamics. We use previously generated rate data from molecular dynamics simulations of eicosane (C20) to calibrate the KMC simulation. In addition, the framework of the simulation gives it the ability to yield different crystal structures, depending on the energy penalties for moves, and contains no inherent bias towards any morphologies.

This implementation of KMC for polymer crystal growth classifies sites by occupancy, availability for growth, and connectivity of chains. We simulate the crystalline phase of the polymer on a three-dimensional cubic lattice, where each lattice

site represents a simplified CH_2 or CH_3 polymer bead; however, if parameterized as such, a lattice site may represent a series of beads, a helix repeat unit, or any crystalline conformer. Only the crystalline region is modeled, since movement in the amorphous region is faster than in the crystalline region, and can be considered a "lumped state" to simplify the simulation. We assume that the amorphous region affects the rate of crystallization through the activation energy barrier, related to the mobility of chains in the melt state, as discussed in detail later. When lattice sites are occupied by the crystalline conformer, we retain information about the connectivity of the polymer chain through that point in the crystal, by tracking the two "facets" through which the polymer chain enters or leave the lattice point. The method accounts not only for the connectivity, but for the conformation in the occupied site, which is either "straight" or "kinked," where straight conformations are generated when the angle through the site is 180° and kinked conformations are generated when the angle is 90°. Figure 8.1 shows the matrix of occupancy states that is generated by combinations of the six directional vectors, numbered one to six.

In addition, we require connectivity between lattice points by designating continuity through "face pairs." Figure 8.2 shows the pairing of face pair vectors, by requiring the connected neighbor sites to be matched to the face pair of its neighbor. We track "active sites" that connect the crystal with the amorphous, which are the locations at which further growth of the crystal can take place. Because these sites are connection points to the amorphous phase, chains in the next layer of growth are not allowed to grow over an active site; active sites are always exposed to the melt through the facet normal to the crystal surface, labeled facet three.

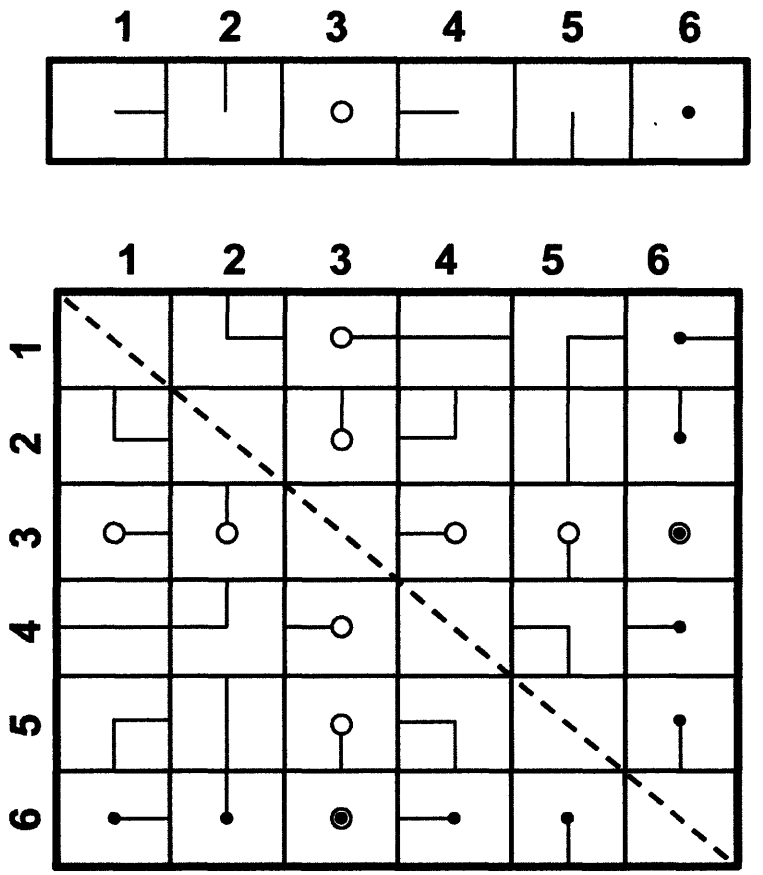

Figure 8.1 Top row highlights a chain going through one of the six faces of the cube. In each lattice site, the line touches the face through which the chain passes into or out of the lattice site. The filled circle indicates a line passing through the face parallel to the plane of the page and farthest from the viewer; the open circle indicates a line passing through the face parallel to the plane of the page and nearest to the viewer. The bottom matrix shows all possible states of occupancy that are generated by requiring a chain cross through two faces of the cube, for entry and exit.

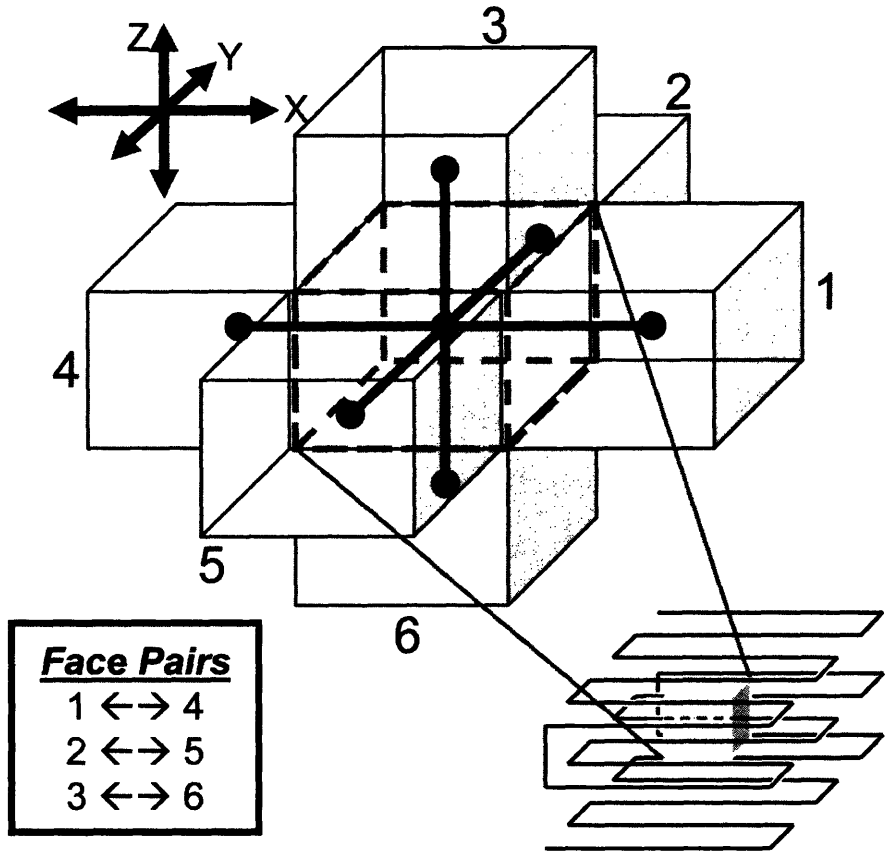

Figure 8.2 Illustration of the face pair requirement for connectivity, where a chain leaving through a certain face the lattice site must be connected to the neighboring site by its face pair.

The basic KMC moves involve changes in occupancy made to two neighboring lattice points. The types of possible KMC moves were generated by considering all combinations of occupancy, connectivity, and the number of active sites, for two neighboring sties. Allowed moves entail the creation or elimination of a chain connection between two neighboring sites. Figure 8.3 shows a table of combinations of these states, and the possible moves they generate, as well as examples of those moves. Of the nine possible combinations, only four are states in which moves are possible. These moves are addition of an occupied site, removal of an occupied site, nucleation of a new chain segment, and desorption of a new chain segment.

These four moves between two neighboring sites are responsible for controlling the growth rate of the crystal. Addition is the process of growing the chain by propagating the active site to a neighboring empty site. Removal is the reverse process of addition, whereby an active site is moved one lattice site back along the chain, leaving an unoccupied site, representing the lumped melt state behind. Nucleation can occur in two unoccupied lattice sites, which lie on two occupied sites that are not active. A nucleation event generates two connected, neighboring active sites, which can be seen as a small segment of amorphous polymer coming into registry with the crystal surface. Desorption is the reverse process of nucleation, destroying two neighboring, connected active sites, and leaving the sites unoccupied as the crystal segment comes out of registry and returns to amorphous conformation. The rates of all these moves are dependent on the number of occupied nearest neighbor sites and the conformation of the chains created or removed. These moves are the natural consequence of the design of the simulation, with the assumption that most complex moves can be decomposed into these simple two-site,

Occupancy	Active Sites	Connectivity	Type	Example	
				Lattice change	Internal Energy Change $\Delta E_{i \to j}$
0	0	-	NUCLEATION	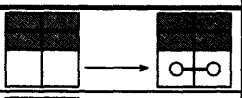	$2 \times (-\frac{1}{2}\Delta E_{NN}) + 2 \times (\Delta E_{KINK})$
1	0	-			
1	1	-	ADDITION		$2 \times (-\frac{1}{2}\Delta E_{NN}) + 1 \times (\Delta E_{KINK})$
2	0	N			
2	0	Y			
2	1	N			
2	1	Y	REMOVAL	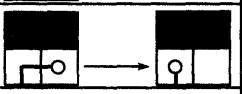	$-2 \times (-\frac{1}{2}\Delta E_{NN}) + -1 \times (\Delta E_{KINK})$
2	2	N			
2	2	Y	DESORPTION		$-2 \times (-\frac{1}{2}\Delta E_{NN}) + -2 \times (\Delta E_{KINK})$

Figure 8.3 The generation of KMC moves, by considering two neighboring sites and classifying by occupancy, connectivity and the number of active sites. Nucleation, addition, removal and desorption moves are generated. Examples of moves are given where the white sites are being considered for moves. Changes in internal energy of the white sites, computed by Eq. (8.11), are given based on conformational changes at the white sites and the interactions occurring with the grey example neighbor sites.

nearest neighbor moves. All moves have corresponding reverse moves to satisfy microscopic reversibility, as applied to non-equilibrium reactions. Birth processes and the associated death processes, i.e. nucleation and desorption or growth and removal, have the same transition state and mechanism, differing only in direction. For the equilibrium system that occurs at the melt temperature, detailed balance is satisfied completely.

8.2 Theoretical Framework

Our kinetic Monte Carlo algorithm is based originally on the work of Bortz, et. al. [Bortz et al. 1975], which has been expounded upon by the theoretical work of Fichthorn and Weinberg [Fichthorn and Weinberg 1991]. The KMC cycle consists of four steps: enumerating the possible moves, calculating the rates of available moves, choosing a move based on the rates, and incrementing the time accordingly. Figure 8.4 shows a schematic flowchart of the implementation.

First, we assemble the list of all possible moves in the system. The rate for each move is then computed, based on the free energy of activation $A_{act,i\to j}$, using the Arrhenius formulation,

$$k_{i\to j} = k_o \exp\left(\frac{-A_{act,i\to j}}{kT}\right) \tag{8.1}$$

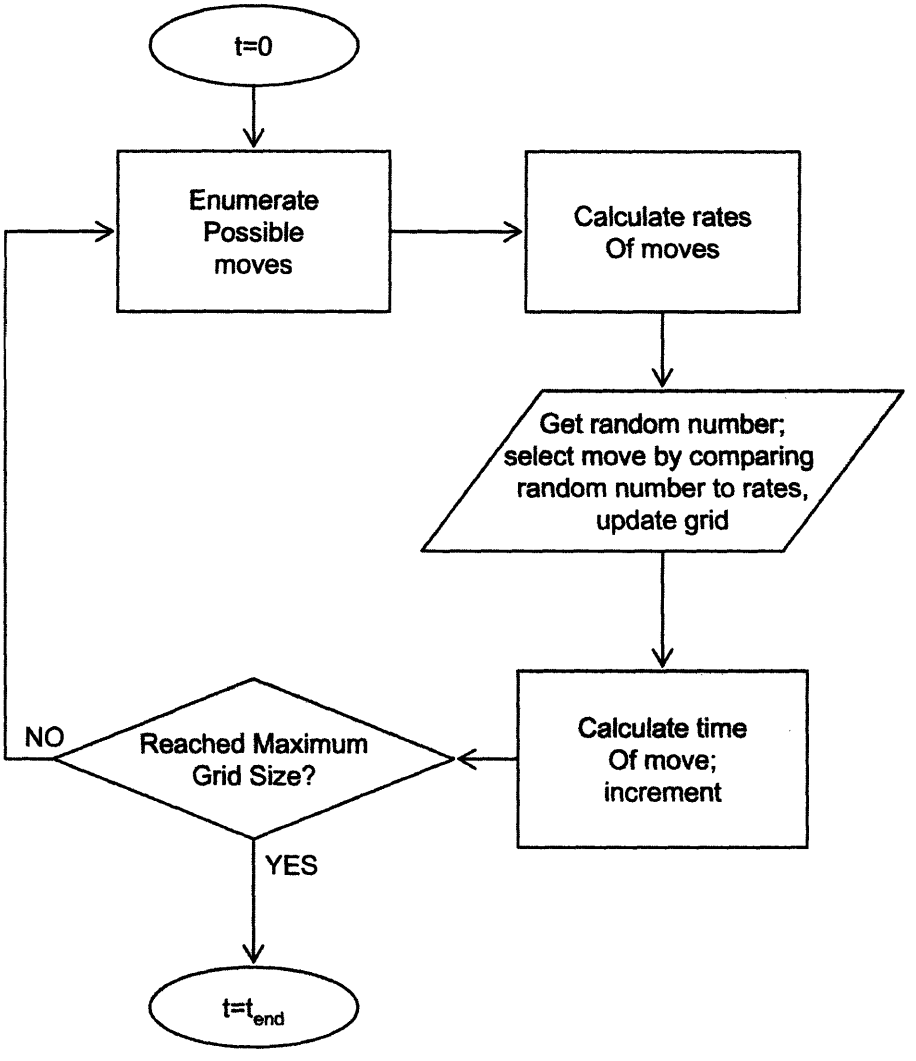

Figure 8.4 Flowchart showing the implementation of the kinetic Monte Carlo algorithm.

where $k_{i\to j}$ is the rate of going from state *i* to state *j*, and k_0 is the rate pre-factor for the process, based on the attempt rate for the move, from transition state theory.

Moves are selected by calculating the probability of their occurrence, based on the other competing moves, according to the equation,

$$p_{i\to j} = \frac{k_{i\to j}}{\sum_{m=1}^{n_m} k_{i\to m}} \tag{8.2}$$

where $p_{i\to j}$ is the probability of the move taking the system from state *i* to state *j*, and n_m is the total number of moves available leaving state *i*. Once the probability of all available moves is known, we can select a move based on the generation of a uniform random number from 0 to 1. Fichthorn and Weinberg [Fichthorn and Weinberg 1991] have shown that the time elapsed during a move is related to the rates of all the available moves by the following equation,

$$\tau_i = -\frac{1}{\sum_{m=1}^{n_m} k_{i\to m}} \ln(U) \tag{8.3}$$

where τ_i is the time required to leave state *i*, and *U* is a uniform random number between 0 and 1. Once a move is selected, we increment time according to this relation.

It is often assumed that the free energy barrier does not vary with temperature in a KMC simulation. This assumption is usually made because differences in internal

energy, which can be computed from an interaction potential, are accepted as approximations for differences in free energy. This approximation implies that the entropies of any two states are approximately the same and exhibit the same temperature dependence. This makes sense for lattice sites that represent objects with no internal degrees of freedom. In the vicinity of a phase transition, however, this approximation does necessarily not hold. At the phase transition temperature, the free energies of crystal and melt are the same, giving rise to equal rates of crystallization and melting. Since the internal energies of crystal and melt sites are not equal, their entropies are necessarily unequal as well. A lattice site that can alternate between being crystalline and melt, as is done here, must also account for the higher intrinsic entropy of the latter. However, in order to capture the temperature dependence of transition rates near the melt temperature, this variation should be considered. If the internal energy is used rather than the free energy, the first order transition will not be observed. Even though the forward and reverse rates will be closer to each other as temperature increases, it will be impossible to reach a regime where the rate of transition from crystal to melt is greater than the rate of transition from melt to crystal, yielding an infinite melting temperature.

Therefore, we decompose the energy barrier to account for the temperature dependence of these interactions. We begin with the equation of Turnbull and Fischer [Turnbull and Fisher 1949], which gives us the theoretical framework to break up the total free energy barrier into a thermodynamic part and a diffusive part. We parameterize the activation energy barrier $A_{act,i\to j}$ for a move from state i to state j, from Eq.(8.1) in terms of the activated state barrier, a melt mobility barrier, and the thermodynamic difference, such that

$$A_{act,i\to j}(T) = A^{\dagger}_{act} + E_D(T) + \max\left[0, \Delta A_{i\to j}(T)\right] \tag{8.4}$$

where $\Delta A_{i\to j}(T)$ is the Helmholtz free energy of the final state j minus the free energy of the initial state i, $E_D(T)$ is the energy barrier due to the mobility restrictions of the melt phase, and $A_{act}^{\dagger}$ is the additional barrier (over and above the melt mobility barrier) required to reach the activated state for the transition to occur. Equation (8.4) is written such that the melt mobility barrier is the present for the forward and reverse reactions, since a relaxation in the melt phase is required both for drawing a bead in from the melt to join the crystal, and for returning a bead to the melt from the crystal. The Helmholtz free energy difference is additively applied to the total barrier when it is positive, such that the transition state is the same in both the forward and reverse direction. Figure 8.5 illustrates the breakdown of the barrier in the forward and reverse direction, according to Eq. (8.4), and how it is applied for four temperatures.

Because of the large temperature dependence of the free energy difference and the mobility barrier, we assume that the activated state barrier is temperature independent, and can be lumped into the kinetic pre-factor, such that

$$k_0^* = k_0 \exp\left(\frac{-A^{\dagger}_{act}}{kT}\right) \tag{8.5}$$

where k_0^* is the kinetic pre-factor, including the activated state barrier. Then the temperature dependent barrier $A^*_{act,i\to j}(T)$ can be written in terms of the mobility barrier and the free energy difference, and is given by

$$A^*_{act,i\to j}(T) = E_D(T) + \max\left[0, \Delta A_{i\to j}(T)\right]. \tag{8.6}$$

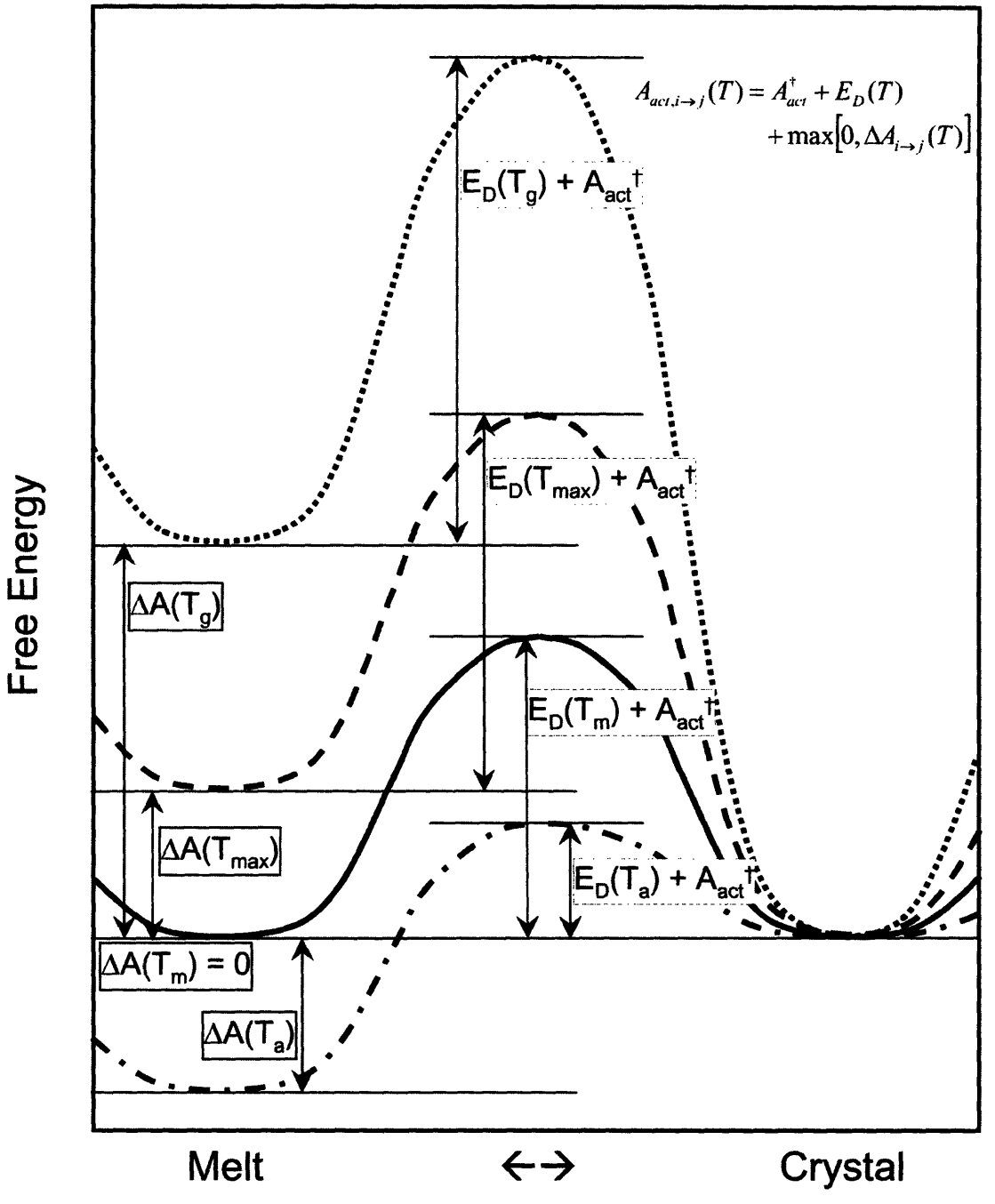

Figure 8.5 Illustration of the breakdown of the free energy barrier into components at four temperatures. When decomposing the energy barrier into a free energy difference $\Delta A_{i\to j}(T)$ and a melt mobility and activated state barrier $E_D(T) + A_{act}^{\dagger}$, Eq.(8.4), shown on the graph, can describe the free energy barrier in either direction, at any temperature. Illustrative curves are shown for four temperatures: the glass transition temperature T_g (dotted), the temperature of maximum crystal growth rate T_{max} (dashed), the melt temperature T_m (solid), and a temperature above the melt temperature where the amorphous phase is stable T_a (dotted-dashed).

This allows us to rewrite Eq.(8.1), in terms of the temperature-dependent components of the barrier. The revised equation is given by

$$k_{i\to j} = k_0^* \exp\left(\frac{-A^*_{act,i\to j}(T)}{kT}\right). \tag{8.7}$$

The pre-factor k_0^* is considered temperature independent and is the same for all moves. This form of the rate equation is implemented in our KMC code, where the activated state barrier is included in the pre-factor, and the energy barrier is given by Eq. (8.6).

The effect of temperature on the melt mobility barrier and the Helmholtz free energy difference are also illustrated in Fig. 8.5. The Helmholtz free energy difference between the melt and crystal state, which is the thermodynamic driving force for phase change, is zero at the melt temperature T_m, yielding a growth rate of zero. At temperatures above the melt temperature, illustrated in Fig. 8.5 as T_a, the free energy of the melt is lower than that of the crystal phase, such that melting occurs and the crystallization rate is negative. For temperatures lower than T_m, such as T_{max} and T_g on Fig. 8.5, the thermodynamic driving force towards crystallization leads to positive crystallization rates. However, the melt mobility barrier also has a strong temperature dependence that can be seen in Fig. 8.5. As the temperature decreases, the melt mobility barrier increases, since drawing in a chain from the melt or returning it to the melt requires more energy. Because of this higher barrier at lower temperatures, such as near T_g on Fig. 8.5, the rate of crystallization decreases significantly, despite the high driving force towards crystallization.

The Helmholtz free energy difference can be estimated using internal energy and thermodynamic relations at the melting temperature. The free energy is given by

$$\Delta A_{i\to j}(T) = \Delta E_{i\to j} - T\Delta S_{i\to j} \tag{8.8}$$

where $\Delta A_{i\to j}$ is the change in Helmholtz free energy, $\Delta E_{i\to j}$ is the change in internal energy, T is the temperature, and $\Delta S_{i\to j}$ is the change in entropy. At the melting temperature T_m, there is no change in free energy between the two states. A relation exists between the change in internal energy and the change in entropy, given by

$$\Delta S_{i\to j} = \frac{\Delta E_{i\to j}}{T_m}. \tag{8.9}$$

This equation is valid near T_m, where the major contribution to the difference in entropy is due to the difference in available states between the crystalline and amorphous phase. Far below T_m, the available states are also limited by temperature. However, the rates in this region are more significantly affected by the high melt mobility barrier, allowing us to use this approximation at low temperatures as well. Thus, the free energy difference can be approximated as a function of the internal energy and temperature:

$$\Delta A_{i\to j}(T) = \Delta E_{i\to j} - \frac{T\Delta E_{i\to j}}{T_m} = \Delta E_{i\to j}\left(1 - \frac{T}{T_m}\right) = \frac{\Delta E_{i\to j}\Delta T}{T_m} \tag{8.10}$$

where ΔT is the undercooling $T_m - T$. The reader might recognize this term from Chapter 6, where we parameterized the growth rate in terms of this quantity. In Eq.

(6.11), the undercooling appears in the denominator of the second exponential term, which is the thermodynamic driving force for growth, whereas here, when Eqs. (8.6), (8.7) and (8,10) are combined, it appears in the numerator of the exponential term in the rate. It is worth highlighting why this difference exists. Equation (6.11) is derived based on nucleation theory for a two-dimensional nucleus, where a "critical nucleus" is formed once the bulk free energy of the surface nucleus is greater than the surface energy created by the nucleus. However, for the KMC simulations, nucleation theory is not applied in order to generate the rate equations. *Nucleation*, as we use it in the KMC simulations, is only meant to describe the move in which a new segment of chain comes into crystallographic registry with the crystal, and is not related to the "critical nucleus" described in nucleation theory. The behavior modeled in nucleation theory, if applicable, should be a consequence of a high energy chain nucleation move, stabilizing itself by growth or by the presence of other nucleating segments. The filling of neighboring sites lowers the energy because of the way the occupied sites on the lattice interact with one another, as is described below.

The change in internal energy $\Delta E_{i\to j}$ can be expressed in terms of the energy due to nearest neighbor interactions and the chain conformational energy. Nearest neighbor interactions are parameterized in terms of E_{NN}, which represents the change in energy that arises when two neighboring crystalline conformers pack together tightly and have the same conformation. A nearest neighbor interaction is formed when both "facets" of an occupied site, through which the chain enters and leaves the lattice point, match the facets of a neighboring occupied site; when only one of the facets match, half of the interaction energy is awarded. There is also a change in internal energy that depends on the

conformation that a crystalline site adopts. The crystalline conformations are classified into "kinked" and "straight" conformations, where straight conformations are the states found in the bulk of the equilibrium polymer crystal and kinked conformations change the direction in which the chain grows, as can be seen in Fig. 8.1. The internal energy of a segment of beads in the melt is an average of many conformers, but when it fits into the crystal lattice, it assumes one of these two specific types of conformations. For "straight" conformations, there is a decrease in internal energy, when compared to an average chain in the melt state. For "kinked" conformations, there is an increase in internal energy, compared to the melt state. If we assign the difference between the "straight" and the "kink" state to be E_{kink}, then we can partition the energy difference between the crystal conformation and the melt state, in terms of this value, using a second parameter δ. The energy change from locking a melt state into a "kinked" crystalline conformation is δ E_{kink}, while the energy change from locking a melt state into a "straight" crystalline conformation is -(1- δ) E_{kink}. For the purposes of this initial study, we assign δ a value of one which implies that there is little energetic benefit to creating a "straight" segment from the melt. This first order approximation is acceptable since most of the melt conformers are in the *trans* torsional conformation. This simplification yields a conformational energy change of zero if the bead packs in a "straight" conformation and E_{kink} for a kinked conformation. The total conformational energy change of the move is determined by looking at the number of kinks created or removed by a particular event. Therefore, in total, the free energy difference can be written as,

$$\Delta E_{i\to j} = \left[-\left(n_{NN}\times E_{NN}\right)+\left(n_{KINK}\times E_{KINK}\right)\right]_j - \left[-\left(n_{NN}\times E_{NN}\right)+\left(n_{KINK}\times E_{KINK}\right)\right]_i \qquad (8.11)$$

where n_{NN} is the total number of nearest neighbor interactions in either state i or j, and n_{KINK} is the total number of kinked conformations in either state i or j. An illustration of the usage of Eq. (8.11) is included for the example moves in Fig. 8.3, where example two example neighbor sites are also given. A nucleation move creates two kinked conformations, as a nucleation site is a spontaneous registry of two sites both containing kinks that connect to the melt phase, and a desorption move removes two kinked conformations.

For polymer systems, when T decreases significantly, the energy required to extend a chain in the melt increases dramatically. We have shown how E_D is related to the relaxation time of the chain in Chapter 6. Because of time-temperature super-positioning, the temperature dependence of E_D is derived from the WLF equation [Williams et al. 1955], and is given by:

$$E_D(T) = \begin{cases} \dfrac{C_D c_1 c_2 kT}{c_2 + T - T_g} & \text{for addition/removal moves} \\ C_{DN}\left(\dfrac{C_D c_1 c_2 kT}{c_2 + T - T_g}\right) & \text{for nucleation/desorption moves} \end{cases} \tag{8.12}$$

where the WLF constants c_1 and c_2 are 17.44 and 51.66 K, respectively, T_g is the glass transition temperature, and C_D is a variable that sets the magnitude of the energy barrier. Equation (8.12) was derived by converting the WLF exponential shown in Eq. (6.11) to the Arrhenius form given in Eq. (8.7), and moving the constant terms into the pre-factor. The diffusive barrier for nucleation and desorption moves is assumed to be different than

that of growth and removal moves, since the motion required for rearrangement of an nucleating/desorbing melt segment's conformation is different from the coupled motion required to add or removal a segment attached to an existing crystal. Therefore, the diffusive barrier for nucleation and desorption is also multiplied by C_{DN}, which is the fraction of the melt mobility barrier that is applied as the nucleation barrier.

In other approaches to KMC, E_D is often not considered explicitly and is factored out into the pre-factor since it is present in all moves. However, it is necessary to keep it explicit here in order to compare simulations conducted at different temperatures. The temperature dependence affects relaxation times on the scale of orders of magnitude, and will lead to different net rates of growth as a function of temperature. Although the thermodynamic driving force is very strong close to T_g, both the forward and reverse reactions are taking place on a very long time scale, due to glassy behavior. The decomposition of rates into a thermodynamic term and a melt mobility barrier allows us to understand the large change in rate behavior near the melting point and the glass transition point.

8.3 Validation and Rate Analysis

8.3.1 Comparison to previous KMC attempts

Doye and Frenkel [Doye and Frenkel 1999] conducted growth rate measurements for a two-dimensional single chain crystal, as mentioned in Chapter 2. We have validated our three-dimensional model against their work, but in order to do so, we introduce a slightly different framework for handling changes in energy with temperature. We

introduced a breakdown of energies into a thermodynamic and diffusive term in Section 8.2, to capture the behavior of rates at high and low temperatures. Doye and Frenkel were also able to achieve similar effects, by parameterizing in terms of internal energy differences, with an additional term for the entropy loss of the melt phase,

$$\Delta A_{amorph} = kT \log(1 + 4\exp(-E_{KINK} / kT), \tag{8.13}$$

which is based on the assumption that the melt part of the chain behaves as an ideal coil. They use this term in combination with nearest neighbor interactions and kink energies, which do not vary with temperature. We use their formalism in this section for comparison. However, we note that this equation allows us to reproduce a finite melting temperature, but cannot account for the drop off in the rate at T_g rather than absolute zero. The algorithm described above was first checked by comparison to previous work using kinetic Monte Carlo. In order to reproduce the work of Doye and Frenkel [Doye and Frenkel 1999], this requires restricting our simulation to a single chain crystallizing in two dimensions. In our system, this restriction is imposed by assuming a very high nucleation energy, such that only the nearest neighbor energy and the kink energy are relevant, and folding is the mode by which the crystal is formed. We set up the simulation using an initial fixed stem of length 50 lattice sites on an underlying infinite crystal surface, as was done by Doye and Frenkel. We allow the chain to crystallize by addition and removal moves in either a straight or kinked configuration, where the energy of a kinked state E_{KINK} is equal to eight times the nearest neighbor energy E_{NN}. We use Doye and Frenkel's value for entropy loss for the amorphous phase, given by Eq. (8.11).

We performed simulations over a range of values for kT, from 2 E_{NN} to 3.5 E_{NN}. Each simulation measured growth characteristics for the growth of 40 stems. Growth rates and average stem lengths were calculated for comparison to the work of Doye and Frenkel. The growth rate as a function of temperature is shown in Fig. 8.6(a). The average stem length for the first 40 stems is shown as a function of temperature in Fig. 8.6(b). Both measurements show our algorithm able to capture the behavior of previous work on single chains crystallizing in two dimensions.

8.3.2 Comparison to molecular dynamics for n-eicosane

In this section, we use the data from our previous molecular dynamics simulation to match growth rates as a function of temperature, by adjusting the values for the free energy parameters. Four main parameters are present in the case of C20 crystallization: C_D, C_{DN}, E_{NN}, and E_{KINK}. We use the values of T_m and T_g, based on our previous molecular dynamics simulations, using 338 K for T_m and 124 K for T_g of n-eicosane, as given in Table 6.2. We search this parameter space to approximate the temperature at which the maximum rate occurs, and the shape of that temperature dependence.

The full multi-chain three-dimensional model is applied to the crystallization of n-eicosane (C20). The system is set up to be analogous to molecular dynamics simulations we have conducted on C20, discussed in Chapter 4. The lattice size is 20 x 6 x 40 sites, where the x-direction is the direction of chain orientation of the pre-existing layer, and the z-direction is the surface normal. Periodic boundaries exist in the x and y directions, as was the case with the MD simulations. One layer of 6 n-eicosane chains is fixed as the seed for growth. For finite chains such as C20, when the chain length has reached the

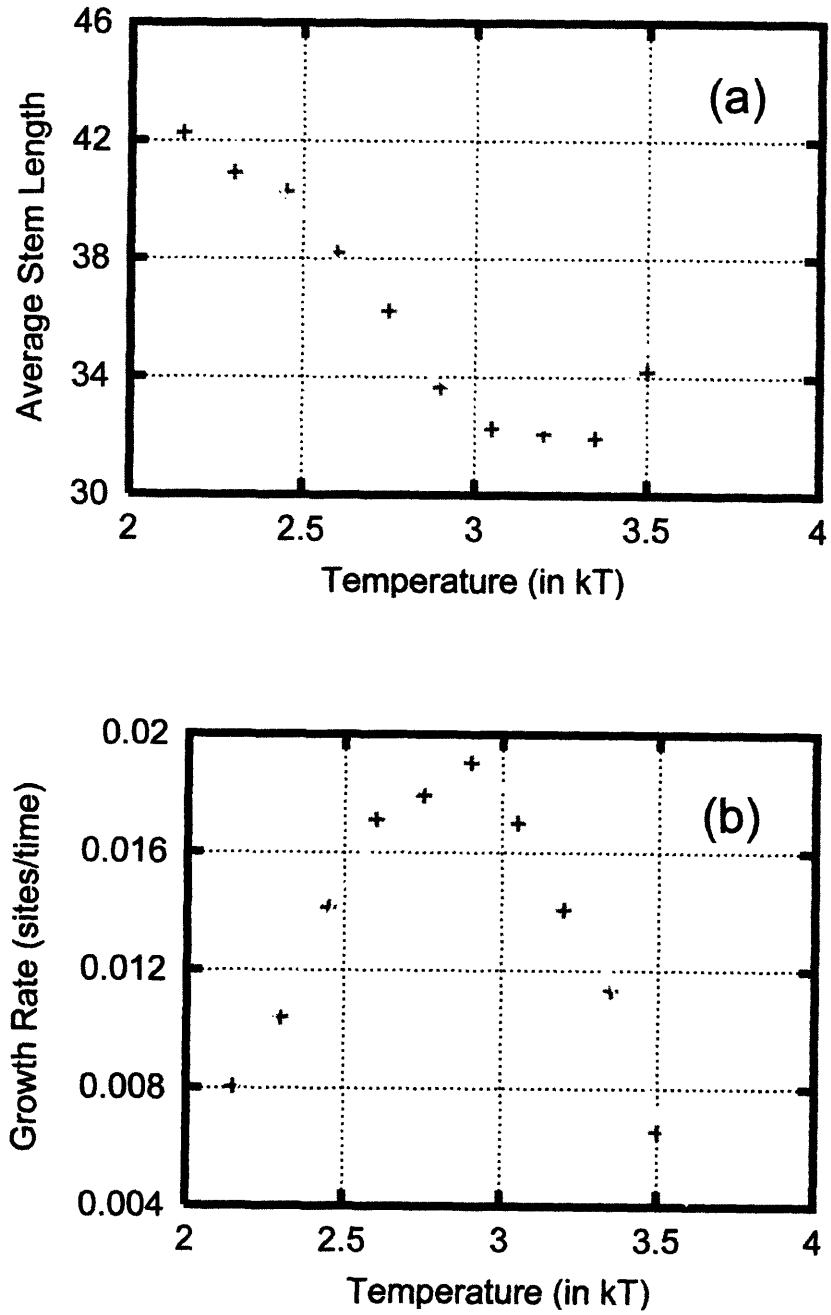

Figure 8.6 Validation of method by comparison of two-dimensional results (+) to work of Doye and Frenkel (gray line), for a single chain crystallizing on an infinite surface. (a) Average stem length as a function of temperature. (b) Growth rate as a function of temperature.

maximum, addition is no longer allowed, but removal can occur, as long as the chain end is exposed to the melt phase.

The four main parameters (E_{NN}, E_{KINK},C_D,C_{DN}) were studied parametrically in order to determine the effects of the each variable and the best match to molecular dynamics data. Preliminary estimates led us to center the values for the variables around E_{NN} of 0.42 kcal/mol, E_{KINK} of 6. kcal/mol, C_D of 0.38, and C_{DN} of 0.12. The initial guess for nearest neighbor internal energy of 0.42 kcal/mol CH_2 units was approximated based on the heat of fusion value 16.8 kcal/mol for n-eicosane. Each lattice site has four neighbor interactions (excluding along the chain itself), each approximately 0.42 kcal/mol, which are shared between the two atoms in the pair, to yield an overall heat of fusion of 16.8 kcal/mol for the chain of length 20 beads. The nearest neighbor interaction requires a neighboring site to match in conformation, as well as be occupied. If only one of the two faces of the site match, then half a nearest neighbor interaction is awarded. The conformational energy for nucleation is equal to that of two kink sites. The kink energy was estimated at 6 kcal/mol, so that a total fold (consisting of two kinks) would approximate 4 *gauche* bonds, each with a 3 kcal/mol barrier. Initial values for C_D and C_{DN} were unknown and were tested over the entire range of zero to one.

The agreement of the KMC simulations to the MD data was determined by conducting KMC simulations at 250 K, 260 K, 270 K, 280 K, and 290 K. The curves generated were then scaled, using the rate pre-factor k_0, in order to minimize the root-mean-square error between the KMC rates and the rates generated by the empirical best-fit curve to the C20 MD data, given by Eq. (2.1), with the order-based parameters of Table 4.1. Fitting was done by manual iteration based on observation of the root-mean

square error. First C_D and C_{DN} were varied to find the best fit at a given E_{KINK} and E_{NN}. Then E_{KINK} was varied and the fitting of C_D and C_{DN} conducted again. This process was repeated until the best value for E_{KINK} was found. Lastly, E_{NN} was varied and the process repeated again.

The fitting of these values proved to be sensitive and complicated. However, some guidelines were determined based on observed behavior of several simulations. First, it is important to note that the nucleation rate must be much smaller than the other rates because there are many more sites on which nucleation can occur. The other moves may only take place at active sites, which are scarce, while nucleation can occur on the inactive sites that are created by crystal growth. In addition, the crystal grows only when the rate of desorption is much faster than the rate of nucleation. This condition prevents the filling of the surface with nuclei incapable of growth because of competition between nuclei, which yields a system incapable of further growth. In addition, the rates of growth and removal should be much faster than the nucleation rate, but still smaller than the rate of desorption. This prevents a system that grows at every new nucleated site, which leads to short segments of growing chain but prevents full extension and further growth. In order to yield a moving growth front of extended chains, these guidelines were necessary, such that generally $k_{desorption} > k_{addition} > k_{removal} > k_{nucleation}$. In addition, the C20 molecular dynamics data imposes additional constraints on the rates, such that the maximum rate is observed around 260-270 K. This criterion is also very dependent on the magnitude of the four parameters mentioned, and especially sensitive to the conformational barrier to nucleation, which is twice the value of E_{KINK}. Therefore, we attempted to vary the position of the maximum mainly by varying the kink energy, while trying to find the

appropriate relative rates for moves using C_D and C_{DN}. This initial set of parameters, determined by manually iterating the process to find the parameters using the method described above, is shown as Run 1 in Table 8.1. The pre-factor k_0^* that yielded the best fit curve had a value of 5.93×10^3 m/s.

Once we had found the region of parameter space where growth occurs and exhibits a maximum in rate as a function of temperature, the region of parameter space surrounding this set was studied thoroughly by conducting simulations with the parameters specified in Table 8.1. Crystal growth rates were computed by dividing the number of beads crystallized by the time required, when the maximum number of layers of 40 has been reached. For each set of parameters, ten simulations were conducted using different seeds for the random number generator, and the ten values for the growth rate were averaged. Table 8.1 also gives the aggregate root-mean-square error, over all five temperature data points, calculated as the difference between the average rate given by the ten simulations at that temperature and the corresponding MD result. The rms error was calculated based on the pre-factor k_0^* that yielded the best fit in Run 1. Figure 8.7 shows the effect of variation of the parameter values on the magnitude of the linear growth rates and the location of the rate maximum. The effect of changing the nearest neighbor energy is shown in Fig. 8.7(a), using Runs 1, 2 and 3. A decrease in the nearest neighbor energy leads to a decrease on the left side of the temperature dependence curve; the right side is not significantly affected by the change. Increasing the nearest neighbor energy in this range increases the growth rates at low temperature slightly, but tests of several values indicate that increasing the nearest neighbor energy has only a small effect, as a limiting curve is reached, near the Run 3 curve. The temperature at which the

Table 8.1 Values of variables for parametric studies. Values are in kcal/mol, except C_D and C_{DN} which are unitless. Values for $\Delta A_{i\to j}$ and E_D are given for a typical addition move with one neighbor, and a nucleation move with no neighbors, both at 270 K. The rms error given is the error computed from the difference between the average rates over ten simulations conducted at each temperature (250 K, 260 K, 270 K, 280 K, 290 K), and the corresponding data from molecular dynamics, shown in Fig. 8.7.

Run	E_{NN}	E_{KINK}	C_D	C_{DN}	Addition		Nucleation		*Rms* error
					$\Delta A_{i\to j}$	E_D	$\Delta A_{i\to j}$	E_D	
1	0.42	6.	0.38	0.12	-0.0845	3.21	2.41	0.385	0.0127
2	0.39	6.	0.38	0.12	-0.0684	3.21	2.41	0.385	0.0368
3	0.50	6.	0.38	0.12	-0.1609	3.21	2.41	0.385	0.0448
4	0.42	5.5	0.38	0.12	-0.0845	3.21	2.21	0.385	0.3640
5	0.42	6.5	0.38	0.12	-0.0845	3.21	3.62	0.385	0.2888
6	0.42	6.	0.35	0.12	-0.0845	2.96	2.41	0.356	2.594
7	0.42	6.	0.41	0.12	-0.0845	3.46	2.41	0.416	0.9050
8	0.42	6.	0.38	0.012	-0.0845	3.21	2.41	0.039	0.0219
9	0.42	6.	0.38	0.5	-0.0845	3.21	2.41	1.605	0.2261

(a)

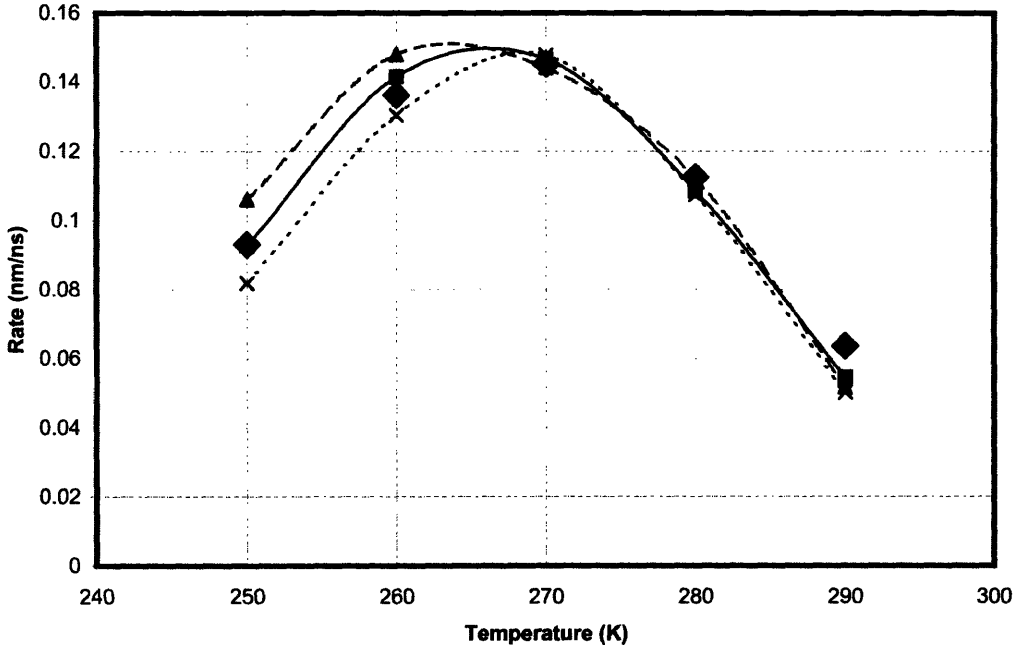

(b)

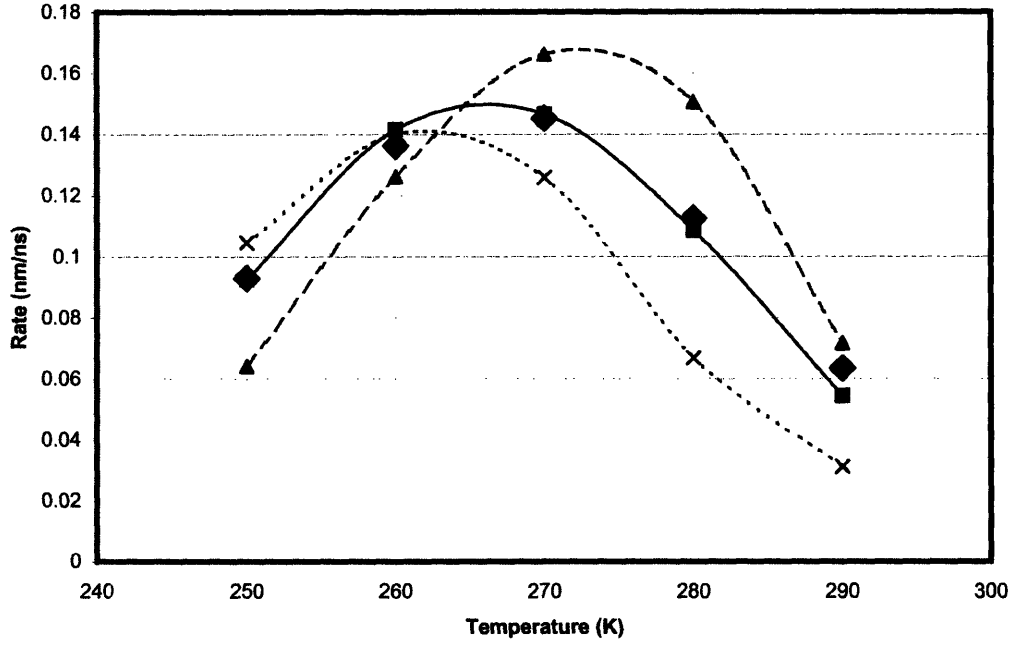

Figure 8.7 Effects of variation of energy barriers on the growth rate curve, according to Table 8.1, with data from fitted equation shown (♦). (a) Effect of changing the nearest neighbor energy using runs 1 (solid line), 2 (dotted line), and 3 (dashed line). (b) Effect of changing the nucleation conformational barrier using runs 1 (solid line), 4 (dotted line), and 5 (dashed line). (continued) [see Table 8.1 for parameters used in each run]

(c)

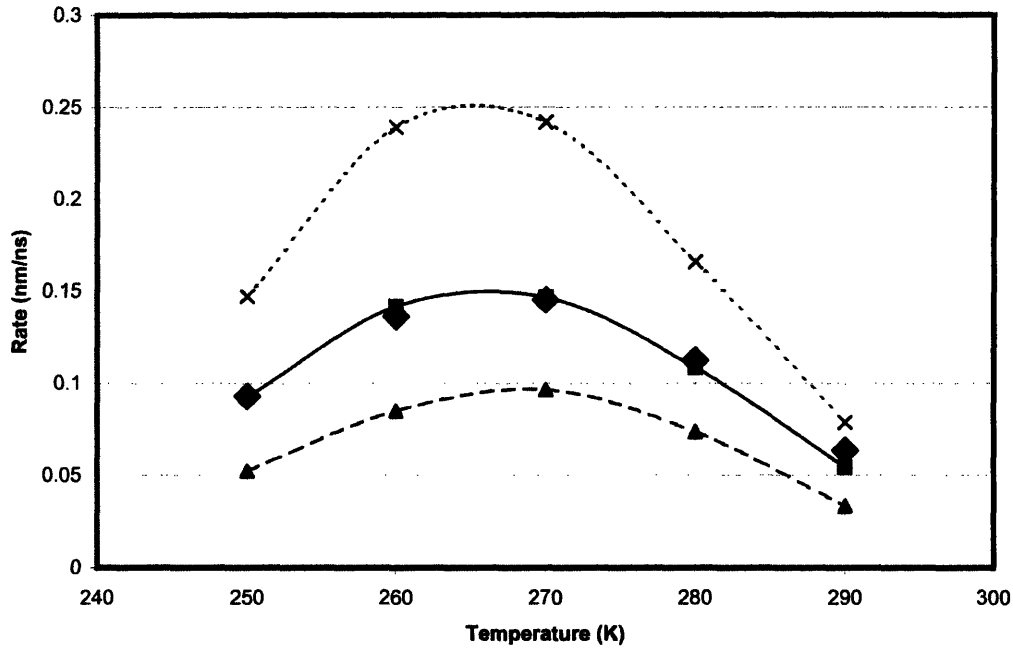

(d)

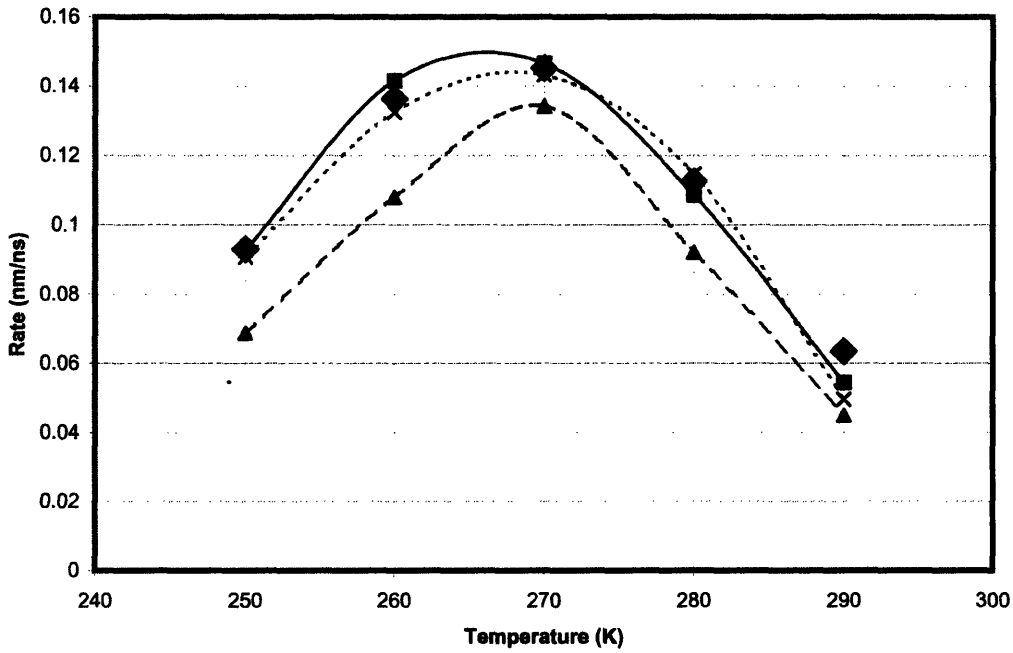

Figure 8.7 Effects of variation of energy barriers on the growth rate curve, according to Table 8.1, with data from fitted equation shown (♦). (c) Effect of changing the growth diffusive barrier using runs 1 (solid line),6 (dotted line), and 7 (dashed line). (d) Effect of changing the nucleation diffusive barrier using runs 1 (solid line), 8 (dotted line), and 9 (dashed line). [see Table 8.1 for parameters used in each run]

maximum occurs shifts slightly towards T_m as the nearest neighbor strength decreases. The effect of changing the magnitude of the nucleation conformational barrier is shown in Fig. 8.7(b), using Runs 1, 4, and 5. Increasing the nucleation conformational barrier shifts the maximum towards T_m, and increases the overall growth rates slightly. The effect of changing the diffusive barrier for growth and removal is shown in Fig. 8.7(c). An increase in the melt mobility barrier causes an increase in rates at all temperatures proportionally. Figure 8.7(d) shows the effect of changing the melt mobility barrier for nucleation. Small changes in this value did not yield any appreciable change in this value. Again, there appears to be a limiting curve that is approached as the parameter approaches zero, which corresponds to the most consistent curvature across the temperature range. For large values of the parameter, as in Run 9, the curvature of the curve is dampened, and restricted to the maximum itself.

To determine the effect temperature has on the *mechanism* of growth, we can study the rates of the individual moves that are occurring in the system. The rates of occurrence of the four moves are shown in Fig. 8.8(a). The rates of all moves increase monotonically with temperature. Fast rates at higher temperature yield a more orderly growth front, where short stems are constantly growing and being removed, leading to a more thermodynamically favorable final structure. At low temperatures, the growth front is more dependent on the stochastic events of the simulation, as is suggested by the highly temperature-dependent mobility term that was parameterized in Chapter 6. While "mistakes" in chain placement interfering with growth are less likely to occur at low temperature, they are much more difficult to reverse. Nucleation is the most common

(a)

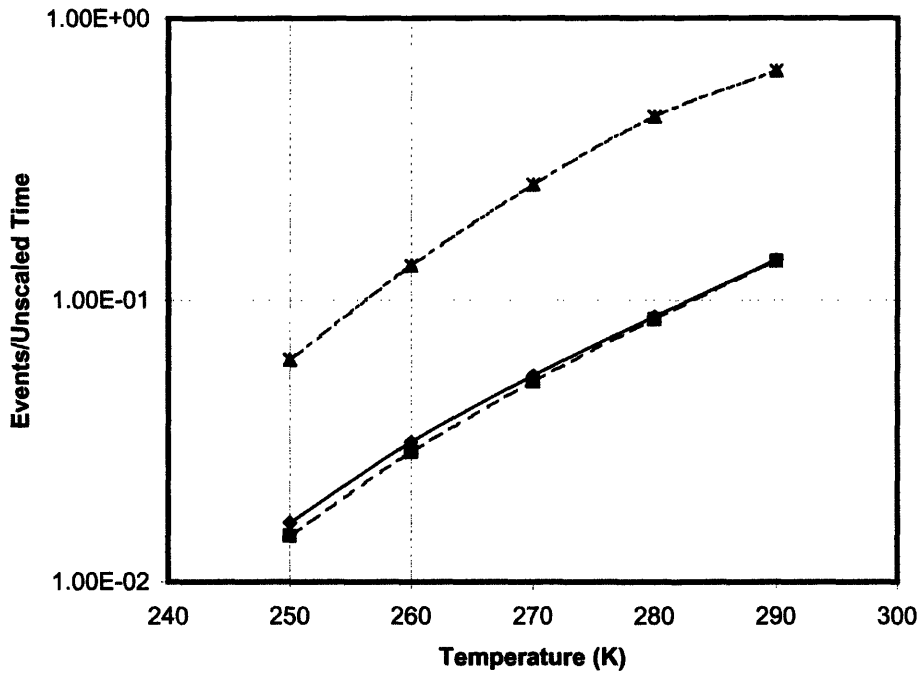

(b)

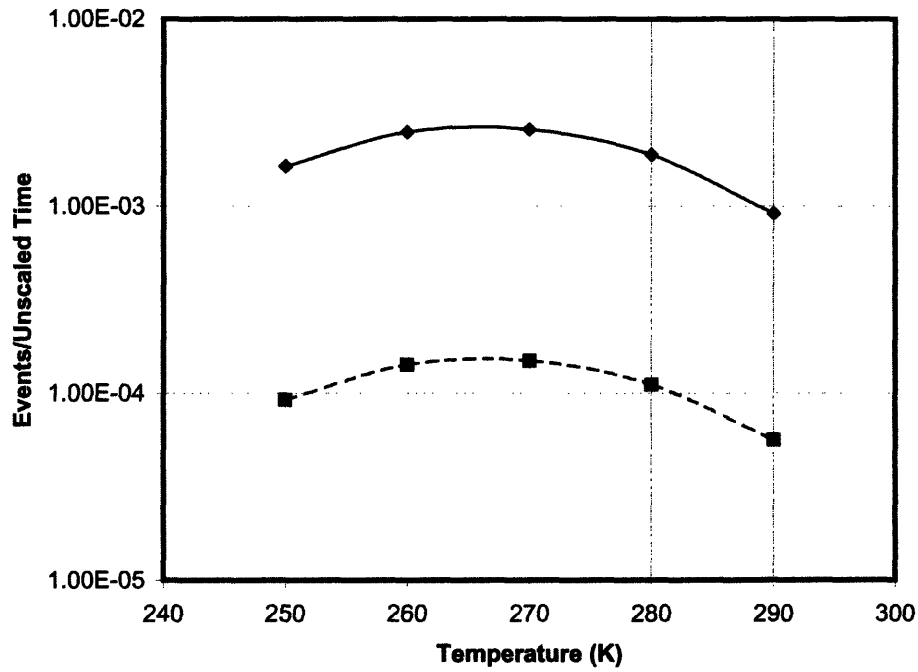

Figure 8.8 Relative rates of occurrence of events as a function of temperature. (a) Rates of the individual moves; addition (solid line), removal (dashed line), nucleation (dotted line), desorption (dotted-dashed line).(On the scale of this plot, the nucleation and desorption rates nearly overlap.) (b) Net rates for events; addition/removal (solid) and nucleation/desorption (dashed).

move, but coupled with the high rate of desorption, the availability of nuclei is the limiting condition for growth. The net rates of addition/removal and nucleation/desorption are shown in Fig. 8.8(b). The net rate for growth was the addition rate minus the removal rate, and the net rate for nucleation was the nucleation rate minus the desorption rate. In this graph, the maximum that occurs in the net rate can be seen more clearly. The net addition/removal rate tracks the net nucleation/desorption rate, as this is the limiting step in growth. This suggests that the mechanism for growth is dominated by secondary nucleation.

8.4 Proof-of-Concept: Polymer Crystallization

A kinetic Monte Carlo algorithm should be able to generate any possible polymer crystal structure, but should predict the correct one, based on accurate values for the rates of the elementary moves. There are three popular structures for melt-crystallized polymer crystals that have been considered in the literature, as discussed in Chapter 2. The main difference between them is in the approach to chain folding. One suggested phenomenon is that of tight folding, or "adjacent re-entry," where a chain stem crystallizes in a lamella of a certain thickness by repeatedly folding into an adjacent lattice position. Another suggestion, made because of the high energy associated with tight folds, is that polymers could crystallize in the same lamellar structure, with non-adjacent re-entry into the crystal. This idea, suggested by Flory, is called a "switchboard model" for lamellae, where chains may wander into the melt phase and return into the crystal at distant lattice sites [Flory 1962]. This is an extension to the "fringed micelle"

model of crystallization, where chains do not fold, but connect to the melt phase that cannot crystallize more material, due to entanglements. In addition, at the growth front, growth may be occurring at a certain lamellar thickness for kinetic reasons, but the lamella may be thickening gradually by another mechanism. Our MD simulation results in Chapter 5 have suggested that surface nucleation during melt crystallization may create short stems that are not connected by folding, but reach equilibrium length in a process independent of lateral growth of the crystal. The recent proposal of Strobl, that crystallization occurs by formation of a mesomorphic layer near the crystal surface, is also consistent with this type of structure [Strobl 2000]. Therefore, a "no-folds" outcome should be a possibility in the model as well. However, previous KMC attempts at melt concentration only rely on the possibility of adjacent re-entry. Finally, we would like to include a model which may contain a distribution of adjacent and non-adjacent folds. As we mentioned in Chapter 2, simulation results have shown that non-adjacent folding may be the most energetically favorable way to dissipate order and density in the interphase region between the melt and the crystal [Mansfield 1983; Balijepalli and Rutledge 1998; Gautam et al. 2000]. However, these simulations have sometimes observed the occurrence of adjacent re-entry as well. Therefore, one "mixed" model of crystal growth should allow for the occurrence of both phenomena.

There are some more complex events that have been observed or suggested, which should be included to allow for ripening behind the growth front. The two moves that we need to make our system comparable to observed C50 and C100 MD systems discussed in Chapter 5 are shown in Fig. 8.9. One move is an 'escape-to-melt' move, shown in Fig. 8.9(a), which accounts for connectivity to the melt phase through the

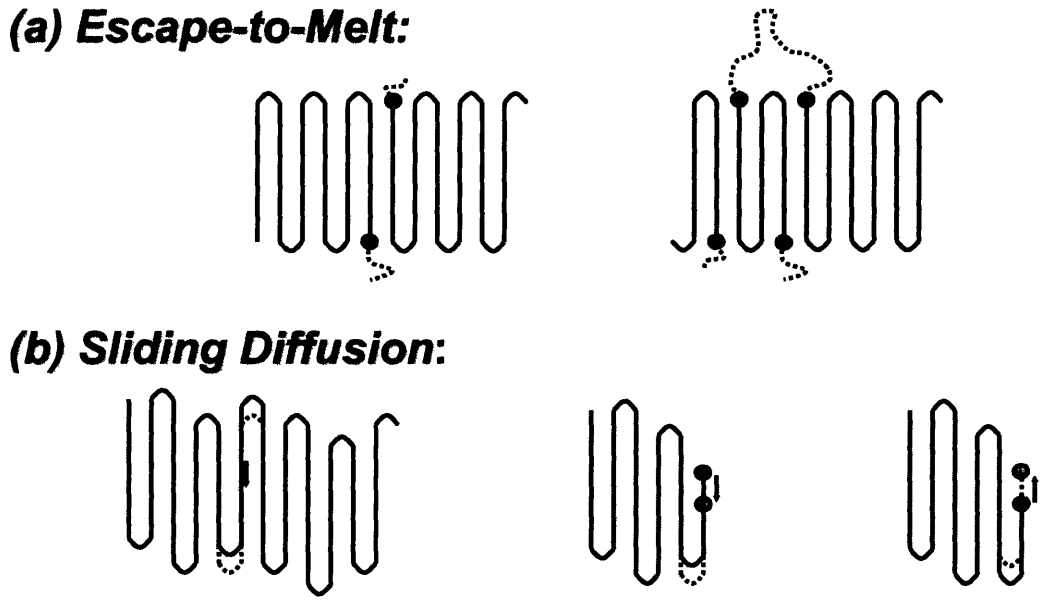

Figure 8.9 Illustration of complex moves that do not affect growth rate, but affect the transition from a growth face to the final structure. (a) Escape-to-melt move allows connectivity between the crystal and melt through the fold surface by converting an active site to an inactive escape site. (b) Sliding diffusion move allows for equilibration of the roughness in the lamellar thickness.

crystal fold surface. This allows for the phenomenon of loose folding or non-adjacent re-entry. This state represents any chain that takes on an amorphous conformation and accounts for the case where a chain exits the crystal, takes on an amorphous conformation, and returns later to the crystal, or the case when a chain exits the crystal and ends in the amorphous phase. However, the identity of the chain is lost when it enters the melt, such that one cannot assess the length of such loops or the connectivity of re-entry points in the fold surface. Because active sites on the fold surface are also capable of capturing this phenomenon, this move is not a requirement for the simulation to be accurate. Rather, it is expedient for accounting purposes, to eliminate the need of keeping track of active sites that are unlikely to lead to further growth. Therefore, we provide active sites at the fold surface a finite probability of being deactivated by conversion to an 'escape-to-melt" site. This move does not effect the nearest neighbor interactions or the conformational energy and is not related to the melt mobility barrier. Therefore, the energy barrier for the escape-to-melt move is assigned a new barrier E_{2MELT}.

Another move that we have observed in MD simulations is that of sliding diffusion of a "stem" or chain segment, shown in Fig. 8.9(b), in which a segment of polymer beads in the crystal slides in a collaborative motion, as observed and discussed in Section 5.2. This is observed in MD runs, as one of the main mechanisms in realizing the equilibrium lamellar thickness, because of the low energy barrier associated with diffusion along the chain axis. The energy barrier for chain sliding is proportional to the number of beads being moved. We allow sliding diffusion to occur for the three cases shown in Fig. 8.9(b). In the first, a chain segment that folds at both ends slides two

lattice sites in either direction. In the second, an active chain end slides two lattice sites pushing a fold back. In the third, an active chain end slides two lattice sites, pull a fold with it. This type of move does not affect the growth rate, but it does control the level of disorder seen in the crystal thickness, which may be different than the disorder that results from the growth process alone. The characterization of the barrier for this move is the same as with the main moves described in Section 8.2. However, the melt mobility barrier used before is now replaced with a barrier to sliding diffusion E_{SLIDE}, which is related to the ability of chains to slide within the crystal.

A second set of simulations were run in order to show that this model is general enough to create different morphologies for melt-crystallized lamella. These simulations are performed using large values for certain energies to prove that the simulation can generate the range of structures shown in Fig. 2.3, in its limiting behavior. Three examples of these simulations are presented here. The moves included in these simulations are addition, removal, nucleation, desorption, sliding diffusion, and escape-to-melt. Because we were not looking at the temperature dependence, we prescribed values for the free energies of each move directly, rather than as a function of temperature. The values for the barrier energies for the different moves are given in Table 8.2. The initial crystal seed is a single layer of 20 x 30 occupied lattice sites in the *xy* plane, isolated on a one of the walls of the the simulation cell comprised of 40 x 60 sites. The growth occurs away from the wall in the positive *z* direction, for up to ten layers. Chain segments are allowed to growth infinitely long. Nucleation moves are assumed to have an activation barrier of 2 E_D, twice that of growth, in the following simulations. Because the runs we present use energies without a temperature

Table 8.2 Values of parameters for examples of different morphologies. The nearest neighbor free energy is given by ΔA_{NN}. For addition and removal moves, conformation energy for kink conformations is ΔA_{KINK}, while for nucleation and desorption moves, the conformational energy for the nucleation and desorption moves are described by ΔA_{NUCL}. All four of these move types have barriers described by E_D, while the mobility barriers for escape-to-melt and sliding diffusion moves are also given. Since we are not interested in temperature dependence at this point, we use free energy differences rather than internal energy differences. Values are in units of kT. The value for the sliding diffusion barrier is for a segment of 20 beads, and is chain length dependent.

Run	Outcome	ΔA_{NN}	ΔA_{KINK}	ΔA_{NUCL}	E_D	E_{2MELT}	E_{SLIDE}
B1	*No-folds*	0.40	4.27	4.27	0.60	0.0	2.67
B2	*Tightly folded*	1.33	1.07	26.7	2.13	3.29	2.67
B3	*Mixed*	1.33	1.60	7.47	2.13	2.13	2.67

dependence, the energies can be scaled to any temperature. We present energies in units of kT.

The morphologies of the three systems are shown in Fig. 8.10. The "no-fold" outcome is shown in Fig. 8.10(a). This is generated by allowing no additional barrier for escape-to-melt moves, and prescribing a high folding energy. Growth occurs by nucleating new chains onto the surface, resulting in multiple layers growing simultaneously. Almost all stems end with an active site for growth or an escape-to-melt site. A tightly folded outcome is shown in Fig 8.10(b). Key features of the energy barriers are a high nearest neighbor energy, a low fold energy, and a high nucleation energy. The structure only has one or two active sites at which growth is taking place. Lattice sites within the layer are filled by folding of the chain into adjacent sites, before growth starts in the next layer. A mixed folding outcome is shown in Fig. 8.10(c). This outcome is a consequence of a high nucleation barrier, and competing fold energy and escape-to-melt energy. This morphology contains several active sites at which growth is taking place. Both adjacent folds are seen, as well as escape-to-melt sites, representing loose folds or chain ends in the melt. Rare nucleation events fill the gaps left by the few nucleating chains. The growth that occurs in these three runs yields differences in structure, as shown in Fig. 8.11. The data was averaged over the stems in each z-layer, for a single simulation and do not yield good statistics, since there are only approximately six stems per layer. Figure 8.11(a) shows the fractional coverage of the initial seed as a function of distance from that seed. Despite the statistical noise, we can see that, for the tightly folded crystal, the subsequent growth cannot fully cover the initial seed. This may be due to the configurational restrictions of single chain growth, which create a stem of

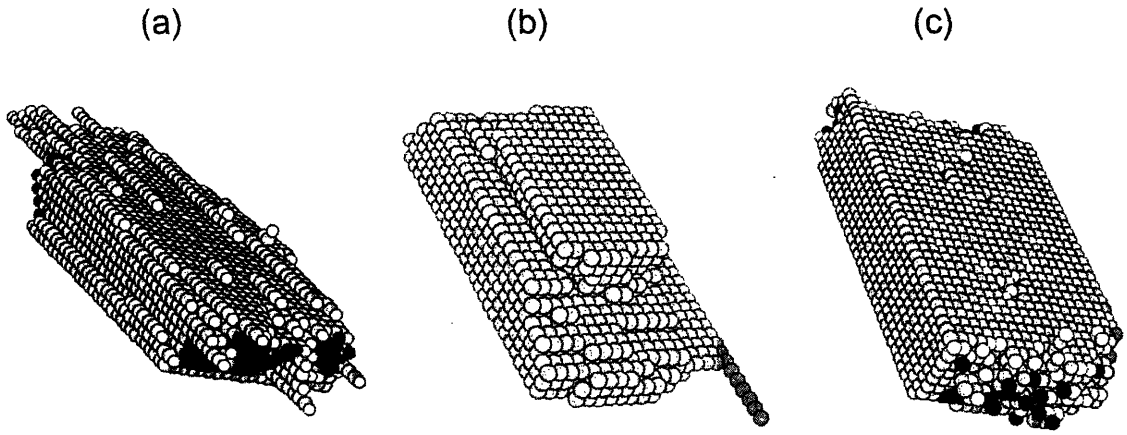

Figure. 8.10 Snapshots of morphologies representing different growth models from Table 8.2. Black beads represent escape-to-melt sites, white beads active sites, and grey beads all other occupied sites. (a) Run B1, No folds. (b) Runs B2, Tightly folded. (c) Run B3, Mixed.

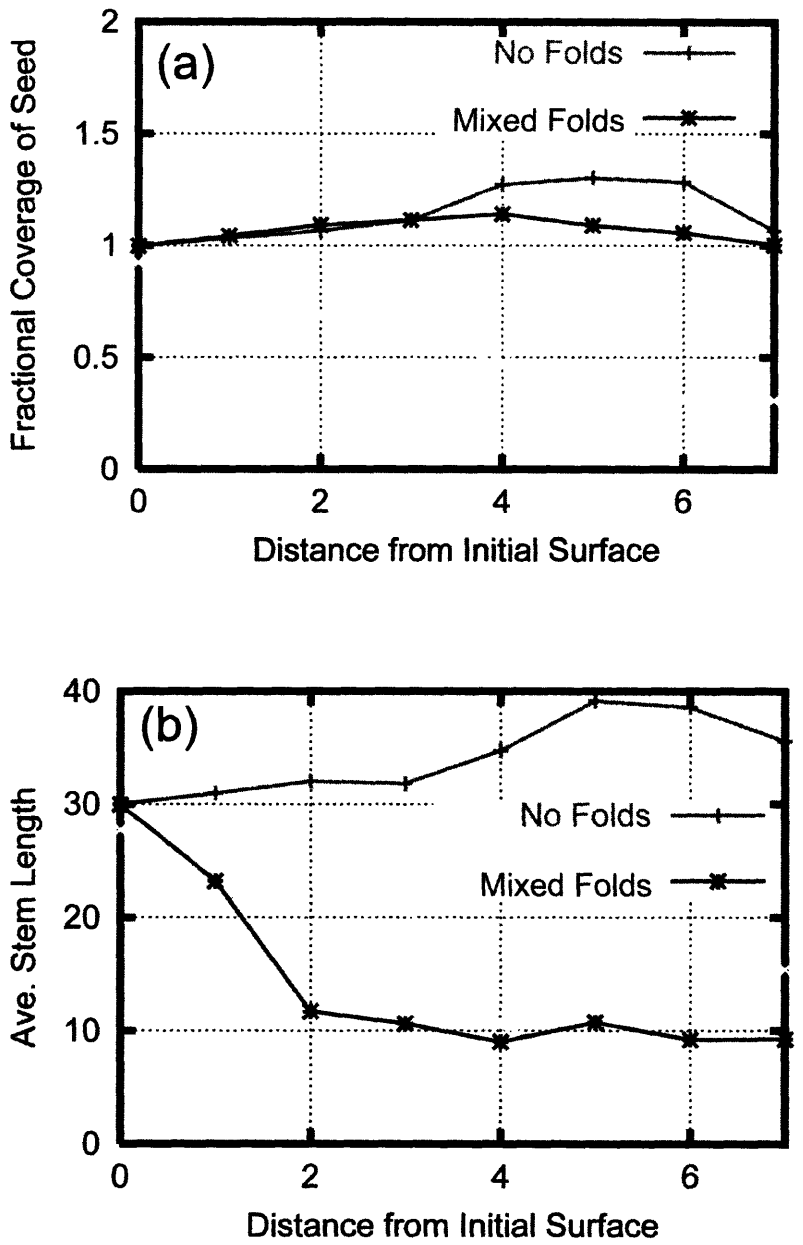

Figure 8.11 Characteristics of growth front as a function of distance from initial seed, for runs in Table 8.2; Runs B1, no folds (+); Run B2, Tightly folded (×); Run B3, Mixed (*). (a) Fractional coverage of the initial seed as a function of distance from the seed. (b) Average stem length, or average number of consecutive straight segments as a function of distance from the initial seed.

equal or less length to the underlying stem. This also may be a consequence of using a strong interaction energy which limits overgrowth of the original seed. However, the stochastic nature of folding allows folds that can occur anywhere on the surface. This characteristic is of more consequence in the three-dimensional system than it is in the two dimensional system of Doye and Frenkel [Doye and Frenkel 1999]. The two dimensional case only allows one direction for the deposition of a new stem, while the three-dimensional case allows stem deposition not only in the direction of growth, but in both lateral directions as well. Therefore, the "fixed point attractor" observed in the two-dimensional case, where a steady-state value of lamellar thickness is achieved, may only be possible in the three dimensional case with particular parameters for the nearest neighbor interaction, the kink energy, and the chain sliding barrier. We did not find a set of parameters like this during the course of our simulations. The "no-folds" outcome allows for full coverage of the initial surface, as does the mixed folds outcome.

Because these morphologies are created from conditions where nucleation is prevalent, they have the ability to fill holes created by stochastic folding and/or nucleation. Therefore, the fixed point attractor is shifted upwards to thicker crystals, compared to the tightly-folded model. When we consider the length of a stem within the crystal, only the "no-fold' model crystallizes in completely extended stems that cover the crystal, as shown in Fig. 8.11(b). The tightly-folded model crystallizes in extended stems that are shorter than the initial seed stems. The mixed folds model, however, uses shorter stems to yield full coverage of the initial crystal, by using a combination of folding, and nucleation of new chains from the melt to fill gaps in the crystal.

The generality of this model suggests that, given the correct values for the rates of these moves, the morphology of the crystal can be an outcome of the model described here, rather than an assumption. Because the model can reproduce different morphologies, it can predict which would be observed for a particular set of parameters. Estimates for accurate energy barriers for most moves can be made based on molecular dynamics, where KMC rates were mapped to molecular dynamics rates. However, for long chains, the energy of the escape-to-melt move will still be unknown. This move attempts to capture not just the transition from crystal to the interphase region, but also the restricting energy that may be present from entanglements of chains in the interphase. This complicates estimates for the energy barrier to this move. However, we recognize that this move is not essential to the simulation, since chains can be left as actively growing chains that do not grow anymore; the move is important as an accounting move only that limits the number of active sites.

Comprehensive simulations mapping the both the temperature and molecular weight effects to KMC parameters should be considered for future work as a second level of validation. Based on our observations from Chapter 5, the parameters generated from the C20 simulations should be adequate to simulation C50, which seems to crystallize by the same mechanism. Using the T_m and T_g for C50 from Table 6.2, we conducted three simulations of C50 at 347 K, the temperature at which the rate maximum is observed, using the KMC parameters generated for C20. The Rouse-based model, shown in Fig. 6.1, yields a crystallization rate of 0.0238 m/s at this temperature. Our KMC simulation results yield an average growth rate of 0.0184 m/s with a standard deviation of 0.0050 m/s. Despite exponential changes in the growth rate as a function of molecular weight,

this result for C50 not only predicts the order of magnitude of the growth rate correctly, but is approximately one standard deviation away from the best-fit curve for the molecular dynamics results. For the case of C100, we believe that the introduction of the sliding diffusion move should allow for duplication of this result as well, once the barrier for sliding diffusion has been properly parameterized. The escape-to-melt move would be important for longer, entangled chains that retain connectivity to the melt through the fold surface for semi-crystalline morphologies.

Chapter 9

Conclusion

9.1 Summary

As was mentioned as a motivation of this work, empirical investigations have been unable to differentiate competing models of crystallization at high undercooling. Furthermore, a phase change model would be beneficial for process simulation, in order to streamline process design. This requires molecular detail to understand the mechanism and rate of crystal phase growth. We have adapted molecular simulation techniques to observe, quantify, and model crystal growth of alkanes and polyethylene, with the best model that today's computational capabilities allowed. The alkane and polyethyelene subgroup was chosen as a prototype for these simulations, and the methods developed here are extensible to other polymers. The findings of this study are summarized below.

(1) We have identified a molecular simulation technique that is capable of modeling the growth rate of alkane systems. This technique is non-equilibrium molecular dynamics in the presence of surface crystals. We have considered the atomistic models for alkanes and polyethylene, and chosen the united atom model, as a compromise between level of

detail and computational speedup. Our atomistic model and simulation setup incorporate first-principles and are based on fundamental scientific knowledge.

(2) We have implemented molecular dynamics simulations, on alkanes of length C20, C50, and C100, to capture the molecular weight and temperature dependence of crystallization rates for the phase change from a confined melt to a hexagonal close-packed crystal structure. We have developed several tools as metrics for crystallization, and quantitative measures of linear growth rates, based on the initial geometry. The ones with the most resolution quantify the increase in local chain order and local density that accompany the phase change, specifically the bond order parameter, based on orientational order, and Voronoi tessellation of space based on atom locations. The rates showed a temperature dependence that followed the Ziabicki empirical model, and parameters for this model have been computed based on molecular considerations. In addition, the growth process for eicosane has been decomposed into elementary ordering and melting processes, which suggests the necessity of a secondary nucleation model that incorporates reversible attachment. For C50 and C100, we have been able to quantify growth rates and make qualitative comments about the likelihood of secondary nucleation mechanisms. We have described our observations about the size and shape of a surface nucleus from molecular simulation for C50 and C100 systems, to aid in the understanding of the mechanisms involved in alkane crystallization. Extrapolations of our results suggest that the growth rate measurements of alkane from molecular dynamics and polyethylene from high speed crystallization converge near the entanglement molecular weight.

(3) We have adapted the best existing models for polymer crystallization to handle the molecular weight dependence of alkane rates. We have constructed an analytical crystallization model that can be parameterized entirely in terms of universal properties of polymer chains described by polymer physics and chemically specific quantities that can be estimated polymer by polymer. Furthermore, we have for the first time parameterized a crystallization model using molecular dynamics simulations. The model predicts crystal growth rates as a function of temperature and molecular weight up to the entanglement molecular weight. The model is broken down into a barrier based on relaxation of the chains in the melt, and the traditional thermodynamic barrier from classical nucleation theory. Error analysis reveals that there is no statistically significant difference between the Rouse-based model and a reptation-based model, but the thermodynamic parameters for the Rouse-based model are to be closer to those measured empirically.

(4) We have shown how the crystal growth rate model for alkanes obtained from molecular dynamics simulations can be extended for use with entangled polymers as well, by linking the relaxation associated with crystallization to the local relaxation of an entangled segment. We validate this approach using theory, our simulations, and recent experimental data for polyethylene crystal growth. We have generated one set of parameters that are strictly characteristic of chemistry and valid for any molecular weight and temperature in which Regime III crystal growth occurs. This model can now be applied to quantify polyethylene crystallization rates using Schneider's rate equations, to

infer how small changes in the processing conditions can yield large differences in the final properties, as we have suggested in a sample problem. This type of equation, which quantifies the effects of molecular weight and temperature independently, can be even more useful for materials in more complex processing conditions, such as reaction spinning or reactive injection molding, where the molecular weight is a process variable that can also be controlled.

(5) We have developed a general KMC algorithm for measuring growth of a polymer crystal phase during melt crystallization, based on the algorithm of Bortz *et al.* We have incorporated new moves into a general framework to allow multi-chain, three-dimensional growth and the escape of chains from the crystal to the melt, through the fold surface. By restricting growth to a single chain in two dimensions, we have validated the algorithm against the work of Doye and Frenkel. We performed parametric studies on the melt-crystallization of C20 to study the effects of each energy barrier. In addition, the KMC algorithm allows us to consider the importance of individual moves in contributing to growth. We have shown, as a proof-of-concept, that this algorithm is capable of generating morphologies characteristic of several theories of secondary nucleation in polymer melts.

9.2 Recommendations for Future Work

While this study answers several questions regarding the models of growth of alkane and polymer crystal phases, several new questions have been raised, regarding

ideas for improvement, other applications of the methodology, and old areas of research that could be revisited. From the understanding gained from this research, we propose the following recommendations for subsequent work in this area:

(1) This methodology should be tested for alkane systems of higher molecular weights. Simulating past the entanglement molecular weight was computationally challenging, when this work was initiated. While still challenging, the advent of cheap parallel computing should allow for a small multiplication in the size of the system that can be simulated. However, timescale issues may still remain a problem until computational abilities allow. In addition, if this model is to be relevant to the processing community, growth should be studied under flow conditions. The assumption often made is that nucleation is influenced strongly by flow, but growth is not influenced. Because studies discussed in Chapter 2 suggest that nucleation does not occur until stress is removed from a system, we have also made the assumption that growth is not affected by flow. However, fibril morphologies are created from under different flow conditions, where growth might be occurring simultaneous with flow. Applying molecular dynamics with a directed Langevin thermostat, which adds a uniaxial velocity between the two plates, can give us a molecular window into complex processing conditions, and allow us to determine concretely the effects of flow on crystal growth.

(2) Further work, both experimental and simulation should be conducted for polyethylene systems near the entanglement molecular weight. More data in this area will give us a better understanding of how entanglements affect crystallizing polymeric

systems. Our hypothesis on why the molecular weight dependence of growth rates changes at the crossover from alkanes to polyethylene can explain both current experimental and simulation data, but requires revisiting this old field of measuring growth rates, using new available techniques. New techniques for measurements of high speed crystallization rates may be applied to chains that are below or near the entanglement length. While rates for polymer crystallization have already been observed, measurements of alkane rates can provide information that can verify the origin of the behavior that we are suggesting.

Simulations can also be conducted on the fold surface. The MD techniques we have used may be applied to study the fold surface and interphase region between lamellae. Currently, our research group has the capability to create equilibrated melt-crystal interfaces at the fold surface, through Monte Carlo techniques. Performing molecular dynamics on such a system may reveal the rates and mechanisms of lamellar thickening, and give us a molecular understanding of what limits lamellar growth.

(3) This methodology and model should be tested on a more complex polymer. Polyethylene was explored as a prototype for more complex materials. Forcefields for polypropylene are the same as polyethylene, though the crystal structure is much more complex. This pursuit would require the generalization of crystallization metric algorithms that can differentiate between crystal and amorphous phase. This endeavor in itself is a large project. It would be of interest to develop a tool that can systematically create a metric for differentiating regions of crystal and amorphous phases, based on the crystalline conformer.

In addition, developing a similar rate model for polypropylene would be the first step towards understand how the material-specific parameters are affected by the chemical species, in order to determine a predictive growth model based on the chemistry of the repeat unit. This would be an important step towards developing the molecular-level framework for use in the multiscale predictive modeling of fiber and film processing.

(4) Finally, the Kinetic Monte Carlo methodology should be further tested for crystal growth systems to be able to match the rates of MD to the rates of KMC. If this system can be parameterized from a few alkane systems of varying molecular weight, then it may be useful as a speedup for studying entangled systems as they crystallize. This would aid the study of the nature of the growth face, the mechanism by which crystal thickening occurs after the growth front has moved away. Once this calibration step has occurred, a verified set of parameters required for simulation of long polymer chains will exist, which will allow the study of polymer lamellar growth.

Further refinements of the code should also be conducted to make study the growth on three-dimensional nuclei. Currently the systems allow for growth in the z direction, but a search algorithm should be implemented to find nucleation and growth sites in all directions, such that the study of single crystal growth in three dimensions can be done. Furthermore, the KMC algorithm is also applicable to the study of nucleation of a crystal polymer phase, with minor modifications. This would require allowing nucleation to occur between any two empty sites, and growth to occur in three dimensions, as mentioned above. This is a problem that involves very rare events for a

molecular dynamics simulation, but may be tractable for KMC. A debate is occurring regarding whether polymers crystallize by spinodal decomposition or classical nucleation and growth. KMC should be able to provide insight into this issue. This implementation has a general framework that could provide much insight into both crystallization and melting phenomena.

Chapter 10

Bibliography

Alamo, R. G.,Mandelkern, L.,Stack, G. M.,Krohnke, C.,Wegner, G. "Crystallization Kinetics of Long-Chain N-Alkanes from the Melt and from Solution." *Macromolecules* **1994**, 27(1): 147-156.

Al-Hussein, M.,Davies, G. R.,Ward, I. M. "Mechanical properties of oriented low-density polyethylene with an oriented lamellar-stack morphology." *Journal of Polymer Science Part B-Polymer Physics* **2000**, 38(5): 755-764.

Allen, M. P.,Tildesley, D. J. *Computer Simulations of Liquids* Oxford University Press: New York, 1987.

Armistead, J. P.,Hoffman, J. D. "Direct evidence of regimes I, II, and III in linear polyethylene fractions as revealed by spherulite growth rates." *Macromolecules* **2002**, 35(10): 3895-3913.

Armistead, K.,Goldbeckwood, G.,Keller, A. "Polymer Crystallization Theories." *Advances in Polymer Science* **1992**, 100: 221-312.

Avrami, M. *Journal of Chemical Physics* **1940**, 8: 212.

Balijepalli, S.,Rutledge, G. C. "Molecular simulation of the intercrystalline phase of chain molecules." *Journal of Chemical Physics* **1998**, 109(16): 6523-6526.

Balijepalli, S.,Rutledge, G. C. "Conformational statistics of polymer chains in the interphase of semi-crystalline polymers." *Computational and Theoretical Polymer Science* **2000**, 10(1-2): 103-113.

Bassett, D. C.,Frank, F. C.,Keller, A. *Nature* **1959**, 184: 810.

Bassett, D. C.,Olley, R. H.,Alraheil, I. A. M. "On Isolated Lamellae of Melt-Crystallized Polyethylene." *Polymer* **1988**, 29(9): 1539-1543.

Berendsen, H. J. C.,Postma, J. P. M.,Van Gunsteren, W. F.,Dinola, A.,Haak, J. R. "Molecular-Dynamics with Coupling to an External Bath." *Journal of Chemical Physics* **1984**, 81(8): 3684-3690.

Binsbergen, F. L. "A reconsideration fo polymer crystallization theory." *Kolloid Zeitscrift* **1970**, 237: 389-395.

Blundell, D. J.,Mahendrasingam, A.,Martin, C.,Fuller, W.,MacKerron, D. H.,Harvie, J. L.,Oldman, R. J.,Riekel, C. "Orientation prior to crystallisation during drawing of poly(ethylene terephthalate)." *Polymer* **2000**, 41(21): 7793-7802.

Bolton, K.,Bosio, S. B. M.,Hase, W. L.,Schneider, W. F.,Hass, K. C. "Comparison of explicit and united atom models for alkane chains physisorbed on alpha-Al2O3 (0001)." *Journal of Physical Chemistry B* **1999**, 103(19): 3885-3895.

Bortz, A. B.,Kalos, M. H.,Lebowitz, J. L. "New Algorithm for Monte-Carlo Simulation of Ising Spin Systems." *Journal of Computational Physics* **1975**, 17(1): 10-18.

Bruno, J. A. O.,Allan, N. L.,Barron, T. H. K.,Turner, A. D. "Thermal expansion of polymers: Mechanisms in orthorhombic polyethylene." *Physical Review B-Condensed Matter* **1998**, 58(13): 8416-8427.

Cai, W.,Bulatov, V. V.,Yip, S. "Kinetic Monte Carlo method for dislocation glide in silicon." *Journal of Computer-Aided Materials Design* **1999**, 6(2-3): 175-183.

Capaldi, F. M.,Boyce, M. C.,Rutledge, G. C. "Molecular response of a glassy polymer to active deformation." *Polymer* **2004**, 45(4): 1391-1399.

Carmesin, I.,Kremer, K. "The Bond Fluctuation Method - a New Effective Algorithm for the Dynamics of Polymers in All Spatial Dimensions." *Macromolecules* **1988**, 21(9): 2819-2823.

Chen, C. M.,Higgs, P. G. "Monte-Carlo simulations of polymer crystallization in dilute solution." *Journal of Chemical Physics* **1998**, 108(10): 4305-4314.

Cheng, S. Z. D.,Chen, J. H.,Barley, J. S.,Zhang, A. Q.,Habenschuss, A.,Zschack, P. R. "Isothermal Thickening and Thinning Processes in Low-Molecular-Weight Poly(Ethylene Oxide) Fractions Crystallized from the Melt .3. Molecular-Weight Dependence." *Macromolecules* **1992**, 25(5): 1453-1460.

Davis, G. T.,Eby, R. K. "Glass Transition of Polyethylene - Volume Relaxation." *Journal of Applied Physics* **1973**, 44(10): 4274-4281.

Davis, G. T.,Eby, R. K.,Colson, J. P. "Thermal Expansion of Polyethylene Unit Cell: Effect of Lamella Thickness." *Journal of Applied Physics* **1970**, 41(11): 4316-4326.

Degennes, P. G. "Polymer-Solutions near an Interface .1. Adsorption and Depletion Layers." *Macromolecules* **1981**, 14(6): 1637-1644.

Doufas, A. K.,McHugh, A. J.,Miller, C.,Immaneni, A. "Simulation of melt spinning including flow-induced crystallization - Part II. Quantitative comparisons with industrial spinline data." *Journal of Non-Newtonian Fluid Mechanics* **2000**, 92(1): 81-103.

Doye, J. P. K.,Frenkel, D. "Crystallization of a polymer on a surface." *Journal of Chemical Physics* **1998**, 109(22): 10033-10041.

Doye, J. P. K.,Frenkel, D. "Kinetic Monte Carlo simulations of the growth of polymer crystals." *Journal of Chemical Physics* **1999**, 110(5): 2692-2702.

Eder, G.,Janeschitz-Kriegl, H.,Liedauer, S. "Crystallization Processes in Quiescent and Moving Polymer Melts under Heat-Transfer Conditions." *Progress in Polymer Science* **1990**, 15(4): 629-714.

Eisenriegler, E.,Kremer, K.,Binder, K. "Adsorption of polymer chains at surfaces: scaling and Monte Carlo analysis." *Journal of Chemical Physics* **1982**, 77(12): 6296-6320.

Ermak, D. L.,McCammon, J. A. "Brownian Dynamics with hydrodynamic interactions." *Journal of Chemical Physics* **1978**, 69(4): 1352-1360.

Esselink, K.,Hilbers, P. A. J.,Vanbeest, B. W. H. "Molecular-Dynamics Study of Nucleation and Melting of N-Alkanes." *Journal of Chemical Physics* **1994**, 101(10): 9033-9041.

Ferry, J. D. *Viscoelastic poperties of polymers* WIley: New York, 1970.

Fichthorn, K. A.,Weinberg, W. H. "Theoretical Foundations of Dynamic Monte-Carlo Simulations." *Journal of Chemical Physics* **1991**, 95(2): 1090-1096.

Flory, P. J. "On the Morphology of the Crystalline State in Polymers." *Journal of the American Chemical Society* **1962**, 84: 2857-2867.

Fox, T. G.,Loshaek, S. "Influence of Molecular Weight and Degree of Crosslinking on the Specific Volume and Glass Temperature of Polymers." *Journal of Polymer Science* **1955**, 15: 371-384.

Fujiwara, S.,Sato, T. "Molecular dynamics simulation of structural formation of short polymer chains." *Physical Review Letters* **1998**, 80(5): 991-994.

Fujiwara, S.,Sato, T. "Molecular dynamics simulation of structure formation of short chain molecules." *Journal of Chemical Physics* **1999**, 110(19): 9757-9764.

Gandica, A.,Magill, J. H. "A universal relationship for the crystallization kinetics of polymeric materials." *Polymer* **1972**, 13: 595-596.

Gautam, S.,Balijepalli, S.,Rutledge, G. C. "Molecular simulations df the interlamellar phase in polymers: Effect of chain tilt." *Macromolecules* **2000**, 33(24): 9136-9145.

Gee, R. H.,Boyd, R. H. "The role of the torsional potential in relaxation dynamics: a molecular dynamics study of polyethylene." *Computational and Theoretical Polymer Science* **1998**, 8(1-2): 93-98.

Gerstein, M.,Tsai, J.,Levitt, M. "The Volume of Atoms on the Protein Surface: Calculated from Simulation, using Voronoi Polyhedra." *Journal of Molecular Biology* **1995**, 249: 955-966.

Gibbs, J. W. *The Collected Works of J. Willard Gibbs* Yale Univ. Press: New Haven, 1948.

Goldbeck-Wood, G. "Simulation of polymer crystallization kinetics with the Sadler/Gilmer model." *Polymer* **1990**, 31: 586.

Goldbeck-Wood, G. "Polymer crystallization: Simulation with entropic barrier model and application to specific polymers." *Macromolecular Symposium* **1994**, 81: 221.

Heck, B.,Hugel, T.,Iijima, M.,Strobl, G. "Steps in the formation of the partially crystalline state." *Polymer* **2000**, 41(25): 8839-8848.

Heeley, E. L.,Maidens, A. V.,Olmsted, P. D.,Bras, W.,Dolbnya, I. P.,Fairclough, J. P. A.,Terrill, N. J.,Ryan, A. J. "Early stages of crystallization in isotactic polypropylene." *Macromolecules* **2003**, 36(10): 3656-3665.

Hikosaka, M.,Amano, K.,Rastogi, S.,Keller, A. "Lamellar thickening growth of an extended chain single crystal of polyethylene .1. Pointers to a new crystallization mechanism of polymers." *Macromolecules* **1997**, 30(7): 2067-2074.

Hikosaka, M.,Amano, K.,Rastogi, S.,Keller, A. "Lamellar thickening growth of an extended chain single crystal of polyethylene (II) : Delta T dependence of lamellar thickening growth rate and comparison with lamellar thickening." *Journal of Materials Science* **2000**, 35(20): 5157-5168.

Hobbs, J. K.,Humphris, A. D. L.,Miles, M. J. "In-situ atomic force microscopy of polyethylene crystallization. 1. Crystallization from an oriented backbone." *Macromolecules* **2001**, 34(16): 5508-5519.

Hocquet, S.,Dosiere, M.,Tanzawa, Y.,Koch, M. H. J. "Lamellar and crystalline layer thickness of single crystals of narrow molecular weight fractions of linear polyethylene." *Macromolecules* **2002**, 35(13): 5025-5033.

Hoffman, J. D. "Role of Reptation in the Rate of Crystallization of Polyethylene Fractions from the Melt." *Polymer* **1982**, 23(5): 656-670.

Hoffman, J. D.,Frolen, L. J.,Ross, G. S.,Lauritzen, J. I. "Growth-Rate of Spherulites and Axialites from Melt in Polyethylene Fractions - Regime-1 and Regime-2 Crystallization." *Journal of Research of the National Bureau of Standards Section a-Physics and Chemistry* **1975**, 79(6): 671-699.

Hoffman, J. D.,Miller, R. L. "Kinetics of crystallization from the melt and chain folding in polyethylene fractions revisited: Theory and experiment." *Polymer* **1997**, 38(13): 3151-3212.

Hoffman, J. D.,Weeks, J. J. "Rate of Spherultic Crystallization with Chain Folds in Polychlorotrifluoroethylene." *Journal of Chemical Physics* **1962**, 37(8): 1723-1741.

Hosier, I. L.,Bassett, D. C. "A study of the morphologies and growth kinetics of three monodisperse n-alkanes: C122H246, C162H326 and C246H494." *Polymer* **2000**, 41(25): 8801-8812.

Hosier, I. L.,Bassett, D. C.,Moneva, I. T. "On the Morphology of Polyethylene Crystallized from a Sheared Melt." *Polymer* **1995**, 36(22): 4197-4202.

Hu, W. B.,Frenkel, D.,Mathot, V. B. F. "Intramolecular nucleation model for polymer crystallization." *Macromolecules* **2003**, 36(21): 8178-8183.

Hu, W. B.,Frenkel, D.,Mathot, V. B. F. "Sectorization of a lamellar polymer crystal studied by dynamic Monte Carlo simulations." *Macromolecules* **2003**, 36(3): 549-552.

Huetter, M.,Rutledge, G. C.,Armstrong, R. C. *In Press*.

Imai, M.,Kaji, K.,Kanaya, T. "Structural Formation of Poly(Ethylene-Terephthalate) During the Induction Period of Crystallization .3. Evolution of Density- Fluctuations to Lamellar Crystal." *Macromolecules* **1994**, 27(24): 7103-7108.

Iwata, M.,Sato, H. "Chain movement in crystallization process by molecular dynamics simulation." *Physical Chemistry Chemical Physics* **1999**, 1(10): 2491-2500.

Kanig, G. "Further Electron-Microscope Observations On Polyethylene .3. Smectic Intermediate State During Melting and Crystallization." *Colloid and Polymer Science* **1991**, 269: 1118-1125.

Karasawa, N.,Dasgupta, S.,Goddard, W. A. "Mechanical-Properties and Force-Field Parameters for Polyethylene Crystal." *Journal of Physical Chemistry* **1991**, 95(6): 2260-2272.

Kavassalis, T. A.,Sundararajan, P. R. "A Molecular-Dynamics Study of Polyethylene Crystallization." *Macromolecules* **1993**, 26(16): 4144-4150.

Keith, H. D. *Journal of Applied Physics* **1964**, 35: 3115-3126.

Keller, A. *Journal of Polymer Science* **1955**, 17: 351-364.

Keller, A.,Hikosaka, M.,Rastogi, S.,Toda, A.,Barham, P. J.,Goldbeckwood, G. "An Approach to the Formation and Growth of New Phases with Application to Polymer Crystallization - Effect of Finite-Size, Metastability, and Ostwald Rule of Stages." *Journal of Materials Science* **1994**, 29(10): 2579-2604.

Ko, M. J.,Waheed, N.,Lavine, M. S.,Rutledge, G. C. "Charaterization of polyethylene crystallization from an oriented melt by molecular dynamics simulation." *Journal of Chemical Physics* **2004**, 121(6): 2823-2832.

Kolb, R.,Seifert, S.,Stribeck, N.,Zachmann, H. G. "Simultaneous measurements of small- and wide-angle X-ray scattering during low speed spinning of poly(propylene) using synchrotron radiation." *Polymer* **2000**, 41(4): 1497-1505.

Koyama, A.,Yamamoto, T.,Fukao, K.,Miyamoto, Y. "Molecular dynamics simulation of polymer crystallization from an oriented amorphous state." *Physical Review E* **2002**, 65(5): Art. No. 050801 Part 050801.

Kraack, H.,Deutsch, M.,Sirota, E. B. "n-alkane homogeneous nucleation: Crossover to polymer behavior." *Macromolecules* **2000**, 33(16): 6174-6184.

Kraack, H.,Sirota, E. B.,Deutsch, M. "Measurements of homogeneous nucleation in normal-alkanes." *Journal of Chemical Physics* **2000**, 112(15): 6873-6885.

La Magna, A.,Coffa, S.,Colombo, L. "Role of extended vacancy-vacancy interaction on the ripening of voids in silicon." *Physical Review Letters* **1999**, 82(8): 1720-1723.

Lacks, D. J.,Rutledge, G. C. "Simulation of the Temperature-Dependence of Mechanical-Properties of Polyethylene." *Journal of Physical Chemistry* **1994**, 98(4): 1222-1231.

Lauritzen, J. I.,Hoffman, J. D. "Extension of Theory of Growth of Chain-Folded Polymer Crystals to Large Undercoolings." *Journal of Applied Physics* **1973**, 44(10): 4340-4352.

Lavine, M. S.,Waheed, N.,Rutledge, G. C. "Molecular dynamics simulation of orientation and crystallization of polyethylene during uniaxial extension." *Polymer* **2003**, 44(5): 1771-1779.

Lin, L.,Argon, A. S. "Structure and Plastic-Deformation of Polyethylene." *Journal of Materials Science* **1994**, 29(2): 294-323.

Liu, C.,Muthukumar, M. "Langevin dynamics simulations of early-stage polymer nucleation and crystallization." *Journal of Chemical Physics* **1998**, 109(6): 2536-2542.

Lotz, B. "What can polymer crystal structure tell about polymer crystallization processes?" *European Physical Journal E* **2000**, 3(2): 185-194.

Lovinger, A. J.,Davis, D. D.,Padden, F. J. "Kinetic-Analysis of the Crystallization of Poly(Para-Phenylene Sulfide)." *Polymer* **1985**, 26(11): 1595-1604.

Luth, H.,Nyburg, S. C.,Robinson, P. M.,Scott, H. G. "Crystallographic and Calorimetric Phase Studies of the n-Eicosane $C_{20}H_{42}$: n-Docosane $C_{22}H_{46}$ System." *Molecular Crystals and Liquid Crystals* **1974**, 27: 337-357.

Lyulin, A. V.,Adolf, D. B.,Davies, G. R. "Brownian dynamics simulations of linear polymers under shear flow." *Journal of Chemical Physics* **1999**, 111(2): 758-771.

Mahendrasingam, A.,Blundell, D. J.,Martin, C.,Fuller, W.,MacKerron, D. H.,Harvie, J. L.,Oldman, R. J.,Riekel, C. "Influence of temperature and chain orientation on the crystallization of poly(ethylene terephthalate) during fast drawing." *Polymer* **2000**, 41(21): 7803-7814.

Mandelkern, L. (1958). Growth and perfection of Crystals. Proceedings of the International Conference on Crystal Growth, New York, John Wiley.

Mandelkern, L. *Crystallization of polymers* McGraw-Hill: New York, 1964.

Mandelkern, L.,Jain, N. L.,Kim, H. "Temperature Dependence of the Growth Rate of Spherulites." *Journal of Polymer Science Part A-2: Polymer Physics* **1968**, 6: 165-180.

Mansfield, M. L. "Monte-Carlo Study of Chain Folding in Melt-Crystallized Polymers." *Macromolecules* **1983**, 16(6): 914-920.

Martonak, R.,Paul, W.,Binder, K. "Orthorhombic phase of crystalline polyethylene: A Monte Carlo study." *Journal of Chemical Physics* **1997**, 106(21): 8918-8930.

Mavrantzas, V. G.,Theodorou, D. N. "Atomistic Monte Carlo simulation of steady-state uniaxial, elongational flow of long-chain polyethylene melts: dependence of the melt

degree of orientation on stress, molecular length and elongational strain rate." *Macromolecular Theory and Simulations* **2000**, 9(8): 500-515.

Mayo, S. L.,Olafson, B. D.,Goddard, W. A. "Dreiding - a Generic Force-Field for Molecular Simulations." *Journal of Physical Chemistry* **1990**, 94(26): 8897-8909.

Meyer, H.,Muller-Plathe, F. "Formation of chain-folded structures in supercooled polymer melts examined by MD simulations." *Macromolecules* **2002**, 35(4): 1241-1252.

Miller, A. A. "Kinetic Interpretation of the Glass Transition: Glass Temperatures of n-Alkane Liquids and Polyethylene." *Journal of Polymer Science Part A-2: Polymer Physics* **1968**, 6: 249-257.

Nakamura, K.,Katayama, K.,Amano, T. *Journal of Applied Polymer Science* **1973**, 17: 1031.

Narang, R. S.,Sherwood, J. N. "The purification and single crystal growth of n-alkanes." *Journal of Crystal Growth* **1980**, 49: 357-362.

Nose, S. "A Molecular-Dynamics Method for Simulations in the Canonical Ensemble." *Molecular Physics* **1984**, 52(2): 255-268.

Nozaki, K.,Hikosaka, M. Nucleation and Growth in the Solid-solid Phase transtitions of n-alkanes. *Crystallization Processes in Fats and Lipid Systems*. Garti, N.,Sato, K. Marcel Dekker: New York, 2001: 151-176.

Okada, M.,Nishi, M.,Takahashi, M.,Matsuda, H.,Toda, A.,Hikosaka, M. "Molecular weight dependence of the lateral growth rate of polyethylene - 2. Folded-chain crystals." *Polymer* **1998**, 39(19): 4535-4539.

Pant, P. V. K.,Han, J.,Smith, G. D.,Boyd, R. H. "A Molecular-Dynamics Simulation of Polyethylene." *Journal of Chemical Physics* **1993**, 99(1): 597-604.

Paradkar, R. P.,Sakhalkar, S. S.,He, X.,Ellison, M. S. "Estimating crystallinity in high density polyethylene fibers using online Raman spectroscopy." *Journal of Applied Polymer Science* **2003**, 88(2): 545-549.

Paul, W.,Yoon, D. Y.,Smith, G. D. "An Optimized United Atom Model for Simulations of Polymethylene Melts." *Journal of Chemical Physics* **1995**, 103(4): 1702-1709.

Point, J. J. "A New Theoretical Approach of Secondary nucleation at high supercooling." *Macromolecules* **1979**, 12(4): 770-775.

Rastogi, S.,Hikosaka, M.,Kawabata, H.,Keller, A. "Role of Mobile Phases in the Crystallization of Polyethylene .1. Metastability and Lateral Growth." *Macromolecules* **1991**, 24(24): 6384-6391.

Ratajski, E.,Janeschitz-Kriegl, H. "How to determine high growth speeds in polymer crystallization." *Colloid and Polymer Science* **1996**, 274(10): 938-951.

Rigby, D.,Roe, R. J. "Molecular-Dynamics Simulation of Polymer Liquid and Glass .1. Glass-Transition." *Journal of Chemical Physics* **1987**, 87(12): 7285-7292.

Rudisill, J. W.,Fetsko, S. W.,Cummings, P. T. "Brownian dynamics simulation of chain models for dilute polymer solutions in shear flow." *Computational Polymer Science* **1993**, 3: 23-31.

Ryan, A. J.,Fairclough, J. P. A.,Terrill, N. J.,Olmsted, P. D.,Poon, W. C. K. "A scattering study of nucleation phenomena in polymer crystallisation." *Faraday Discussions* **1999**, (112): 13-29.

Ryckaert, J. P.,Bellmans, A. "Molecular dynamics of liquid n-butane near its boiling point." *Chemical Physics Letters* **1975**, 30(1): 123-125.

Sadler, D. M.,Gilmer, G. H. "Rate-Theory Model of Polymer Crystallization." *Physical Review Letters* **1986**, 56(25): 2708-2711.

Sadler, D. M.,Gilmer, G. H. "Selection of Lamellar Thickness in Polymer Crystal-Growth - a Rate-Theory Model." *Physical Review B-Condensed Matter* **1988**, 38(8): 5684-5693.

Sasaki, S.,Tashiro, K.,Kobayashi, M.,Izumi, Y.,Kobayashi, K. "Microscopically viewed structural change of PE during the isothermal crystallization from the melt - II. Conformational ordering and lamellar formation mechanism derived from the coupled interpretation of time-resolved SAXS and FTIR data." *Polymer* **1999**, 40(25): 7125-7135.

Schneider, W.,Koppl, A.,Berger, J. "Non-Isothermal Crystallization of Polymers." *International Polymer Processing* **1988**, 2(3-4): 151-154.

Schultz, J. M.,Hsiao, B. S.,Samon, J. M. "Structural development during the early stages of polymer melt spinning by in-situ synchrotron X-ray techniques." *Polymer* **2000**, 41(25): 8887-8895.

Semenov, A. N.,Joanny, J. F. "Kinetics of Adsorption of Linear Homopolymers onto Flat Surfaces - Rouse Dynamics." *Journal De Physique Ii* **1995**, 5(6): 859-876.

Shimizu, T.,Yamamoto, T. "Melting and crystallization in thin film of n-alkanes: A molecular dynamics simulation." *Journal of Chemical Physics* **2000**, 113(8): 3351-3359.

Sirota, E. B.,Singer, D. M.,King, H. E. "Structural Effects of High-Pressure Gas on the Rotator Phases of Normal-Alkanes." *Journal of Chemical Physics* **1994**, 100(2): 1542-1551.

Small, D. M. *The Physical Chemistry of Lipids: from alkanes to phospholipids* Plenum Press: New York, 1986.

Smith, G. D.,Yoon, D. Y. "Equilibrium and Dynamic Properties of Polymethylene Melts from Molecular-Dynamics Simulations .1. N-Tridecane." *Journal of Chemical Physics* **1994**, 100(1): 649-658.

Snetivy, D.,Yang, H. F.,Vancso, G. J. "Imaging of Different Crystal Planes in Oriented Polyethylene by Atomic Force Microscopy." *Journal of Materials Chemistry* **1992**, 2(8): 891-892.

Somani, R. H.,Hsiao, B. S.,Nogales, A.,Srinivas, S.,Tsou, A. H.,Sics, I.,Balta-Calleja, F. J.,Ezquerra, T. A. "Structure development during shear flow-induced crystallization of i-PP: In-situ small-angle X-ray scattering study." *Macromolecules* **2000**, 33(25): 9385-9394.

Sorensen, M. R.,Voter, A. F. "Temperature-accelerated dynamics for simulation of infrequent events." *Journal of Chemical Physics* **2000**, 112(21): 9599-9606.

Sorensen, R. A.,Liau, W. B.,Kesner, L.,Boyd, R. H. "Prediction of Polymer Crystal-Structures and Properties - Polyethylene and Poly(Oxymethylene)." *Macromolecules* **1988**, 21(1): 200-208.

Steele, W. M. "The physical interaction of gases with crystalline solids." *Surface Science* **1973**, 36: 317-352.

Stribeck, N.,Alamo, R. G.,Mandelkern, L.,Zachmann, H. G. "Study of the Phase-Structure of Linear Polyethylene by Means of Small-Angle X-Ray-Scattering and Raman-Spectroscopy." *Macromolecules* **1995**, 28(14): 5029-5036.

Strobl, G. "From the melt via mesomorphic and granular crystalline layers to lamellar crystallites: A major route followed in polymer crystallization?" *European Physical Journal E* **2000**, 3(2): 165-183.

Sukhishvili, S. A.,Chen, Y.,Muller, J. D.,Gratton, E.,Schweizer, K. S.,Granick, S. "Materials science - Diffusion of a polymer 'pancake'." *Nature* **2000**, 406(6792): 146.

Swope, W. C.,Andersen, H. C.,Berens, P. H.,Wilson, K. R. "Physical Clusters of Molecules." *Journal of Chemical Physics* **1982**, 76(637): 648.

Tashiro, K.,Sasaki, S.,Gose, N.,Kobayashi, M. "Microscopically-viewed structural change of polyethylene during isothermal crystallization from the melt - I. Time-resolved FTIR spectral measurements." *Polymer Journal* **1998**, 30(6): 485-491.

Tian, M. W.,Dosiere, M.,Hocquet, S.,Lemstra, P. J.,Loos, J. "Novel aspects related to nucleation and growth of solution grown polyethylene single crystals." *Macromolecules* **2004**, 37(4): 1333-1341.

Toda, A. "Growth of Polyethylene Single-Crystals from the Melt - Change in Lateral Habit and Regime I-Ii-Transition." *Colloid and Polymer Science* **1992**, 270(7): 667-681.

Toma, L.,Toma, S.,Subirana, J. A. "Simulation of polymer crystallization through a dynamic Monte Carlo lattice model." *Macromolecules* **1998**, 31(7): 2328-2334.

Toxvaerd, S. "Molecular-Dynamics Calculation of the Equation of State of Alkanes." *Journal of Chemical Physics* **1990**, 93(6): 4290-4295.

Toxvaerd, S. "Equation of state of alkanes .2." *Journal of Chemical Physics* **1997**, 107(13): 5197-5204.

Turnbull, D.,Fisher, J. C. "Rate of Nucleation in Condensed Systems." *Journal of Chemical Physics* **1949**, 17(1): 71-73.

Umemoto, S.,Kobayashi, N.,Okui, N. "Molecular weight dependence of crystal growth rate and its degree of supercooling effect." *Journal of Macromolecular Science-Physics* **2002**, B41(4-6): 923-938.

Umemoto, S.,Okui, N. "Master curve of crystal growth rate and its corresponding state in polymeric materials." *Polymer* **2002**, 43(4): 1423-1427.

Ungar, G.,Keller, A. "Inversion of the Temperature-Dependence of Crystallization Rates Due to Onset of Chain Folding." *Polymer* **1987**, 28(11): 1899-1907.

Ungar, G.,Stejny, J.,Keller, A.,Bidd, I.,Whiting, M. C. "The Crystallization of Ultralong Normal Paraffins - the Onset of Chain Folding." *Science* **1985**, 229(4711): 386-389.

Vacatello, M.,Flory, P. J. "Conformational Statistics of Poly(Methyl Methacrylate)." *Macromolecules* **1986**, 19(2): 405-415.

Van Antwerpen, F.,van Krevelen, D. W. "Influence of Crystallization Temperature, Molecular-Weight, and Additives on Crystallization Kinetics of Poly(Ethylene Terephthalate)." *Journal of Polymer Science Part B-Polymer Physics* **1972**, 10(12): 2423-2435.

Van Kampen, N. G. *Stochastic Processes in Physics and Chemistry* Elsevier: Amsterdam, 1992.

van Krevelen, D. W. "Crystallinity of Polymers and the Means to Influence the Crystallization Process." *Chimia* **1978**, 32(8): 279-294.

Vargaftik, N. B.,Vinogradov, Y. K.,Yargin, V. S. *Handbook of Physical Properites of Liquids and Gases* Begell House: New York, 1996.

Voter, A. F. "Hyperdynamics: Accelerated molecular dynamics of infrequent events." *Physical Review Letters* **1997**, 78(20): 3908-3911.

Voter, A. F. "A method for accelerating the molecular dynamics simulation of infrequent events." *Journal of Chemical Physics* **1997**, 106(11): 4665-4677.

Voter, A. F. "Parallel replica method for dynamics of infrequent events." *Physical Review B-Condensed Matter* **1998**, 57(22): R13985-R13988.

Wagner, J.,Phillips, P. J. "The mechanism of crystallization of linear polyethylene, and its copolymers with octene, over a wide range of supercoolings." *Polymer* **2001**, 42(21): 8999-9013.

Wang, Z. G.,Hsiao, B. S.,Sirota, E. B.,Srinivas, S. "A simultaneous small- and wide-angle X-ray scattering study of the early stages of melt crystallization in polyethylene." *Polymer* **2000**, 41(25): 8825-8832.

Wilhelmi, J. L.,Rutledge, G. C. "Simulation of the structure and properties of the polyethylene crystal surface." *Journal of Physical Chemistry* **1996**, 100(25): 10689-10695.

Williams, M. L.,Landel, R. F.,Ferry, J. D. "The Temperature Dependence of Relaxation Mechanisms in Amorphous Polymers and Other Glass-forming Liquids." *Journal of the American Chemical Society* **1955**, 77: 3701-3707.

Yamamoto, T. "Molecular-dynamics simulation of polymer ordering. 1. Crystallization from vapor phase." *Journal of Chemical Physics* **1998**, 109(11): 4638-4645.

Yamamoto, T. "Molecular dynamics simulation of polymer ordering. II. Crystallization from the melt." *Journal of Chemical Physics* **2001**, 115(18): 8675-8680.

Yamamoto, T. "Molecular dynamics modeling of polymer crystallization from the melt." *Polymer* **2004**, 45(4): 1357-1364.

Yamamoto, T.,Matsumoto, S.,Hirose, M. "A Monte Carlo study of the pattern formation during transitions in n-alkane crystals." *Journal of Chemical Physics* **2000**, 112(17): 7627-7633.

Yang, X.,Mao, X. "Molecular dynamics simulation on crystalline nucleation behavior of a single chain touching substrate surface. II. Temperature dependence." *Computational and Theoretical Polymer Science* **1997**, 7(2): 81.

Yoon, C. S.,Sherwood, J. N.,Pethrick, R. A. "Growth, Characterization and Ultrasonic Studies of N-Eicosane Single-Crystals." *Journal of the Chemical Society-Faraday Transactions I* **1989**, 85: 3221-3232.

Yoon, D. Y.,Smith, G. D.,Matsuda, T. "A Comparison of a United Atom and an Explicit Atom Model in Simulations of Polymethylene." *Journal of Chemical Physics* **1993**, 98(12): 10037-10043.

Ziabicki, A. *Fundamentals of Fibre Formation* John Wiley: London, 1976.

Appendix A

Methods of Accelerating Nucleation of an Ordered Phase

Several methods were discussed for accelerating the nucleation of an ordered phase. During the course of this work, we explored some of these methods briefly, in an attempt to better understand their effects. The three methods that we explored were used to decrease the extension time of the chains in the system. These three methods are increasing the chain rigidity, lowering the molecular weight, and introducing an orienting deformation.

Increasing the chain stiffness can be accomplished in several ways related to changing the potential between atoms. For the simulations discussed in Chapter 4 and 5, we chose to use the forcefield by Paul et al., because it was the best at duplicating the P-V-T behavior of short alkanes, and was based on the most recent experimental data and ab initio calculations [Paul et al. 1995]. The differences in forcefields makes comparison to other simulations difficult. Most forcefields overestimate the *trans-gauche* barrier and the *cis* barrier, through the choice of forcefield. The DREIDING forcefield [Mayo et al. 1990] is a commonly used forcefield [Kavassalis and Sundararajan 1993; Fujiwara and

Sato 1998] that uses 3 equal torsional wells, and constructs the *trans-gauche* and *cis* barriers by allowing 1-4 non-bonded interactions. This leads to almost no *gauche* well, and a *cis* barrier that is approximately three times too high. In addition, in our attempts to duplicate other recent work [Liu and Muthukumar 1998], we were only able to do so by applying the Paul forcefield, with the inclusion of 1-4 interactions, an error we suspect is commonly made in the application of this forcefield. This inclusion leads to a disappearance of the *gauche* well completely, and a *cis* barrier that is nearly twenty times too large.

We implemented simulations including the 1-4 non-bonded interactions to show the effect of this type of forcefield on the behavior of the chain. Two simulations were conducted, uniformly cooling an equilibrated chain of length 500 beads in a vacuum from 700 K to 500 K, over 5 ns. Figure A.1 shows the effect of the torsional bias of the development of orientational order, given by the orientaional order parameter in Eq. (3.18). The torsional bias accelerates the extension of chain stems and their alignment, allowing for the observation of chain folding in a lamellar-like structure. The torsional bias creates a change in the percentages of *trans* states at 500 K from approximately 60% to 90%. While the system does reveal salient features of crystallization, the torsional bias severely stiffens the chains, changing the *trans-gauche* torsional distribution. As a result, the forcefield is no longer properly calibrated, having a melting point that approaches 650 K. The material simulated is no longer polyethylene, though it does yield insight to polymer crystallization.

Alternatively, crystallization can be accelerated by lowering the molecular weight

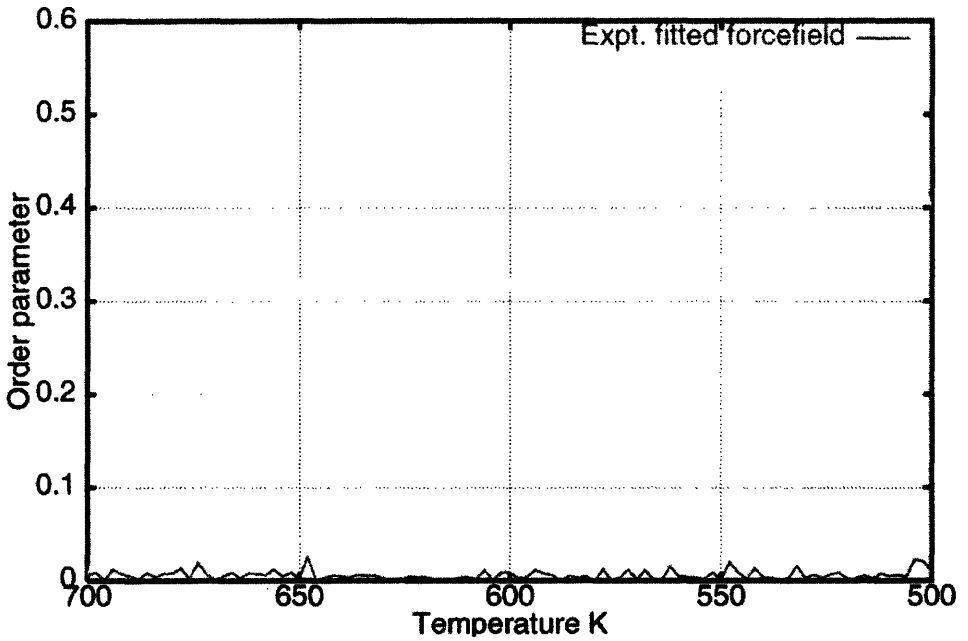

Figure A.1 The effect of inclusion of 1-4 non-bonded interactions on the development of orientational order for a chain of 500 beads in vacuum, cooled uniformly from 700 K to 500 K over 5 ns. Lines show order parameter for forcefield by Paul et. al. (dark gray) and the same forcefield with 1-4 interactions (light gray).

of the system, i.e. similating shorter chains. Shorter chains have faster relaxation times, and therefore, require less time to establish an extended state. The Rouse relaxation time predicts that the relaxation time varies with the number of beads by N^{-2}. We performed simulations of 400 beads in a vacuum, being cooled uniformly from 350 K to 200 K, over 12 ns, in chain configurations of one C400 chain, 10 C40 chains, and 20 C20 chains. The effect of the chain length on the development of orientational order is shown in Fig. A.2. The 20 C20 chains are able to develop orientational order in a time frame accessible to the simulation technique, while the C400 chain and 10 C40 chains are unable to develop orientation order, despite the fact that the simulation temperature is below the crystallization temperature. These longer chains in vacuum remain in the supercooled metastable state for the course of the simulation, even though the vacuum enhances chain diffusion well past what is seen in melt systems.

In addition, introducing orienting deformations to the system can decrease the time for extension of the chains. The Langevin dynamics technique, discussed in detail in Appendix B, allows for the easy inclusion of shear deformation, by imposing a frictional drag that is a function of position. This frictional drag is compensated by the stochastic forces imposed on the system. We can include a frictional drag in the y direction that is a function of the x position, to create a shear deformation of the system. We use a solvent viscosity of 1 cp, converted to frictional drag by Stokes' Law. The effect of shear on the orientational order parameter for a single C500 chain at 300 K, is shown in Fig. A.3. Imposing a shear of $5. \times 10^{11}$ s^{-1}, does not have significant impact on the orientational order. However, imposing a shear of $1. \times 10^{12}$ s^{-1}, makes extended conformations accessible in the simulation time. Our simulations suggest that there

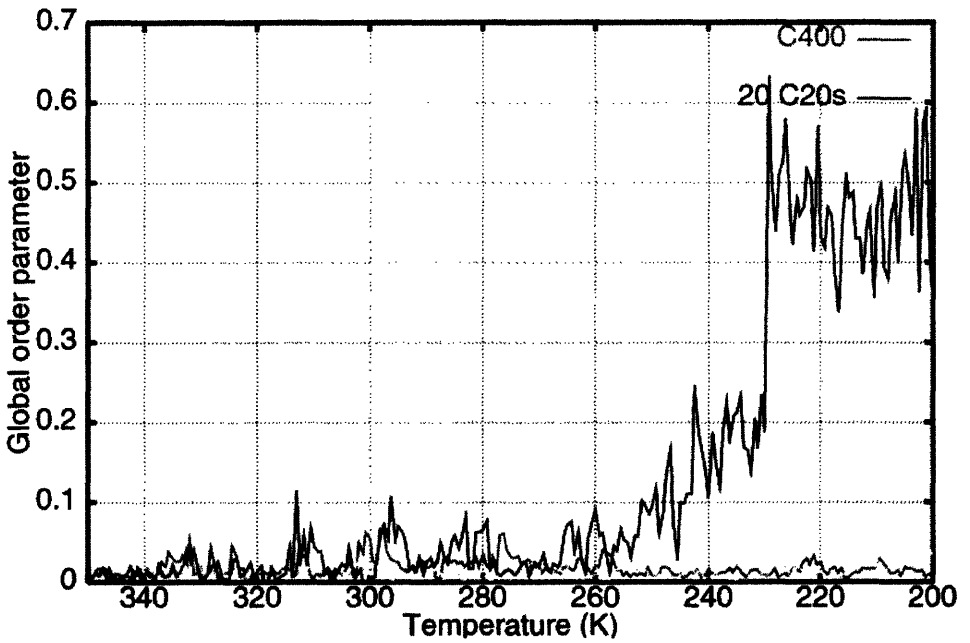

Figure A.2 The effect of chain length on the development of orientational order for a 400 beads in vacuum, cooled uniformly from 350 K to 200 K over 12 ns. Lines show order parameter for one C400 chain (dark gray), 10 C40 chains (light gray), and 20 C20 chains (black).

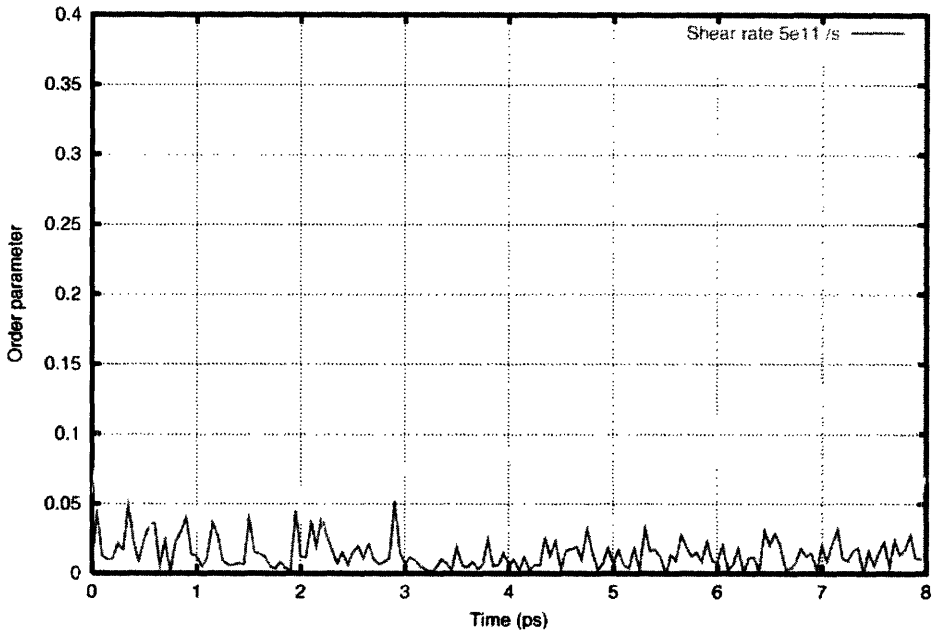

Figure A.3 The effect of shear rate on the development of orientational order for a chain of 500 beads in dilute solution, at 300 K. Lines show order parameter for shear rates of 5. x 10^{11} s^{-1} (dark gray), and 1. x 10^{12} s^{-1} (light gray).

exists a critical shear rate that allows the transition from a globule to an extended state.The extended state that forms is temporal and rotates about itself for the case of a single chain in dilute solution.

Our research is based on using accurate potentials and methods appropriate for the simulated system. Therefore, we decided not to introduce a torsional bias in our simulation that would make it difficult to relate our results to experimental systems. For melt crystallization, the Langevin dynamics technique is also not appropriate, since one of the inherent assumptions in the technique is that the stochastic forces are acting on a faster time scale than the movement of the simulated beads. This is appropriate for some solvent systems, but not for melt systems, where there is no medium to induce frictional drag on fast time scales.

The use of shorter chains is relevant to our simulations, since it allows us to simulate molecules that we can relate to experiment. However, in order to make these simulations relevant to polymer crystallization, a relationship governing the molecular weight dependence of crystal growth rates must also be established. Our analysis of this effect is discussed in Chapters 6 and 7.

Appendix B

The Applicability of the Brownian Dynamics Technique for Polymer-Solvent Simulations at Realistic Polymer Concentrations

In recent publications, it has been suggested that characteristic behavior of polymer crystallization can be captured with the Langevin dynamics technique [Liu and Muthukumar 1998]. However, the Langevin (or Brownian) dynamics technique generally assumes that the Brownian beads are present in dilute concentrations in solutions; this leads to questions about the applicability of this technique in highly concentrated regions, such as dense polymer crystals.

Other groups have studied the intereactions of linear polymer chains in dilute solutions using Brownian dynamics (BD) [Rudisill et al. 1993; Lyulin et al. 1999]. Lyulin *et. al.* has performed such studies, with the end goal of studying dedrimers using the Brownian dynamics technique. Dedrimers, like polymer crystals, are systems with high concentrations of polymer beads that present a challenge to the Brownian dynamics

technique. An overlap in interest exists to explore the applicability of Brownian dynamics techniques for concentrated systems.

Two approaches were considered. One was a comparision of a certain high concentration system at different levels of detail, including BD with a preaveraged hydrodynamic interaction (HI) tensor, BD with a Rotne-Prager HI tensor, and explicit solvent HI. The other was the attempting to quantify the differences shortcomings of the BD technique as a function of the distance between interacting beads. A three month project, funded by CAEFF was proposed to study the relationships between these techniques, and determine their applicability to concentrated systems.

In Langevin dynamics, the equations of motion are integrated stochastically, and yield the 3N dimensional Langevin equation [Allen and Tildesley 1987], which relates change in inertia to the force field, frictional drag, and noise for N interacting particles:

$$\dot{\mathbf{p}}(t) = -\nabla \mathbf{U} - \zeta \mathbf{p}(t) + \mathbf{W}(t) \qquad \text{(B.1)}$$

where $\mathbf{p}(t)$ is the momentum vector, $\mathbf{U}$ is the potential energy from the force field, ζ is scalar (isotropic) friction coefficient, and $\mathbf{W}(t)$ is the vector of random forces which are Gaussian and acting independently of each other. The random forces and the frictional forces essentially come from the same source, the collisions between solvent and polymer sub-units. The relationship between these two is captured by a special case of the *fluctuation-dissipation theorem of the second kind* that relates the friction coefficient to the second moment of the random noise:

$$\langle W_i(t) \bullet W_j(t') \rangle = 2mkT\xi\, \delta_{ij}\, \delta(t - t') \tag{B.2}$$

where m is the particle mass, k is Boltzman's constant, and T is the temperature of the system [Van Kampen 1992]. These equations, combined with $\mathbf{dr}/dt = \mathbf{p}/m$, are the basic equations governing this type of simulation. This allows the Brownian effects of the solvent to be modeled, without explicitly including and keeping track of solvent molecules, which makes this simulation very efficient.

Our work has been focused on creating a Langevin dynamics simulator that incorporates excluded volume interactions, as well as other molecular forces, such as bond stretch, angle stretch, and torsional forces. Another important factor in correctly characterizing rheological behavior is hydrodynamic interactions between beads due to the presence of solvent. To include hydrodynamic interactions, requires that the friction coefficient be dependent on momentum and configuration. However, including momentum makes the solution to the equations intractable. For this reason, all simulations including hydrodynamic interactions must assume that the time scales for momentum relaxation and position relaxation are separable. Then we can consider time intervals greater than the momentum relaxation time, and work in the diffusive regime.

However, incorporating hydrodynamic interactions in the momentum-level (Langevin/Fokker-Planck) equation that has been presented is not possible. It is necessary to use the diffusion-limited position-level (Langevin/Smoluchowski) equation:

$$\frac{\partial}{\partial t}\rho(r,t) + (\nabla r \cdot \frac{D(t)}{k_b T}) fp(r,t) = \nabla r D(t) \cdot \nabla r \rho(r,t)\,. \tag{B.3}$$

The integration of this equation, in the diffusion-limited case, was performed by Ermak and McCammon [Ermak and McCammon 1978], to yield the equation:

$$r_i(t+\Delta t) = r_i(t) + \sum_j \left(\frac{D_{ij}(t)F_j(t)}{k_b T} + \frac{\partial D_{ij}(t)}{\partial r_j} \right) \Delta t + R_i(\Delta t), \tag{B.4}$$

where D_{ij} are the components of the diffusion tensor between atoms i and j, and F_{ij} is the force between atoms i and j, computed from the interaction potential. R_{ij} is also related to D_{ij} by the fluctuation-dissipation theorem and is expressed by the relation:

$$\left\langle R_i(\Delta t) R_j(\Delta t) \right\rangle = 2D_{ij}\Delta t . \tag{B.5}$$

There are two diffusion tensors that are suggested as approximations to the hydrodynamic interaction: the Oseen tensor and the Rotne-Prager tensor. The Rotne-Prager tensor is an improvement over the Oseen tensor, in that it accounts for the volume occupied by the beads and guarantees a positive definite tensor, making it more rigorous. The Rotne-Prager tensor is given by:

$$\begin{aligned} D_{ii} &= \frac{kT}{6\pi\eta a}\overline{\overline{I}} \\ D_{ij} &= \frac{kT}{8\pi\eta r_{ij}} \left[\left(\overline{\overline{I}} + \frac{\overline{r_{ij} r_{ij}}}{r_{ij}^2} \right) + \frac{2a^2}{r_{ij}^2} \left(\frac{1}{3}\overline{\overline{I}} - \frac{\overline{r_{ij} r_{ij}}}{r_{ij}^2} \right) \right] \end{aligned} \tag{B.6}$$

where a is the sphere radius, η is the solvent viscosity, r_{ij} is the distance between atoms i and j, and $\overline{\overline{I}}$ is the identity matrix.

The diffusion tensor, expressed as the Rotne-Prager tensor is a function of the configuration of the chain beads, and thus becomes a function of time. Since the computation of the tensor and the corresponding random forces is expensive, an alternate expression is often used, which is averaged based on the average inverse hydrodynamic radius. This preaveraged tensor is not dependent on configuration, and is computed only once. However, this means that the hydrodynamic interations between beads no longer depend on the distance between individual beads. The preaveraged forms of the Oseen and Rotne-Prager tensors are identical, and are expressed by:

$$D_{ii} = \frac{kT}{6\pi\eta a}\overline{\overline{I}}$$
$$D_{ij} = \frac{kT}{6\pi\eta}\left\langle\frac{1}{r_{ij}}\right\rangle\overline{\overline{I}} \qquad \text{(B.7)}$$

Recently, Lyulin, *et.al.* have studied linear polymers under shear flow, using Brownian dynamics simulations, with and without excluded volume and hydrodynamic interactions, to determine the dependency of intrinsic viscosity on shear rates, for various models [Lyulin et al. 1999]. Correlation function, density distributions, and end-to-end vectors were computed. The Adolf group is now in the process of performing similar calculations for dedrimer systems in shear.

Our project's goal was to obtain measurements for the average inverse hydrodynamic radius for various dendrimer systems. Using BD with full hydrodynamic

interactions, three dendrimer systems were equilibrated, and average inverse hydrodynamic radii were measured for these systems with a fixed bond length of one, as shown in Table B.1.

The Lyulin BD code was then adapted to calculate the diffusion tensor based on these values, and use the preaveraged diffusion tensor to calculate random forces at each step. Results from these runs will be incorporated into a comparison between BD and MD for dedrimers, prepared by the Adolf group.

We also desired to find a more quantitative relationship between Brownian dynamics and explicit solvent molecular dynamics. Our approach to this problem was to find an effective diffusion tensor generated by explicit solvent molecular dynamics, which would be comparable to the diffusion tensor used in Brownian dynamics. Finding an effective diffusion tensor as a function of the average hydrodynamic radius would allow us to determine where the Rotne-Prager tensor broke down and calculate a correction for it.

The vector form of the Ermak-McCammon equation, assuming a Rotne-Prager or Oseen type diffusion tensor, can be written:

$$\bar{v} = \left(\overline{\overline{DF}}\right) + \bar{R} \tag{B.8}$$

where $\bar{v}$ is the velocity tensor. We assume that the chain beads in a molecular dynamics simulation will follow this equation, with the neighboring solvent beads behaving as a randomizing force. However, knowing only the values of the velocities and forces at each time step, there is no unique solution for the diffusion tensor. Therefore, it becomes

Table B.1 The average inverse hydrodynamic radii for three generations of dendrimers

Generation of dendrimer	*Spacer*	*Number of beads*	*Average inverse HI radius (in units of bond lengths)*
3	1	91	0.2985
4	1	187	0.2385
5	1	379	0.1925

necessary to invoke the central limit theorem and consider the average diffusion tensor.

If we assume that on average the random contributions will be filtered out by the central limit theorem, we can ignore the contribution of the random forces in our computation of a diffusion tensor at each time step:

$$\bar{v} = \bar{\bar{D}}\bar{F} \tag{B.9}$$

To rigorously complete the formulation requires that we invert the force vector, which we cannot do. Therefore we take the outer product of both sides with the transpose of the velocity vector, for reasons that will become apparent shortly:

$$\left(\overline{v\ v^T}\right) = \bar{\bar{D}}\left(\overline{F\ v^T}\right) \tag{B.10}$$

One of the matrices must be inverted to solve for the diffusion tensor. However, neither of these matrices is always nonsingular. Therefore we must now invoke the fact that we have several values to sample from; so that the values we yield are averages.

$$\left\langle\overline{v\ v^T}\right\rangle = \left\langle\bar{\bar{D}}\right\rangle\left\langle\overline{F\ v^T}\right\rangle \tag{B.11}$$

With this formulation we can take advantage of the fact that when the velocities come from a Gaussian distribution, the following simplification applies:

$$\left\langle \overline{v \; v^T} \right\rangle = \frac{1}{N} \left\langle \overline{v} \bullet \overline{v} \right\rangle \overline{\overline{I}} \tag{B.12}$$

where N is the length of the velocity vector. (This is valid since the velocities are temperature-dependent and have a Gaussian distribution. This is why we chose to take the outer product with the transpose of the velocity vector, rather than the forces vector, which is less likely to be Gaussian.) Now we can solve for the inverse of the diffusion tensor.:

$$\begin{aligned}
&\frac{1}{N}\left\langle \overline{v} \bullet \overline{v} \right\rangle \overline{\overline{I}} = \left\langle \overline{\overline{D}} \right\rangle \left\langle \overline{F \; v^T} \right\rangle \\
&\left\langle \overline{\overline{D}} \right\rangle^{-1} \frac{1}{N}\left\langle \overline{v} \bullet \overline{v} \right\rangle \overline{\overline{I}} = \left\langle \overline{\overline{D}} \right\rangle^{-1} \left\langle \overline{\overline{D}} \right\rangle \left\langle \overline{F \; v^T} \right\rangle \\
&\left\langle \overline{\overline{D}} \right\rangle^{-1} = \frac{\left\langle \overline{F \; v^T} \right\rangle}{\frac{1}{N}\left\langle \overline{v} \bullet \overline{v} \right\rangle}
\end{aligned} \tag{B.13}$$

Because of the form of the preaveraged diffusion tensor, we know that its inverse is nonsingular and can be inverted to yield the expected value.

This method of computing the expected value of the diffusion tensor must be tested for a known value of the diffusion tensor, by selecting velocities from a random normal distribution, and calculating corresponding forces that satisfy the equation. After randomizing the forces, the diffusion tensor was back calculated according to the above formula. This guarantees that if a pattern exists in a molecular dynamics simulation, it can be captured with this method. When the random forces are selected from a Gaussian

distribution, the components of the diffusion tensor converge properly to the anticipated values.

This formulation depends on the assumption that the random forces are filtered by the central limit theorem, which is true for the Gaussian distribution of random forces we selected. However, in the Brownian formulation, the random forces are correlated, in addition to being normally distributed. While this would be difficult to test beforehand, we can test if the formulation depends on the distribution of random forces by using a uniform distribution instead of a Gaussian distribution. This also yields similar convergence, with the only restrictions being symmetry and a mean of zero, both of which are satisfied in for the Brownian random forces.

This method may be used in conjuction with explicit solvent molecular dynamics data, which can then be compared to the values of the preaveraged diffusion tensor suggested by the preaveraged Oseen or Rotne-Prager diffusion tensor, to determine at what concentrations the preaveraged tensor breaks down. This information can be used to create a functional correction to the Rotne-Prager tensor that can be included in the form:

$$D_{ij} = D_{ij}^{RP} f\left(r_{ij}^{-1}\right). \tag{B.14}$$

Without some correction for the breakdown of the preavaraged tensor, either simulation accuracy or simulation speed are sacrificed when using Brownian dynamics technique in regions of high concentration of polymer beads. A formulation such as this would be of great value to research that utilizes the Brownian dynamic technique in high concentration regions.